

# INTERNATIONAL JOURNAL OF MODERN ENGINEERING

The Leading Journal of Engineering, Applied Science and Technology

Industrial

Electronics

Biomedical

Civil

Aerospace

Computer

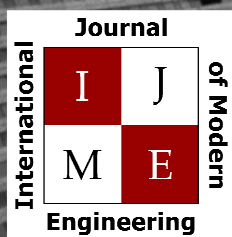
Electrical

Chemical

Mechanical



# ENGINEERING



[www.ijme.us](http://www.ijme.us)

Print ISSN: 2157-8052  
Online ISSN: 1930-6628



[www.iajc.org](http://www.iajc.org)

## INTERNATIONAL JOURNAL OF MODERN ENGINEERING

### ABOUT IJME:

- IJME was established in 2000 and is the first and official flagship journal of the International Association of Journal and Conferences (IAJC).
- IJME is a high-quality, independent journal steered by a distinguished board of directors and supported by an international review board representing many well-known universities, colleges and corporations in the U.S. and abroad.
- IJME has an impact factor of **3.00**, placing it among the top 100 engineering journals worldwide, and is the #1 visited engineering journal website (according to the National Science Digital Library).

### OTHER IAJC JOURNALS:

- The International Journal of Engineering Research and Innovation (IJERI)  
For more information visit [www.ijeri.org](http://www.ijeri.org)
- The Technology Interface International Journal (TIIJ).  
For more information visit [www.tiij.org](http://www.tiij.org)

### IJME SUBMISSIONS:

- Manuscripts should be sent electronically to the manuscript editor, Dr. Philip Weinsier, at [philipw@bgsu.edu](mailto:philipw@bgsu.edu).

For submission guidelines visit  
[www.ijme.us/submissions](http://www.ijme.us/submissions)

### TO JOIN THE REVIEW BOARD:

- Contact the chair of the International Review Board, Dr. Philip Weinsier, at [philipw@bgsu.edu](mailto:philipw@bgsu.edu).

For more information visit  
[www.ijme.us/ijme\\_editorial.htm](http://www.ijme.us/ijme_editorial.htm)

### INDEXING ORGANIZATIONS:

- IJME is currently indexed by 22 agencies.  
For a complete listing, please visit us at [www.ijme.us](http://www.ijme.us).

### Contact us:

**Mark Rajai, Ph.D.**

Editor-in-Chief  
California State University-Northridge  
College of Engineering and Computer Science  
Room: JD 4510  
Northridge, CA 91330  
Office: (818) 677-5003  
Email: [mrajai@csun.edu](mailto:mrajai@csun.edu)



[www.tiij.org](http://www.tiij.org)



[www.ijeri.org](http://www.ijeri.org)

---

# INTERNATIONAL JOURNAL OF MODERN ENGINEERING

The INTERNATIONAL JOURNAL OF MODERN ENGINEERING (IJME) is an independent, not-for-profit publication, which aims to provide the engineering community with a resource and forum for scholarly expression and reflection.

IJME is published twice annually (fall and spring issues) and includes peer-reviewed research articles, editorials, and commentary that contribute to our understanding of the issues, problems, and research associated with engineering and related fields. The journal encourages the submission of manuscripts from private, public, and academic sectors. The views expressed are those of the authors and do not necessarily reflect the opinions of the IJME editors.

## EDITORIAL OFFICE:

Mark Rajai, Ph.D.  
Editor-in-Chief  
Office: (818) 677-2167  
Email: [ijmeeditor@ajc.org](mailto:ijmeeditor@ajc.org)  
Dept. of Manufacturing Systems  
Engineering & Management  
California State University-  
Northridge  
18111 Nordhoff Street  
Northridge, CA 91330-8332

## THE INTERNATIONAL JOURNAL OF MODERN ENGINEERING EDITORS

*Editor-in-Chief*

**Mark Rajai**

California State University-Northridge

*Production Editor*

**Philip Weinsier**

Bowling Green State University-Firelands

*Manuscript Editor*

**Philip Weinsier**

Bowling Green State University-Firelands

*Subscription Editor*

**Morteza Sadat-Hossieny**

Northem Kentucky University

*Executive Editor*

**Sangram Redkar**

Arizona State University

*Publisher*

**Bowling Green State University-Firelands**

*Technical Editors*

**Andrea Ofori-Boadu**

North Carolina A&T State University

**Michelle Brodke**

Bowling Green State University-Firelands

**Marilyn Dyrud**

Oregon Institute of Technology

**Mandar Khanal**

Boise State University

**Chris Kluse**

Bowling Green State University

**Zhaochao Li**

Morehead State University

**Sangram Redkar**

Arizona State University

*Web Administrator*

**Saeed Namyar**

Advanced Information Systems

---

# TABLE OF CONTENTS

<i>Editor's Note: Registration is open for the 8<sup>th</sup> IAJC international conference in Orlando, Florida</i> .....	4
Philip Weinsier, IJME Manuscript Editor	
<i>Computational Fluid Dynamics Simulation of Inhaled Submicron Bioaerosol Particle Flow and Deposition in the Human Lung</i> .....	5
Mohammed Ali, The University of Texas at Tyler	
<i>Influence of Annealing Treatment on the Properties of Low-Temperature Silicon Nitride Films Produced By Inductively Coupled Plasma Chemical Vapor Deposition</i> .....	12
Qingzhou Xu, Morehead State University	
<i>Performance-Based Design of Diagrid Tall Buildings for Earthquake Loads</i> .....	22
Mohammad T. Bhuiyan, West Virginia State University; Md. Arifuzzaman, King Faisal University; Ayed Alluqmani, Islamic University of Madinah	
<i>An Experimental Study of Colloid Liquid Bridge and Force Dynamics in Real-Time Processes</i> .....	32
Nhat Le, Minnesota State University; Shaobiao Cai, Minnesota State University; Yongli Zhao, St. Cloud State University	
<i>Comparative Tangential Stress Analyses of Curved Beams</i> .....	42
MA Muktadir, North Carolina A&T State University; Paul Akangah, North Carolina A&T State University; Sun Yi, North Carolina A&T State University	
<i>Study of Atmospheric Plasma Spraying of Fe-based Materials for Obtaining Wear-Resistance Coatings</i> .....	50
Duong Vu, Duy Tan University, Vietnam	
<i>An Improved Method for Predicting the Results of Accelerated Engine Air Filter Tests Based on Limited Data Sets</i> .....	57
Kevin M. Hubbard, Missouri State University; Neal Callahan, Missouri State University; Nebil Buyurgan, Missouri State University	
<i>Instructions for Authors: Manuscript Submission Guidelines and Requirements</i> .....	66



# 8<sup>TH</sup> IAJC INTERNATIONAL CONFERENCE

[www.2022.iajc.org](http://www.2022.iajc.org)

OCTOBER 13-16, 2022 – ORLANDO, FLORIDA

The leading indexed high-impact-factor conference on engineering and related technologies.

## Our Hotel—Embassy Suites



## Our Previous Tour—NASA's Kennedy Space Center



### CALL FOR CONFERENCE PROPOSALS

Conference Submission Deadlines:

- Abstract Submissions March 11, 2022
- Full-Paper Submissions (optional) April 15, 2022

Full papers may be submitted after a related abstract has been accepted for presentation. All full papers will automatically be reviewed for publication in the conference proceedings and the high-impact-factor IAJC journals after the conference. All submissions must be made using our online system at <https://2022.iajc.org/registration>

Have questions or need help? Contact Philip Weinsier (Conference General Chair) at [philipw@bgsu.edu](mailto:philipw@bgsu.edu)

## Editorial Review Board Members

Mohammed Abdallah	State University of New York (NY)	Rungun Nathan	Penn State Berks (PA)
Paul Akangah	North Carolina A&T State University (NC)	Arun Nambiar	California State University Fresno (CA)
Shah Alam	Texas A&M University-Kingsville (TX)	Aurenice Oliveira	Michigan Tech (MI)
Nasser Alaraje	Michigan Tech (MI)	Troy Ollison	University of Central Missouri (MO)
Ali Alavizadeh	Purdue University Northwest (IN)	Reynaldo Pablo	Purdue Fort Wayne (IN)
Lawal Anka	Zam fara AC Development (NIGERIA)	Basile Panoutsopoulos	Community College of Rhode Island (RI)
Jahangir Ansari	Virginia State University (VA)	Shahera Patel	Sardar Patel University (INDIA)
Sanjay Bagali	Acharya Institute of Technology (INDIA)	Thongchai Phairoh	Virginia State University (VA)
Kevin Berisso	Ohio University (OH)	Huyu Qu	Broadcom Corporation
Pankaj Bhambri	Guru Nanak Dev Engineering (INDIA)	Desire Rasolomampionona	Warsaw University of Tech (POLAND)
Sylvia Bhattacharya	Kennesaw State University (GA)	Michael Reynolds	University of West Florida (FL)
Monique Bracken	University of Arkansas Fort Smith (AR)	Nina Robson	California State University-Fullerton (CA)
Tamer Breakah	Ball State University (IN)	Marla Rogers	Fastboot Mobile, LLC
Michelle Brodke	Bowling Green State University (OH)	Dale Rowe	Brigham Young University (UT)
Shaobiao Cai	Penn State University (PA)	Karen Ruggles	DeSales University (PA)
Rajab Challoo	Texas A&M University Kingsville (TX)	Anca Sala	Baker College (MI)
Isaac Chang	Illinois State University (IL)	Alex Sergeev	Michigan Technological University (MI)
Shu-Hui (Susan) Chang	Iowa State University (IA)	Mehdi Shabaninejad	Zagros Oil and Gas Company (IRAN)
Rigoberto Chinchilla	Eastern Illinois University (IL)	Hiral Shah	St. Cloud State University (MN)
Phil Cochrane	Indiana State University (IN)	Mojtaba Shivaie	Shahrood University of Technology (IRAN)
Curtis Cohenour	Ohio University (OH)	Musibau Shofoluwe	North Carolina A&T State University (NC)
Emily Crawford	Claffin University (SC)	Jiahui Song	Wentworth Institute of Technology (MA)
Dongyang (Sunny)Deng	North Carolina A&T State University (NC)	Carl Spezia	Southern Illinois University (IL)
Z.T. Deng	Alabama A&M University (AL)	Michelle Surerus	Ohio University (OH)
Sagar Deshpande	Ferris State University (MI)	Harold Terano	Camarines Sur Polytechnic (PHILIPPINES)
Marilyn Dyrud	Oregon Institute of Technology (OR)	Sanjay Tewari	Missouri University of Science & Techn (MO)
Mehran Elahi	Elizabeth City State University (NC)	Vassilios Tzouanas	University of Houston Downtown (TX)
Ahmed Elsayy	Tennessee Technological University (TN)	Jeff Ulmer	University of Central Missouri (MO)
Cindy English	Millersville University (PA)	Abraham Walton	University of South Florida Polytechnic (FL)
Ignatius Fomunung	University of Tennessee Chattanooga (TN)	Haoyu Wang	Central Connecticut State University (CT)
Ahmed Gawad	Zagazig University (EGYPT)	Jyhwen Wang	Texas A&M University (TX)
Hamed Guendouz	Yahia Farès University (ALGERIA)	Boonsap Witchayangkoon	Thammasat University (THAILAND)
Kevin Hall	Western Illinois University (IL)	Shuju Wu	Central Connecticut State University (CT)
Mohsen Hamidi	Utah Valley University (UT)	Baijian "Justin" Yang	Purdue University (IN)
Mamoon Hammad	Abu Dhabi University (UAE)	Eunice Yang	University of Pittsburgh Johnstown (PA)
Gene Harding	Purdue Polytechnic (IN)	Xiaoli (Lucy) Yang	Purdue University Northwest (IN)
Bernd Haupt	Penn State University (PA)	Hao Yi	Chongqing University (CHINA)
Youcef Himri	Safety Engineer in Sonelgaz (ALGERIA)	Faruk Yildiz	Sam Houston State University (TX)
Delowar Hossain	City University of New York (NY)	Yuqiu You	Ohio University (OH)
Xiaobing Hou	Central Connecticut State University (CT)	Hong Yu	Fitchburg State University (MA)
Shelton Houston	University of Louisiana Lafayette (LA)	Pao-Chiang Yuan	Jackson State University (MS)
Ying Huang	North Dakota State University (ND)	Jinwen Zhu	Missouri Western State University (MO)
Christian Bock-Hyeng	North Carolina A&T University (NC)		
Pete Hylton	Indiana University Purdue (IN)		
John Irwin	Michigan Tech (MI)		
Toqeer Israr	Eastern Illinois University (IL)		
Sudershan Jetley	Bowling Green State University (OH)		
Alex Johnson	Millersville University (PA)		
Rex Kanu	Purdue Polytechnic (IN)		
Reza Karim	North Dakota State University (ND)		
Manish Kewalramani	Abu Dhabi University (UAE)		
Tae-Hoon Kim	Purdue University Northwest (IN)		
Chris Kluse	Bowling Green State University (OH)		
Doug Koch	Southeast Missouri State University (MO)		
Mohan Krishna	Vidyavardhaka College of Eng. (INDIA)		
Resmi Krishnankuttyrema	Bowling Green State University (OH)		
Zaki Kuruppallil	Ohio University (OH)		
Shiyong Lee	Penn State University Berks (PA)		
Soo-Yen (Samson) Lee	Central Michigan University (MI)		
Chao Li	Florida A&M University (FL)		
Jiliang Li	Purdue University Northwest (IN)		
Zhaochao Li	Morehead State University (KY)		
Dale Litwhiler	Penn State University (PA)		
Mani Manivannan	ARUP Corporation		
G.H. Massiha	University of Louisiana (LA)		
Thomas McDonald	University of Southern Indiana (IN)		
David Melton	Eastern Illinois University (IL)		
Shokoufeh Mirzaei	Cal State Poly Pomona (CA)		
Kay Rand Morgan	iCloud.com		
Sam Mryyan	Excelsior College (NY)		
Jessica Murphy	Jackson State University (MS)		

# COMPUTATIONAL FLUID DYNAMICS SIMULATION OF INHALED SUBMICRON BIOAEROSOL PARTICLE FLOW AND DEPOSITION IN THE HUMAN LUNG

Mohammed Ali, The University of Texas at Tyler

## Abstract

In this study, the authors used computational fluid dynamics modeling and simulation to evaluate the mechanistic phenomena of inhaled submicron bioaerosol particles flowing through surrogate, in-silico human respiratory airways. The phenomena investigated included the effects of four aerodynamic and electromechanical mechanisms: 1) inertial impaction (IIP), 2) Brownian diffusion (BD), 3) gravitational sedimentation (GS), and 4) electrostatic charge forces (ECF) that interact with inhaled particles. A commercial, finite-volume code, ANSYS Fluent, enhanced with user-supplied programs in Visual C++, was employed. Tracheobronchial (TB) geometry was developed using ANSYS Design-Modeler and morphological lung dimensions specified in Ewald R. Weibel's model of dichotomous lung morphometry. Simulation results were compared with established mathematical models for inhaled bioaerosol particles' IIP, GS, and ECF depositions. Although, the IIP is still a dominant deposition mechanism for submicron particles in the TB airways under light physical activity breathing conditions ( $Q = 28.3$  l/min), the BD, GS, and particle intrinsic electrostatic charge may play several roles as well. Moreover, the GS was found to be negligible for smaller particle sizes ( $d_p < 1\mu\text{m}$ ), whereas it became dominant for larger particles ( $d_p > 1\mu\text{m}$ ). The occurrences of IIP caused the deposition of "hot spots" in the bifurcating airway where sharp bends existed. The GS had fifteen times stronger deposition effects on a  $10\mu\text{m}$  particle than on a  $1\mu\text{m}$  particle. A 50 percent increase in electrostatic charge per particle can double its deposition probability as well. Smaller charged particles ( $d_p \leq 1\mu\text{m}$ ) experience higher (one-log) image forces than larger particles ( $d_p \geq 10\mu\text{m}$ ), while carrying the same number of elementary charges.

## Introduction

Respiratory inhalation of in-silico studies can be the basis for assessing the potential risks of workplace exposure to ultrafine bioaerosol particles. Predicting the amount of these particles' deposition in healthy or diseased lung tissue following exposure is the major first step toward evaluating risks associated with exposure to airborne microorganisms and subsequent respiratory distress. Since upper airway deposition in lungs determines the effectiveness of inhaled particles, knowing their quantity may contribute in this endeavor (Farghadan, Poorbahrami, Jalal, Oakes, Coletti, & Arzani, 2020; Usmani, Biddiscombe, & Bames, 2005).

An aerosol is defined as a suspension system of solid or liquid particles in a gas. The major physical properties of respiratory drug aerosol particles include the particle's size (diameter), shape, diffusivity, density, and electrostatic charge (Hinds, 2012). Bioaerosols are airborne particles of biological origin, including viruses, bacteria, fungi, and all varieties of living matter. The prospective applications of bioaerosol in research and industry include: 1) dose determination of respiratory drugs to treat asthma and other chronic obstructive pulmonary diseases (COPD), 2) inhalation toxicity from personal exposure in the workplace, 3) manufacturing of protective devices in industrial ergonomics, and 4) protective actions taken to combat bioterrorism mass catastrophes. However, in-vitro experimental studies of particle deposition in realistic lung airways have been limited, due to regulatory and safety restrictions. To overcome these constraints, researchers adopt numerical simulations, including computational fluid dynamics (CFD) (Hofmann, 2011).

The main mechanisms of lung deposition of inhaled respirable bioaerosol particles in the lung involve four mechanisms: 1) inertial impaction (IIP), denoted by  $D_i$ ; 2) Brownian diffusion (BD), denoted by  $D_{bd}$ ; 3) gravitational sedimentation (GS), denoted by  $D_g$ ; and 4) electrostatic charge forces (ECF), denoted by  $D_e$  (Hinds, 2012). Figure 1 illustrates all four of these distinctive deposition mechanisms.

## Significance of Aerodynamic and Electromechanical Forces on Human Lung Airways

Equation 1 has been widely used to understand the effects of various forces on aerosol particle flow trajectories and deposition mechanisms in the respiratory airway. It is called the Euler-Lagrange particle transport (ELPT) equation (Ouellette, Xu, & Bodenschatz, 2006).

$$F_t = m_p \frac{du}{dt} = \sum F_b + \sum F_e + \sum F_a + \sum F_{bd} \dots \dots \dots (1)$$

where,  $F_t$  is the total force on a particle in the aerosol stream,  $m_p$  is the particle mass,  $u(t)$  is the particle velocity,  $F_b$  is the body force—such as inertial impaction and gravitational sedimentation,  $F_e$  is the surface force—such as electrostatic space and image forces,  $F_a$  is the adhesive force—such as van-der Waals and capillary forces, and  $F_{bd}$  is the Brownian diffusive force.

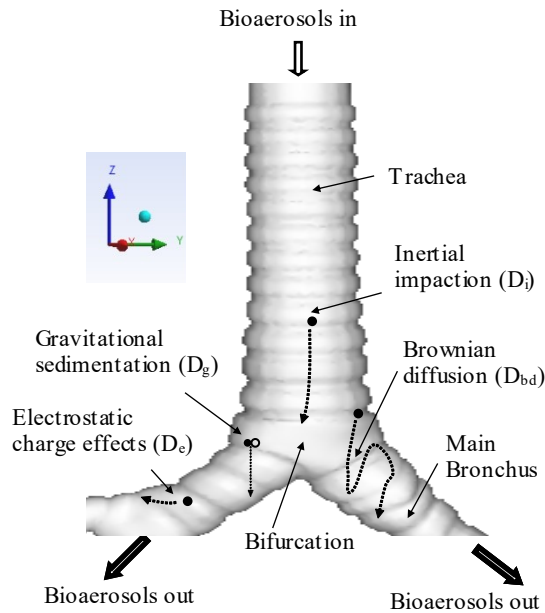


Figure 1. CFD simulation of human tracheobronchial airways. Various aerodynamic and electrotechnical forces may be involved in these mechanisms.

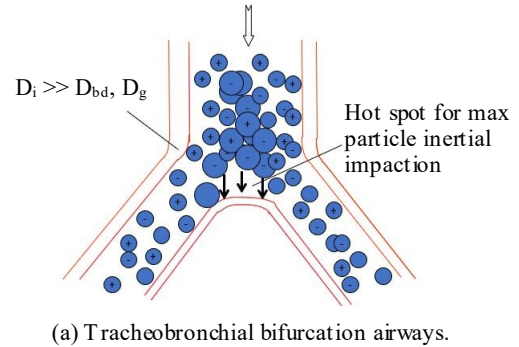
Engineering principles may further explain these forces with respect to the bioaerosol flow inside lung airways. For example, inertial impaction force is a part of a body's force acting on submicron particles, as depicted by the ELPT equation. Figure 2(a) shows that this occurs mainly when a particle is unable to adjust to abruptly changing streamlines, a phenomenon that creates a high probability of larger biological particles ( $d_p$ ), which are greater than  $0.5\mu\text{m}$ , to deposit in tracheobronchial (TB) bifurcation. Moreover, a particle's impaction force is determined by its Stokes number ( $Stk$ ) and Dean number ( $De$ ), which are mathematically defined by Equation 2:

$$Stk = \frac{\rho_p d_p^2 C_c U_0}{18\mu D} \text{ and } De = Re \left( \frac{R}{R_c} \right)^{1/2} \dots \dots \dots (2)$$

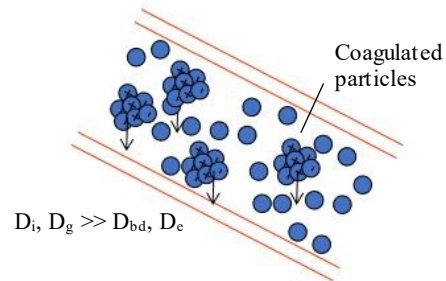
where,  $\rho_p$  is the particle density,  $d_p$  is the particle size or aerodynamic diameter,  $C_c$  is the Cunningham correction factor,  $\mu$  is the fluid viscosity,  $U_0$  is the mean fluid velocity,  $D$  is the airway bifurcation diameter or curvature in carina,  $Re$  is the Reynolds number,  $R$  is the radius of the daughter branch, and  $R_c (D = 2R_c)$  is the branch radius of curvature.

Figures 2(b) and 2(c) show that the deposition mechanism GS is prominent in the distal respiratory airways and very active when particles grow due to agglomeration for coulombic attraction for having positive and negative charges (Hinds, 2012). The BD also becomes very effective on ultrafine particles (UFPs), when flowing through distal respiratory airways. The electrostatic image charges exert effects on conductive walls and cause charged particles to be de-

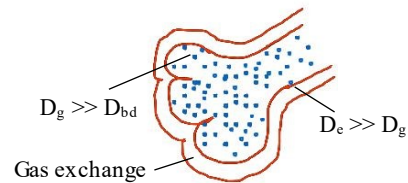
posited. In Alveoli, longer breath-holding time favors GS, and the charged UFPs experience electrostatic image force deposition. The electrostatic space charge force causes repulsion of unipolar charged particles and coagulation of bipolar charged particles (Ali, 2009). Then IIP or GS causes particles to deposit.



(a) Tracheobronchial bifurcation airways.



(b) Inertia and gravity are dominant forces in the bronchiolar airway for larger and coagulated particles.



(c) Longer residence time favors gravitational sedimentation and charged particles favor electrostatic image force depositions in the Alveoli, the distal regions of lung.

Figure 2. Illustrations of aerodynamic and electromechanical mechanism effects with respect to various regions of the lung.

CFD is a computer-based software that simulates the aerosolized fluid flow through ELPT and Navier-Stokes fluid dynamics equations. It has been established as a powerful tool for tracing dispersed-phase flows of submicron particles in lung airways (Minard, Kuprat, Kabilan, Jacob, Einstein, Carson, & Corley, 2012). With these understandings, the objective of the present study was the application of computational simulations to analyze inhaled bioaerosol particle transport and deposition in human lung airways, as

it was expected that findings would lead to the development of appropriate drug doses to treat asthma and COPD, severity of inhalation toxicity, and manufacturing of protective devices in industrial ergonomics and bioterrorism mass prophylaxis.

## Materials and Methods

In this study, the author employed a commercial finite-volume code, ANSYS Computational Fluid Dynamics Fluent, enhanced with user-supplied programs in Visual C++ for bioaerosol particles tracking and deposition pattern (ANSYS, 2016). Figure 3 shows the simplified illustrations of the simulated dichotomous branching of lung morphology. Its dimensions were adopted from Ewald R. Weibel's model that was implemented to construct lung geometry using ANSYS CFD's Design-Modeler (Weibel, 1963). The main focus of this study was the interactive effects of aerodynamic and electro-mechanical forces in the upper tracheo-bronchial (TB) airway model featuring actual geometry of two generations after mouth-throat, where the trachea and main bronchus are located. They are the first and second generations of the lung, respectively.

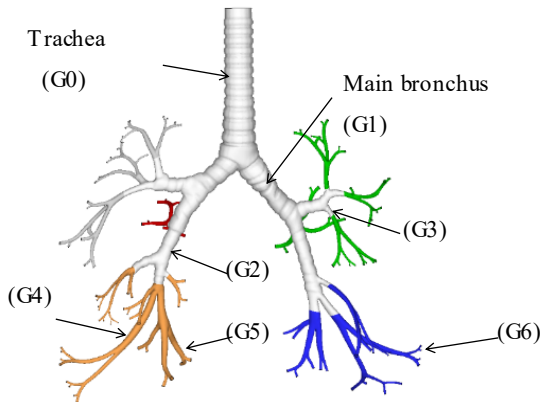


Figure 3. Simulated simplified dichotomous morphology of the human lungs' seven generations from trachea G0 to terminal bronchioles G6.

In order to understand entire human respiratory system functionally with respect to anatomical and physiological perspectives, it can be divided into two zones. They are the conducting zone, which includes nose to bronchioles to form a route for conduction of the inhaled air/bioaerosols, and respiratory zone, which includes respiratory bronchioles to alveolar sacs where the gas exchange takes place. Additionally, the system was partitioned into twenty-four generations of dichotomous branching for ease of function analysis. In such orderly branching fashion, trachea were indexed as generation 0 (G0), main bronchus (G1), and the last order of terminal bronchioles was generation 23 (G23). Each airway was divided into dichotomous branching or two smaller daughter airways at every generation (Weibel, 1963). Table 1 summarizes the various airway-specific parameters.

Table 1. Human lung upper airway morphometric data.

Parameter	Trachea	Main Bronchus
Airway generation index	0	1
Number of airways	1	2
Airway diameter (cm)	1.8	1.22
Airway length (cm)	12.00	4.76
Flow velocity (cm/s)	393.17	201.99
Flow percent of all inhaled	100%	50%
Flow Reynolds number	2213	1634

The  $k-\omega$  turbulence method of the CFD was used to simulate the turbulent flow of aerosols in the realistic lung airway. A  $K-\omega$  model of turbulence can incorporate turbulence parameters very close to boundary or near wall region. If one were interested in capturing the phenomena of pressure gradients and separating flow in such a region, which was the case for this study, the  $K-\omega$  model becomes handy. The applications of this popular eddy-viscosity-based model in similar studies were demonstrated in similar studies (Ruzycki, Javaheri, & Finlay, 2013; Kleinstreuer, & Zhang, 2010; Menter, 1994). The CFD Design Modeler-built human airway was in the form of an unstructured polyhedral grid mesh, and a high-mesh density was observed near the airway wall. Figure 4 shows that a high-fidelity computational mesh is a powerful means of understanding structure-function relationships in the lungs.

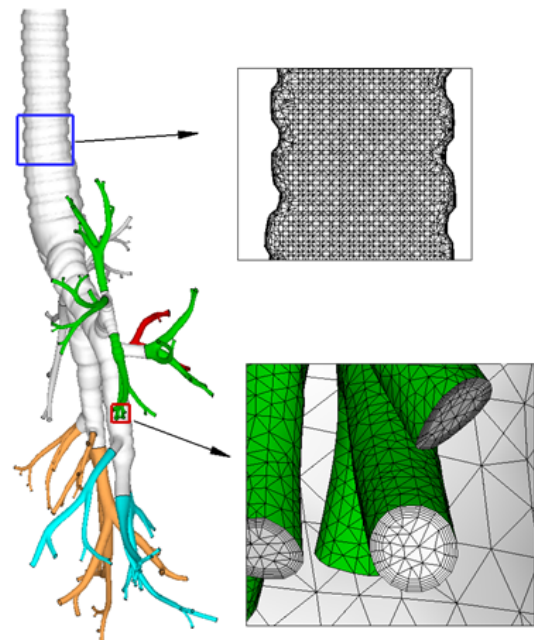


Figure 4. Illustrations of high-fidelity polyhedral computational mesh to mimic realistic lung airways.

As elucidated earlier, the CFD simulations were performed in order to quantify airflow velocity particle flow, transport, and deposition patterns for steady inhalation in the TB airway tree of an adult lung. The effect of turbulence flow was accounted for by using a large eddy simulation. Up until now, considerable efforts have been made to develop advanced techniques for measuring dynamics of aerosolized flow (a solid suspended in gas) on fluidized beds (van Ommen, Sasic, van der Schaaf, Gheorghiu, Johnson, & Coppens, 2011). Although it was computationally challenging in the past to measure the dense bioaerosol flow properties of several thousand particles, current CPU processing power make it possible for multiphase CFD-DPM (computational fluid dynamics-discrete particle model) simulations to provide insight on the behavior of 50,000–100,000 particles on fluidized beds. This technique can use an aerosolized fluid mesh that is much smaller than the particles for precise simulation (Greifzu, Kratzsch, Forgber, Lindner, & Schwarze, 2016).

Like other studies, the major lung function parameters common for both trachea and main bronchus were an inhalation flow rate of 28.3 l/min, forced expiratory volume and forced vital capacity ratio within five percent, an air density of 1.18 kg/m<sup>3</sup>, bioaerosol viscosity of 1.82 x 10<sup>-5</sup> Pa.s, and bioaerosol particle density of 1.0 g/cm<sup>3</sup> (Thomas, Guppy, Straus, Bell, & Glasziou, 2019; Kadota, Inoue, Matsunaga, Takemiya, Kubo, Imano, Uchiyama et al., 2019). The intrathoracic or lung deposition fraction (DF) was defined as the ratio of the particles deposited in any airway (during both inhalation and exhalation) to the particles entering it. The DF was quantified for the case-control model over a range of particle sizes from 0.1 to 10µm.

## Results and Discussion

The inhalation flow rate of bioaerosols is 28.3 l/min—according to the Food and Drug Administration (FDA) guidance, and American Society for Testing and Standards (ASTM) method (ASTM, 2001)—was used to validate the simulation of the realistic fundamental lung-airway functions. The exit bioaerosol flow rate can be defined as the proportion of exhaled-to-inhaled volume of bioaerosols (Heistracher & Hofmann, 1997). A CFD analysis revealed the effects of aerodynamic and electromechanical forces (IIP, BD, GS, and ECF) on bioaerosol particle transport, flow, and deposition fraction in realistic lung airways. Figure 5 illustrates the cross-sectional contours of bioaerosol particle flow and velocity vector in the tracheal airway region. In the instantaneous bioaerosol flow appearance, several vortices were observed under the flow pattern regime.

Note that the bioaerosol flow recovered rapidly in the entrance region of the daughter airways and, thus, became fully developed at the outlets of the bifurcation regions. Simulation patterns were in good agreement with those reported by Kadota et al. (2019). Thick boundary layers formed near the tracheal cartilages that enhanced particles

reach to the airway surfaces, and consequently deposited there. Figure 6 illustrated the fully developed flow characteristics and particle progression at various particle times.

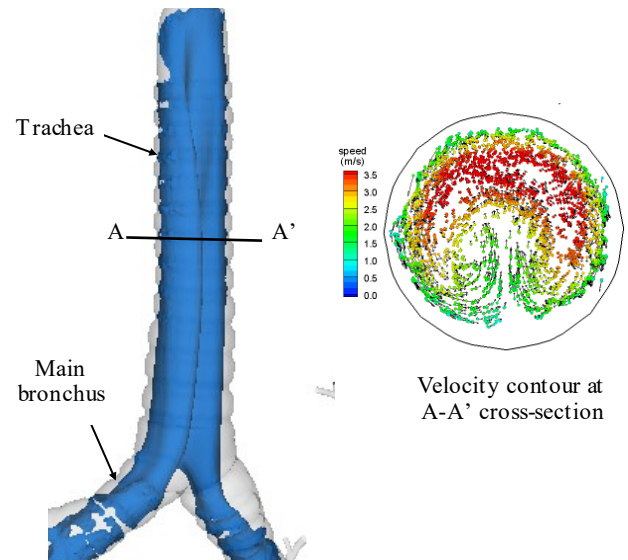


Figure 5. Simulated bioaerosol particles flow progression and velocity contour of the A-A' cross-section.

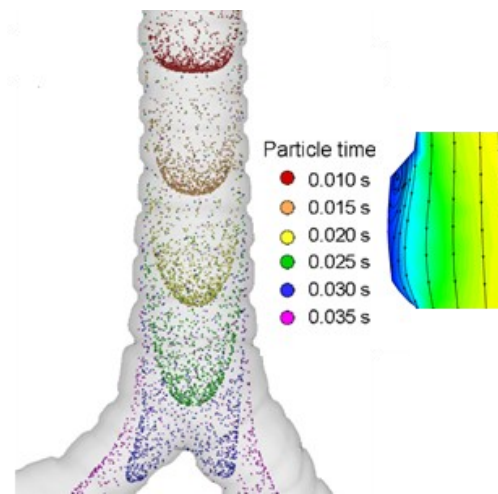


Figure 6. Simulated fully developed bioaerosol particles flow progression at various instances.

Numerical simulation using an ELPT expression to calculate the disposition fraction of the submicron bioaerosol particle due to inertial impaction in the TB airways shows comparable results with the theoretical prediction model by Martonen (1993); Figure 7 shows that graphical representation. Deposition fraction was found to be proportional to particle size and in agreement with previous studies in the literature (Fuchs, 1964). For fine particles in the size range of 1-10µm, the Brownian diffusive process was thought to be insignificant, but GS and IIP forces were more effective in causing them to be deposited in the airway. This phenom-

enon can be explained by the concept that these particles carry far more mass than submicron particles. It is noteworthy that these particles play an important role in a variety of physiological processes. As a consequence of environmental exposure, for example, bacteria or other biological organisms of this size range may enter the lung in aerosolized form and cause disease.

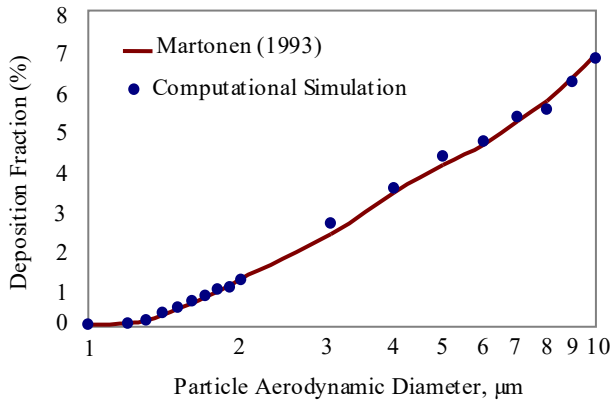


Figure 7. Comparison of bioaerosol particles deposition in the TB airway, due to inertial impaction with the reported literature.

In the same fashion, numerical simulation using an ELPT expression to calculate the disposition fraction of the submicron bioaerosol particle due to GS in the TB airways showed comparable results with the theoretical prediction model by Pich (1972); Figure 8 shows that graphical representation.

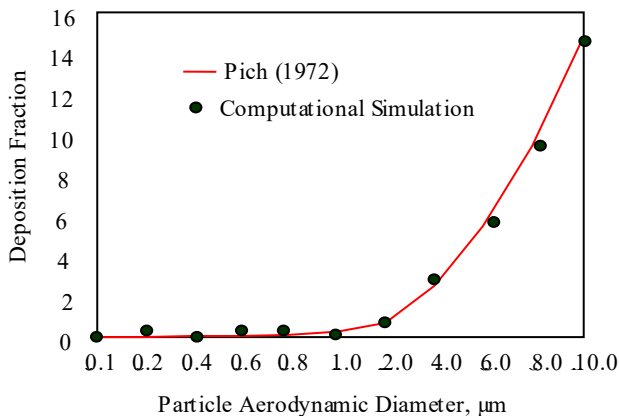


Figure 8. Comparison of bioaerosol particles deposition in the TB airway, due to gravitational sedimentation with the reported literature.

Figure 6 illustrates that the simulation results estimated that the deposition efficiency due to IIP was extremely low (<1%) for a particle size smaller than 2 $\mu$ m. Similarly, Figure 7 shows that the deposition efficiency due to GS was also very low for particles smaller than 2 $\mu$ m but which became significant for larger particles.

Figure 9 exemplifies the comparable deposition probabilities of same size particles due to GS or ECF. Here, the mathematical simulation demonstrated that the deposition fraction of coarser particles was governed by GS, irrespective of the inherent electrostatic charge of the particles.

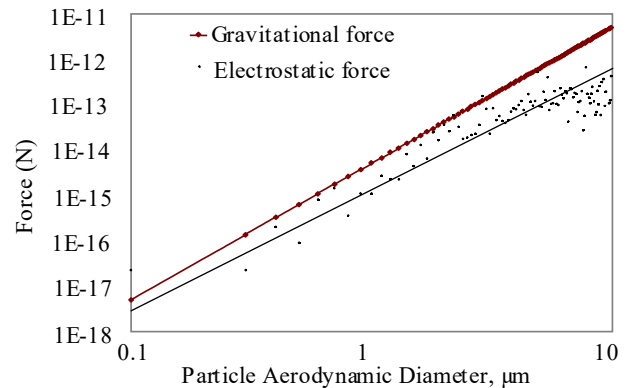


Figure 9. Comparison of gravitational sedimentation and electrostatic forces measured for particles between 0.1 $\mu$ m and 10 $\mu$ m in size.

One may notice that the electrostatic charge is a very important property of an experimental or ambient bioaerosol, as it may influence the particle behavior in lung deposition. The particle's charge-to-mass ratio (denoted by  $q/m$ ) reflects a very accurate understanding about its deposition behavior (Yu, 1977). The smaller the particle size, the larger  $q/m$  experiences higher electrostatic image charge force compared to the same amount of charge for a larger particle. These results were comparable with the lung depositions reported by Darquene (2014) for gravity force and Yu (1988) for electrostatic charge force. Figure 10 presents a comparison between the depositions due to different ECFs. As illustrated in the figure, the 0.1 $\mu$ m particle's probability of deposition was about 18 percent, whereas the 1 $\mu$ m particle's deposition probability was about 4 percent. In general, then, a 50 percent increase in the elementary charge approximately doubles the deposition probability for the range -2.5 $\mu$ m) of particle size distribution.

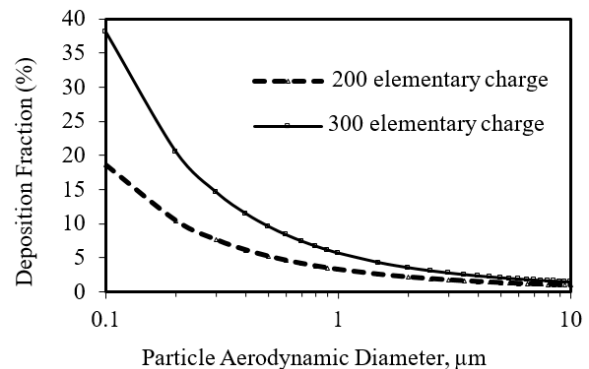


Figure 10. Comparison of electrostatic charge deposition fractions for the same sized particle with different elementary charges (1 elementary charge =  $1.6 \times 10^{-19}$  Coulomb).

The reasonable limitations of this work are recognized here. The CFD simulated a sinusoidal breathing pattern that consisted of an idealized approximation of more realistic wave formation in the lung. Such methodology for the field decomposition assumed uniform ventilation across the TB generations, which might be less realistic, especially in the case of COPD or in the deep lung where air ventilation is altered due to constriction by asthma or cystic fibrosis. Additionally, airflow recovery was assumed to fully develop within the branches downstream of the bifurcation carina. While in general these are reasonable, assumptions can be applied, depending on bioaerosols flow rate. This assumption may not hold true in the lower part (beyond TB regions) of the respiratory airway tree.

## Conclusions

From this current study, the authors predicted bioaerosol particle deposition fractions during a full breathing cycle in a simplified approximation of the tracheobronchial tree, and presented here the first two generations of the human lung. The IIP and GS had roughly 107- and 10-times stronger deposition effects, respectively, on a 10 $\mu$ m particle than that of a 1 $\mu$ m particle. Aerodynamic and electrodynamic motions, such as velocity and electrical mobility, gravitational forces, and weak forces such as van der Waals and adhesive in the lungs' TB airway, vary with respect to the particle's aerodynamic size. A 50 percent increase in electrostatic charge of a bioaerosol particle can enhance deposition probability two times. Smaller ( $d_p < 1\mu$ m) charged particles experienced higher image force than a larger ( $d_p > 5\mu$ m) particle, while carrying the same number of elementary charges. The proposed methodology can be employed in future studies to mimic the drug or other UFP deposition in diseased lung models. Such a study can be achieved by replacing the current healthy bifurcation or acinus model geometries with diseased ones; that is, a pulmonary airway with constrictions or COPD-induced acinus morphology.

## Acknowledgments

The work reported in this paper was partly supported by a seed grant from the University of Texas at Tyler Office of Research and Scholarship.

## References

- Ali, M. (2009). Pulmonary drug delivery. In V. S. Kulkarni (Ed.), *Handbook of non-invasive drug delivery systems* (pp. 209-246). Amsterdam, The Netherlands: Elsevier.
- ANSYS, Inc. (2016). ANSYS Fluent User's Guide, Release 17.2. <https://www.ansys.com>
- ASTM. (2001). Standard test method for evaluating the bacterial filtration efficiency (BEF) of medical face mask materials, using a biological aerosol of *Staphylococcus aureus*. *Annals of ASTM Standards, F2101-01*, 1553-1557.
- Darquenne, C. (2014). Aerosol deposition in the human lung in reduced gravity. *Journal of Aerosol Medicine and Pulmonary Drug Delivery*, 27(3), 170-177.
- Farghadan, A., Poorbahrami, K., Jalal, S., Oakes, J. M., Coletti, F., & Arzani, A. (2020). Particle transport and deposition correlation with near-wall flow characteristic under inspiratory airflow in lung airways. *Computers in Biology and Medicine*, 120, 103703. doi:10.1016/j.compbiomed.2020.103703
- Fuchs, N. A. (1964). *The Mechanics of Aerosols*. Oxford, UK: Pergamon.
- Greifzu, F., Kratzsch, C., Forgber, T., Lindner, F., & Schwarze, R. (2016). Assessment of particle-tracking models for dispersed particle-laden flows implemented in Open FOAM and ANSYS FLUENT. *Engineering Applications of Computational Fluid Mechanics*, 10(1), 30-43.
- Heistracher, T., & Hofmann, W. (1997). Flow and deposition patterns in successive airway bifurcations. *Annals of Occupational Hygiene*, 41, 537-542.
- Hinds, W. C. (2012). *Aerosol Technology: properties, behavior and measurement of airborne particles*. (2nd ed.). New York: John Wiley & Sons Inc.
- Hofmann, W. (2011). Modelling inhaled particle deposition in the human lung—A review. *Journal of Aerosol Science*, 42(10), 693-724.
- Kadota, K., Inoue, N., Matsunaga, Y., Takemiya, T., Kubo, K., Imano, H. ...Tozuka, Y. (2019). Numerical simulations of particle behavior in a realistic human airway model with varying inhalation patterns. *Journal of Pharmacy and Pharmacology*, 72(1), 17-28. doi: 10.1111/jphp.13195
- Koullapisa, P. G., Hofemeierb, P., Sznitmanb, J., & Kassinos, S. C. (2018). An efficient computational fluid-particle dynamics method to predict deposition in a simplified approximation of the deep lung. *European Journal of Pharmaceutical Sciences*, 113(2), 132-144.
- Kleinstreuer, C., & Zhang, Z. (2010). Airflow and particle transport in the human respiratory system. *The Annual Review of Fluid Mechanics*, 42, 301-334.
- Martonen, T. B. (1993). Mathematical model for the selective deposition of inhaled pharmaceuticals. *Journal of Pharmaceutical Sciences*, 82(12), 1191-1199. doi:10.1002/jps.2600821202
- Menter, F. R. (1994). Two-equation eddy-viscosity turbulence models for engineering applications. *AIAA Journal*, 32(8), 1598-1605.
- Minard, K. R., Kuprat, A. P., Kabilan, S., Jacob, R. E., Einstein, D. R. Carson, J. P., & Corley, R. A. (2012). Phase-contrast MRI and CFD modeling of apparent 3He gas flow in rat pulmonary airways. *Journal of Magnetic Resonance*, 221, 129-138.
- Ouellette, N. T., Xu, H., & Bodenschatz, E. A. (2006). Quantitative study of three-dimensional Lagrangian particle tracking algorithms. *Experimental Fluids*, 40, 301-313. doi: 10.1007/s00348-005-0068-7

- 
- Pich, J. (1972). Theory of gravitational deposition of particles from laminar flows in channels. *Journal of Aerosol Science*, 3(5), 351-361.
- Ruzycki, C., Javaheri, E., & Finlay, W. (2013). The use of computational fluid dynamics in inhaler design. *Expert Opinion of Drug Delivery*, 10(3), 307-323.
- Thomas, E. T., Guppy, M., Straus, S. E., Bell, K., & Glasziou, P. (2019). Rate of normal lung function decline in ageing adults: a systematic review of prospective cohort studies. *BMJ Open*, 9(6), e028150. doi:10.1136/bmjopen-2018-028150
- Usmani, O. S., Biddiscombe, M. F., & Bames, P. J. (2005). Regional lung deposition and bronchodilator response as a function of  $\beta_2$ -agonist particle size. *American Journal of Respiratory and Critical Care Medicine*, 172, 1497-1504. doi:10.1164/rccm.200410-1414OC
- van Ommen, R., Sasic, S., van der Schaaf, J., Gheorghiu, S., Johnson, F., & Coppens, M. O. (2011). Time-series analysis of pressure fluctuations in gas-solid fluidized beds—A review. *International Journal of Multiphase Flow*, 37(5), 403-428.
- Weibel, E. R. (1963). *Morphometry of the Human Lung*. Berlin, Heidelberg: Springer-Verlag (pp 136-142).
- Yu, C. P. (1977). Precipitation of unipolarly charged particles in cylindrical and spherical vessels. *Journal of Aerosol Science*, 8, 237-241.
- Yu, C. P. (1985). Theories of electrostatic lung deposition of inhaled aerosols, *The Annals of Occupational Hygiene*, 29(2), 219-227.

## Biography

**MOHAMMED ALI** is an associate professor of industrial technology and industrial management at The University of Texas at Tyler. He earned his B.S. (Mechanical Engineering, 1992) degree from Chittagong University of Engineering and Technology, Bangladesh, M.E. (course work in Industrial and Production Engineering, 1993) from Bangladesh University of Engineering and Technology, Dhaka, MBA (Management of Technology, 1995) from Asian Institute of Technology, Bangkok, Thailand, MS (Computer Science, 2001) from Oklahoma City University, and Ph.D. (Applied Science – Manufacturing of Drug Delivery Devices, 2008) from the University of Arkansas at Little Rock. His research interests are: additive bio-manufacturing, learning pedagogy in technology and applied engineering curriculum, smart-manufacturing of drug delivery devices, modeling and bio-simulation of submicron- and nanoparticles flow and deposition in the lung airways. Dr. Ali may be reached at [mohammedali@uttyler.edu](mailto:mohammedali@uttyler.edu)

# INFLUENCE OF ANNEALING TREATMENT ON THE PROPERTIES OF LOW-TEMPERATURE SILICON NITRIDE FILMS PRODUCED BY INDUCTIVELY COUPLED PLASMA CHEMICAL VAPOR DEPOSITION

Qingzhou Xu, Morehead State University

## Abstract

Silicon nitride ( $\text{SiN}_x$ ) thin films were synthesized at  $170^\circ\text{C}$  by inductively coupled plasma enhanced chemical vapor deposition. The as-deposited  $\text{SiN}_x$  films were found to suffer high-density fixed charges and interface charge traps. In this study, the author worked to improve the properties of the as-deposited  $\text{SiN}_x$  films using an annealing treatment. The chemical, physical, and electrical properties of the annealed  $\text{SiN}_x$  films were characterized and compared with those that were as-deposited. The concentrations of both N-H and Si-H bonds decreased, while a small concentration of Si-O bonds did form after annealing. No considerable changes were observed in the density-voltage (J-V) behavior, with the more drastic changes occurring in the capacitance-voltage (C-V) behavior. The flatband shift of the annealed films decreased significantly, revealing a drastic decrease in the fixed charge density. The interface state density of the annealed films was also reduced significantly. For 800W and 1000W  $\text{SiN}_x$  films, both the fixed charge and interface state densities decreased to acceptable levels. Based on composition and chemical bond analyses, the possible explanation for these improvements is that hydrogen atoms migrate to the interface and chemically react with the interface traps during annealing, making them electrically inactive. Overall, the annealed 800W silicon nitride film possessed the best combination of chemical, physical, and electrical properties, adequate for practical device applications.

## Introduction

Silicon nitride ( $\text{SiN}_x$ ) dielectric films have remarkable chemical, physical, mechanical, and electrical properties and are the materials of choice for barrier, insulation, passivation, and encapsulation layers for semiconductor devices and integrated circuits, wherever high-quality native oxides are not available (Andringa, Perrotta, de Peuter, Knoops, Kessels, & Creatore, 2015; Nyaupane, Bodas, Duttagupta, & Gangal, 2011; Shao et al., 2016; Cen et al., 2009; Stryahilev, Sazonov, & Nathan, 2002; Suzuki, Cervera, Ohnishi, & Takada, 2013; Heya et al., 2004; Huang et al., 2003; Jin, Prost, Neumann, & Tegude, 2004; Lee, Mackenzie, Johnson, Shul, Pearton, & Ren, 1998). The  $\text{SiN}_x$  films are made by plasma-enhanced chemical vapor deposition (PECVD) and low-pressure chemical vapor deposition

(LPCVD). The conventional PECVD method of a parallel-plate reactor is able to lower deposition temperatures to  $250\sim 350^\circ\text{C}$ , compared with  $500^\circ\text{C}$  needed by the LPCVD approach. However, the heat budget present in the conventional PECVD method is still too high for many emerging applications. Furthermore, as the substrate is placed on one of the two electrodes in the conventional PECVD reactor, the highly energetic bombardment of charged particles causes undesirable surface damages and high film stresses. As a result, there has been great interest recently in developing and utilizing low-temperature  $\text{SiN}_x$  films for a variety of applications in which low processing temperatures, surface damages, and film stresses are required.

Low-temperature  $\text{SiN}_x$  films have found wide applications, and two main areas of these applications are nontraditional substrates (Stryahilev, Sazonov, & Nathan, 2002; Parka, & Parsons, 2004; Hekmatshoara, Cherenack, Kattamis, Wagner, & Stum, 2008; Li, Nathan, Wu, & Ong, 2007; Sazonov, Strakhilev, Lee, & Nathan, 2005; Suzuki et al., 2013; Heya et al., 2004; Takano et al., 2005; Huang et al., 2003) and compound semiconductors (Jin et al., 2004; Lee et al., 1998; Lee et al., 1998; Lee et al., 1998; Jin, Neumann, Prost, & Tegude, 2005). One of the main interests in using nontraditional substrates is developing thin-film transistors (TFTs) and organic light-emitting diodes (OLEDs) on flexible plastics for light-weight, foldable displays. The maximum working temperatures of most of the plastics are in the range of  $100\sim 150^\circ\text{C}$  and, in some cases, even below  $80^\circ\text{C}$ . The poor electronic properties of the native oxides of III-V and II-VI compound semiconductors are well known. For example,  $\text{As}_2\text{O}_3$  is unstable thermodynamically in the presence of GaAs and reacts to form As.

Elemental As in turn produces near-mid-gap states that can pin down the Fermi level and enhances non-radiative recombination. Silicon dioxide films are prone to react with semiconductor compounds underneath and cause severe interface problems. In addition, III-V and II-VI semiconductor compounds are highly sensitive to ion bombardment and the non-congruent evaporation of volatile elements. The use of conventional PECVD  $\text{SiN}_x$  films is usually undesirable, due to the presence of high deposition temperatures and intense ion bombardment. The limitations associated with the existing techniques and those emerging demands give rise to the need for developing novel dielectric deposition techniques.

A number of deposition techniques have been developed to obtain high-quality  $\text{SiN}_x$  films at low temperatures, along with decreased surface damage and controlled film stresses. High-density plasma is the most effective approach to drive down deposition temperature. The evolving techniques based on using high-density plasma include electron cyclotron resonance plasma chemical vapor deposition (ECR-CVD) and inductively coupled plasma-enhanced chemical vapor deposition (IC-PECVD). In the ECR-CVD and IC-PECVD reactors, the deposition zones are purposely separated from the plasma generation zones. This provides the possibility of minimizing the surface damages, due to energetic ion bombardment. There had been extensive research on ECR-CVD (García, Martín, Martil, Fernández, & González-Díaz, 1998; Flewitt, Dyson, Robertson, & Milne, 2001; Bae, Farber, & Fonash, 2000; Delmotte, Hugon, Agius, & Courant, 1997; Hugon, Delmotte, Agius, & Courant, 1997; Pool, 1997; Isai, Holleman, Wallinga, & Woerlee, 2004). It is reported that silicon nitride, silicon oxide, and oxynitride films with good electrical properties can be deposited by the ECR-CVD technique at low temperatures down to room temperature. Nonetheless, there are a limited number of studies on IC-PECVD and its films' properties (Nyaupane et al., 2011; Zambona, & Mansano, 2003).

This current research study, then, was focused on characterizing the chemical, physical, and electrical properties of annealed low-temperature  $\text{SiN}_x$  films produced by IC-PECVD. It is part of the ongoing effort of developing high-quality dielectric thin films to passivate high electron mobility transistor (HEMT) integrated circuits at decreased temperatures and low ion bombardment. Lowering deposition temperatures makes it possible to avoid or minimize the alloying of the Schottky gate, the inter-diffusion and dopant redistribution of the multilayer structure, and the incongruous evaporation of volatile elements in HEMTs. From the perspective of minimizing the plasma-induced surface damages, a low microwave power deposition is preferred, but it may lead to poor-quality films due to less-thorough chemical reaction. Thus, three RF powers were used in this current study to evaluate the effect of deposition microwave power on the films' properties.

As revealed in the initial research results (Xu, Ra, Bachman, & Li, 2009), all the as-deposited low-temperature  $\text{SiN}_x$  films synthesized under three RF power condition were characterized with high-density fixed charges and interface charge traps, making the films unsuitable for practical device applications. In addition, lowering the deposition temperature favors the incorporation of hydrogen atoms. The migration of movable hydrogen atoms in the films results in long-term instability. As a result, a post-deposition annealing treatment is needed to decrease the defects produced in low-temperature deposition, improve the electrical properties, and mitigate the reliability concern. The focus of this study, then, was on the influence of the final device stability annealing treatment on the properties of low-temperature silicon nitride films.

## Experimental Methods

The silicon nitride films in this research were made on silicon wafers at  $170^\circ\text{C}$  by using inductively coupled plasma-enhanced chemical vapor deposition (IC-PECVD). Figure 1 shows a schematic diagram of the system. A 13.56 RF power source was inductively coupled into the tubular reactor with an antenna wound around it. Solenoidal magnets were uniformly distributed along the bottom of the reaction chamber, which would help to sustain a high dissociation rate. Prior to deposition, Si wafers were stripped of native oxides by using a dilute HF solution.  $\text{N}_2$  was used instead of  $\text{NH}_3$  in the deposition of silicon nitride films, thus increasing the likelihood of reducing the hydrogen concentration in the silicon nitride films. Hydrogen atoms were considered one of the reasons causing a change in long-term dielectric properties. The reaction chamber utilized two separated sets of gas inlets.  $\text{N}_2$  was injected into the chamber from the gas inlets at the top, and  $\text{SiH}_4$  was introduced by the side gas inlets that were radially distributed above the substrate chuck. Biasing of the substrate chuck was independent of the generation of plasma, and a null bias was used to decrease the surface damages that resulted from ion bombardment.

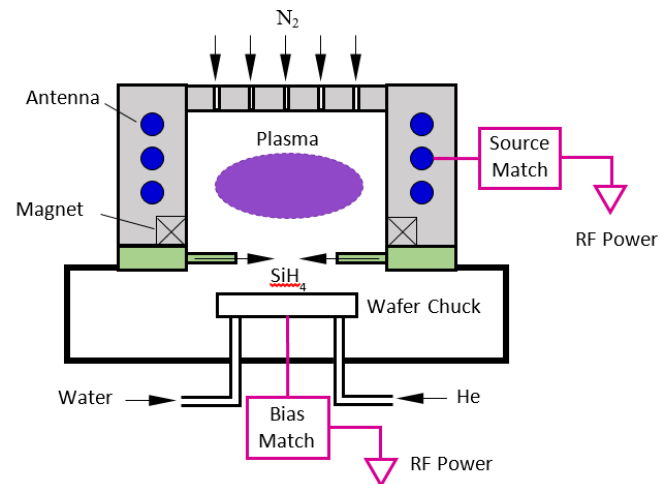


Figure 1. Schematic diagram of the ICPECVD reactor.

The  $\text{SiN}_x$  films were annealed at  $240^\circ\text{C}$  for 48 hours in protective gases, a standard procedure used to improve the long-term stability of high electron mobility transistors (HEMTs) and their IC circuits, especially for high-power and space applications. The chemical bonds of the low-temperature silicon nitride films were analyzed by Fourier transform infrared (FTIR) spectroscopy. The wet etching property of the films was tested in a commercialized, buffered oxide etch (BOE) solution at room temperature. The density of the pinholes was evaluated by KOH etching at  $70^\circ\text{C}$  for three hours. The surface roughness of the silicon nitride films was measured by using atomic force microscopy (AFM). The refractive index of the silicon nitride films was measured by using laser ellipsometry.

The electrical properties of the low-temperature silicon nitride films were measured using a metal-insulator-semiconductor (MIS) structure (Muller & Kamins, 1986; Nicollian & Brews, 1982; Sze, 1981). A mercury probe was used to make contact directly on the silicon nitride films to form an MIS structure for capacitance-voltage (C-V) measurements. Because meaningful quasi-static C-V curves were not successfully obtained, the high-frequency method was used to characterize the low-temperature silicon nitride films (Muller & Kamins, 1986). The dielectric constant of the films was determined by measuring metal-nitride-metal capacitance for calculating the ideal C-V curve of the MIS structure. High-frequency (1MHz) C-V measurements used a sweep rate of 0.1 V/s, starting from accumulation to strong inversion and then sweeping back. For current density-voltage (J-V) measurements, Ti/Cu films were e-beam evaporated and patterned to a series of square pads ranging from  $50 \times 50 \mu\text{m}^2$  to  $10 \times 10 \text{mm}^2$  by wet etching. These electrode pads of J-V measurements were randomly distributed on 4-inch silicon wafers so that the measured values would best represent the properties of the low-temperature silicon nitride films. The polarity was chosen in order to operate the MIS capacitors in accumulation so that a depletion zone in the semiconductor was avoided. Ti/Cu films were also deposited onto the backsides of the silicon wafers. Both C-V and J-V measurements were performed by using a B1500A Agilent semiconductor parameter analyzer.

## Results

The following are the experimental results of the influence of the post-deposition annealing treatment on the properties of the low-temperature silicon nitride films. Some relevant results in the as-deposited condition are included for the sake of comparison.

### Influence on Chemical Bonds

Figure 2 show the results of the chemical bonding structures for the low-temperature silicon nitride films, analyzed using Fourier transform infrared spectroscopy (FTIR). Except for the predominant absorption peak for the stretching vibration mode of the Si-N bond near  $840 \text{ cm}^{-1}$ , the other three major peaks are identified for the N-H stretching vibration mode ( $\sim 3340 \text{ cm}^{-1}$ ), the Si-H stretching vibration mode ( $\sim 2200 \text{ cm}^{-1}$ ), and the N-H bending vibration mode ( $1180 \text{ cm}^{-1}$ ). As mentioned previously, the low-temperature silicon nitride films were made using  $\text{N}_2$  and  $\text{SiH}_4$ . Although the N-H bond structure did not exist in the source gases, the N-H bonds were formed during the chemical reaction of the deposition process. There was a slight variation in the area of an absorption peak among the three power conditions. The peak area for the same bond and vibration mode decreased with increasing microwave power, a trend that was more apparent at the stretching vibration mode at  $3340 \text{ cm}^{-1}$  and the bending vibration mode at  $1180 \text{ cm}^{-1}$  of the N-H bond.

By comparing the spectra of the as-deposited and annealed silicon nitride films, the peak area at the same vibration mode for the chemical bond of N-H or Si-H decreased slightly after the annealing treatment. This was evident for the N-H stretching vibration mode at around  $3340 \text{ cm}^{-1}$  and the N-H bending vibration mode at  $1180 \text{ cm}^{-1}$ ; Figure 1(b) shows that these two peaks were almost indiscernible. After annealing, a trace of absorption occurred roughly between  $1070 \sim 1090 \text{ cm}^{-1}$ , and the location of this absorption peak coincided with that of the absorption peak of the Si-O stretching vibration mode. Because a trace for this kind of absorption was not observed in the measured spectra of the as-deposition films, a possible explanation could be that oxidation occurred during the annealing treatment.

For comparison, Figure 2 includes the measured result of a silicon nitride film made at  $250^\circ\text{C}$  by using a conventional parallel-plate reactor, PlasmaTherm 790 PECVD system, with the gas sources of  $\text{NH}_3$  and  $\text{SiH}_4$ . The absorption peaks of the N-H bonds were more pronounced for the PlasmaTherm film than for the low-temperature films. On the other hand, the absorption peaks of the Si-H bond were larger for the low-temperature films than for the PlasmaTherm film. This observation was in agreement with the fact that the low-temperature films were made of  $\text{N}_2$  and  $\text{SiH}_4$ , and that it was less likely for H atoms to exist in the form of an N-H bond.

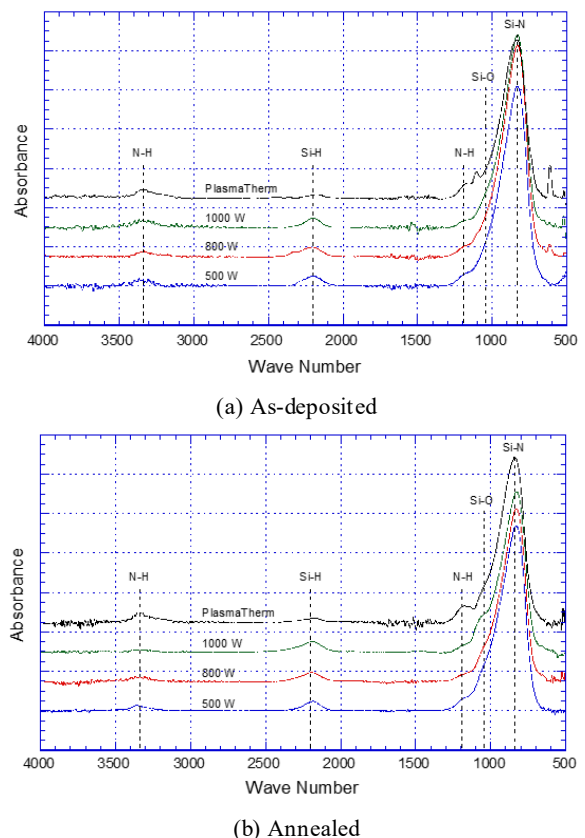


Figure 2. FTIR spectra of the silicon nitride films.

Since the area of an absorption peak was proportional to the concentration of the corresponding atomic bonds, several conclusions can be drawn from the FTIR analyses: the low-temperature silicon nitride films incorporate a lower concentration of N-H bonds but a higher concentration of Si-H bonds than the conventional PECVD film, or the low-temperature silicon nitride films have more Si-H bonds under a lower microwave power than under a higher microwave power. This may happen because, under a lower microwave power, the smaller disassociation rate of  $\text{SiH}_4$  favors more hydrogen retention in a form of Si-H. After annealing, the concentrations of both N-H and Si-H bonds decreased and, at the same time, a small concentration of Si-O bonds was formed. It is known that Si-H bonds in silicon nitride play a dominant role in determining the trapped electron density in the silicon nitride.

## Influence on Pin-Hole Density, Wet Etching Property, and Surface Roughness

Pinholes are tiny structural defects that can occur in thin dielectric films made by all kinds of chemical or physical vapor deposition techniques. In this current study, the pinholes were exposed through large etched pits on silicon wafer surfaces that were obtained by KOH etching at  $70^\circ\text{C}$  for three hours after which the silicon nitride films were removed by BOE. Figure 3 shows typical diamond-shaped etched pits that were taken from the edge area of a silicon wafer where there was higher pinhole density.

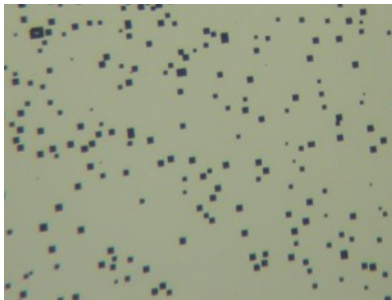


Figure 3. Etched pits on the Si wafer after the  $\text{SiN}_x$  film was stripped.

The density of pinholes depends on processing parameters and is also strongly related to the thickness of the dielectric film. For low-temperature silicon nitrides, when film thickness is larger than  $2000\text{\AA}$ , few pinholes can be seen. Thus, a  $750\text{\AA}$  film thickness was chosen in order to evaluate the differences in the density of pinholes between the three microwave power conditions. The results showed that, for each of the power conditions, the distribution of pinholes was not uniform on the wafer. The density of pinholes was much higher in the narrow edge region with a width of about  $0.5\text{ cm}$ . It was small and relatively uniform in the remaining central area but still had a measure of fluctuation. Figure 4 shows a comparison of the pinhole density in the films under three RF powers in the as-deposited and an-

nealed conditions. The result indicates that the annealing treatment had a limited impact on pinhole density. The small differences were largely likely due to counting errors.

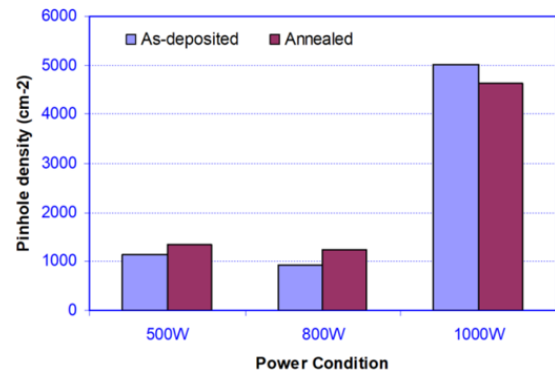
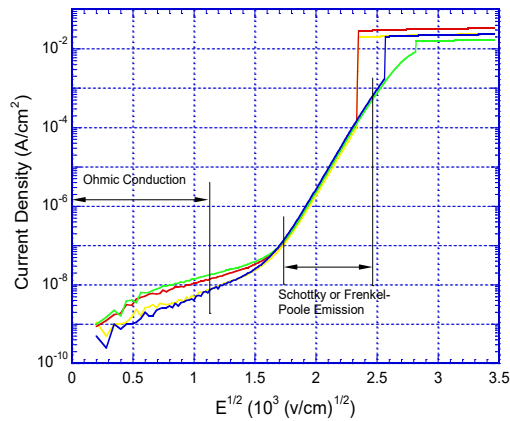


Figure 4. Pinhole densities in the as-deposited and annealed conditions.

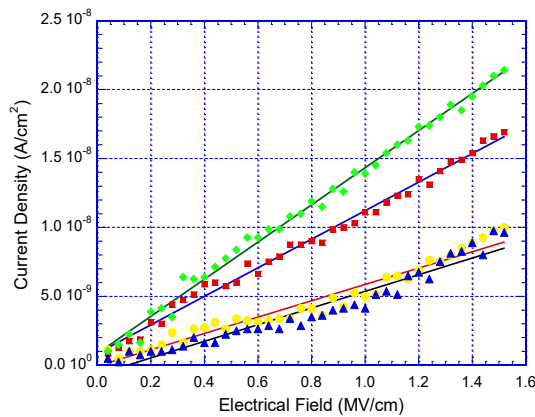
The wet etching property is closely related to composition, chemical bonding stability, and mass density of a dielectric film. The wet etching property of the low-temperature silicon nitride films in the as-deposited and annealed conditions was tested and compared in a commercialized BOE solution at room temperature. There were no observable differences in the wet etching rate in these films between the as-deposited and annealed conditions. The surface roughness of the films in the as-deposited and annealed conditions was also measured and compared by AFM, and the annealing treatment was found to have minimal impact.

## Influence on Breakdown Strength, Leakage Current, and Resistivity

Figure 5(a) shows a group of typical J-V curves for silicon nitrides. The figure uses a logarithm/square-root coordinate system for convenience to ascertain the electrical conduction mechanism. The curves were obtained from four  $200\text{ }\mu\text{m} \times 200\text{ }\mu\text{m}$  measurement electrode pads randomly distributed on an 800W,  $\text{SiN}_x$  film. A distinctive characteristic of the J-V curves is that the film experiences abrupt breakdown, a feature of avalanche breakdown. The breakdown does not happen at a precise value but rather in a range of electrical field strengths—from  $5.4$  to  $7.9\text{ MV/cm}$  for this specific sample. The average breakdown electrical field strength, based on these four measurements, was  $6.02\text{ MV/cm}$ . The J-V curves in Figure 5(a) can be divided into several distinct regions that can be associated with different mechanisms of electron conduction. The linear region in the high electrical field can be interpreted by the synergistic effect of Schottky and Frenkel-Poole electron emissions (Muller & Kamins, 1986; Nicollian & Brews, 1982; Sze, 1981). Figure 5(a) shows that, for both the Schottky and Frenkel-Poole emissions, the logarithm of the current density had a linear relationship with the square root of the electrical field.



(a) The complete curves on a logarithm and square-root coordinate.



(b) The low portions of the curves on a linear coordinate system.

Figure 5. J-V curves of a low-temperature silicon nitride films.

In the low electrical field, the electron emission mechanisms driven by high electrical fields were inactive; the movement of conductive carriers followed the ohmic law (Muller & Kamins, 1986; Nicollian & Brews, 1982; Sze, 1981). The current density had a linear relationship with the electrical field strength. Figure 5(b) shows that one can readily see the data in the low electrical field on a linear coordinate system of the current density and the electrical field, where the data points are the measurement values and the lines are the results of regression analysis. The data points of each measurement are evenly distributed along a straight line, confirming that ohmic conduction was the dominant conduction mechanism for the film in the low electrical field. The inverses of the slopes of the regression lines were the resistivity of the silicon nitride film, which possessed certain fluctuations for different electrode pads. The average resistivity of the silicon nitride film was calculated to be  $1.12 \times 10^{14} \Omega \cdot \text{cm}$ .

Between the ohmic conduction and Schottky/Frenkel-Poole emission regions is a transient region. Beyond the Schottky/Frenkel-Poole emission region, the silicon nitride film experiences avalanche breakdown. Leakage current was another important parameter for use of a dielectric film. Figure 5(a) shows that, with the exception of the regions after the dielectric's breakdown, the measured J-V curves from different electrode pads of the same size were coincident to one another. Thus, in contrast to the large fluctuation in breakdown strength, the leakage current had limited variation between the different electrode pads of an identical size. Because most field-effect devices work at an electric field strength of around 2MV/cm, the leakage current density at 2MV/cm is interesting for practical applications and is often used for comparison. At 2MV/cm, the leakage current density of the silicon nitride film was  $2.28 \times 10^{-8} \text{ A/cm}^2$ .

The breakdown electrical field strength—or breakdown strength—is a critical parameter of a dielectric film for practical utilization. The breakdown strength is an intrinsic material property determined by the dielectric film itself. However, due to the presence of a fringe electrical field, pinholes, or other imperfections, the measured values of breakdown strength varied with the size of the electrode pads used for measurement as well as the thickness of the dielectric film (thickness was not considered here). The influence of electrode pad size on breakdown strength, ignored in reporting dielectric properties in the majority of the published literature, was carefully evaluated in this current study. The author also attempted to determine the root cause for the breakdown of the low-temperature silicon nitride films. Figure 6 shows the measured J-V curves from the different electrode pads on the same silicon nitride film that was made under the 800W power condition. The measured breakdown strength increased with a decrease in the size of the electrode pad for the same silicon nitride film. This result revealed that it is important to compare and judge the dielectrics' properties by using the measured values from the measurement electrode pads of an identical size. This was used as the criterion when comparing the properties of the low-temperature silicon nitride films in this study.

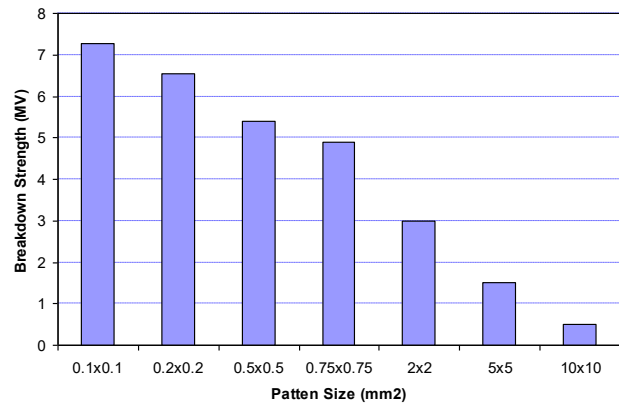


Figure 6. Breakdown strengths of different-size measurement electrode pads.

The breakdown strength, leakage current, and resistivity of the silicon nitride films in the annealed condition were measured and compared with those in the as-deposited condition. The measured results indicated that the annealing treatment has a negligible influence on each of these three properties. Figure 7 shows the influence of annealing treatment on the breakdown strengths of the SiN<sub>x</sub> films made in the 500W, 800W, and 1000W power conditions. The variations of breakdown voltage had no clear trend and were not significant.

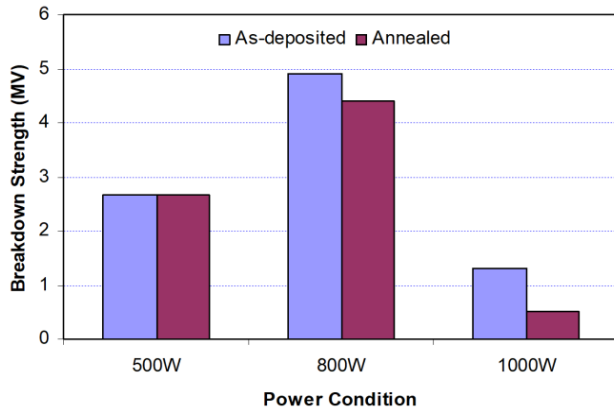
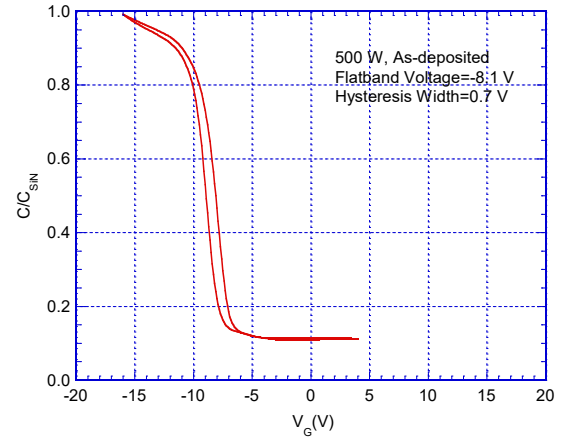


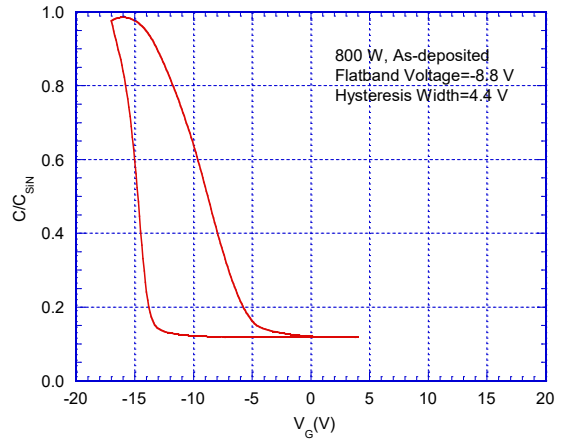
Figure 7. Breakdown strengths of the as-deposited and annealed SiN<sub>x</sub> films.

## Influence of Interface Charge Trap Levels and Fixed Charges

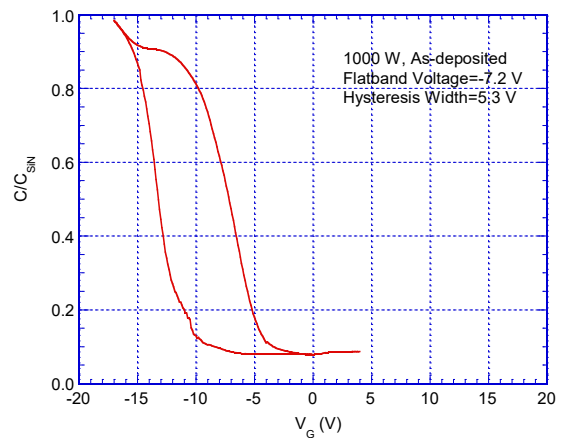
There are two types of defects related to the imperfect chemical bonding structure of a dielectric film: fixed charges and interface traps. Fixed charges refer to localized charge centers that cannot change their charge states under the influence of an external electrical field. Interface traps refer to the interface sites that can change their electrons' occupancy through an exchange of mobile carriers under the influence of an external electrical field. Each interface trap has one or more energy levels. Because the chargeable interface sites are not close enough to one another to create a continuous energy band, they form a series of discrete energy levels within the silicon's bandgap. As a result, interface traps are quantified as an interface trap level density per electron volt, which varies with the location in the bandgap. Interface trap levels below the Fermi level are full, and those above are empty. The density of interface trap energy levels is measurable near mid-gap of the silicon bandgap. Both fixed charges and interface traps must be controlled and minimized, otherwise they can adversely affect device performance. Figure 8 shows the measured C-V curves of the as-deposited silicon nitride films that were produced under the three microwave power conditions of 500W, 800W, and 1000W. The figure also includes the values of flatband shift and hysteresis width for each of the curves. Each of these three curves had a significant flatband shift, indicating the presence of high-density fixed charges.



(a) 500W



(b) 800W



(c) 1000W

Figure 8. C-V curves of the as-deposited, low-temperature silicon nitride films produced at different microwave powers.

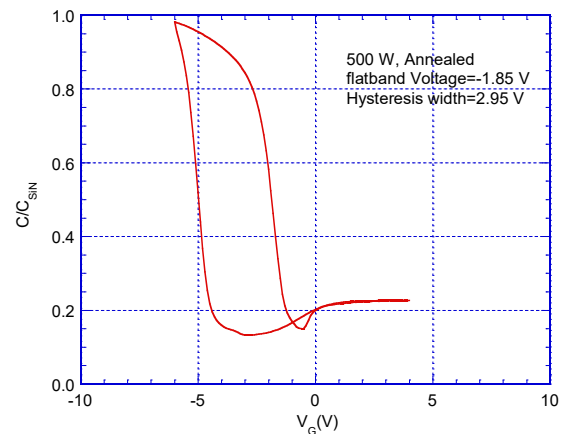
The silicon nitride films made at 500 W and 1000 W were hardly able to reach the saturated capacitance at accumulation, indicating the existence of high-density interface trap levels near the edge of the silicon bandgap. These chargeable interface traps effectively screen out the external electrical field and prevent the silicon's surface layer from reaching accumulation. There were significant differences in the hysteresis width. The hysteresis observed was related to the charge capture/release processes of the interface traps with a large time constant (i.e., the sluggish interface traps). The charge state of the sluggish interface traps cannot follow, but rather lags behind the change in gate bias, leading to hysteresis. The narrow hysteresis of the high-frequency C-V curve of the 500 W silicon nitride film indicated a low level of sluggish traps at the SiN<sub>x</sub>/Si interface. The non-symmetry in hysteresis of the 800 W's C-V curve was due to the fact that the kinetics of charge capture/release is asymmetrical and the capacitance value depends on the direction of the bias voltage variation. The curves of Figure 7 show how the densities of fixed charges and interface charge traps were calculated. Table 1 summarizes the calculated results of the as-deposited silicon nitride films produced under the three microwave conditions.

Table 1. Calculated interface charge trap levels and fixed charges of the as-deposited SiN<sub>x</sub> films.

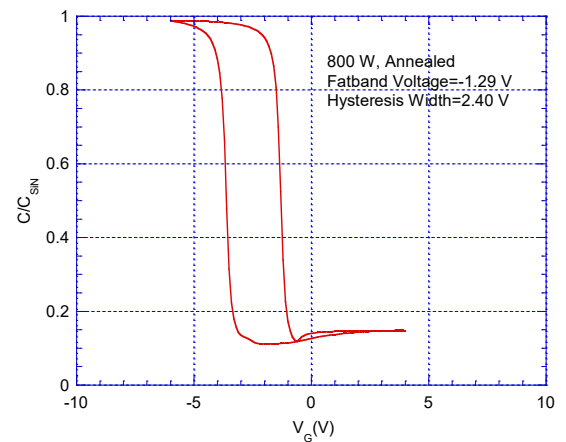
RF Power (W)	Interface States at mid-gap (cm <sup>-2</sup> eV <sup>-1</sup> )	Fixed Charges* (cm <sup>-2</sup> )
500	3.47 × 10 <sup>11</sup>	1.21 × 10 <sup>12</sup>
800	8.80 × 10 <sup>11</sup>	1.33 × 10 <sup>12</sup>
1000	4.52 × 10 <sup>11</sup>	1.06 × 10 <sup>12</sup>

\* Fixed charges include the charged interface states.

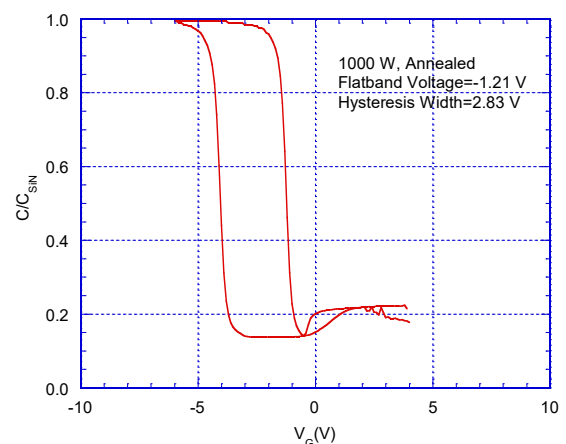
Figure 9 shows the measured C-V curves of the same silicon nitride films used for the measurements of Figure 8, but which were annealed. Compared with those in the as-deposited condition, the flatband shifts of all three silicon nitride films in the annealed condition drastically decreased, indicating a significant decrease in the density of fixed charges. All of the C-V curves became much more vertical, implicating a decrease in the density of interface charge trap levels across the silicon's bandgap. The capacitance of the 1000 W silicon nitride now can readily reach the saturation value at accumulation, representing a low density of interface charge trap levels near the edge of the silicon bandgap. The silicon nitride film made at 500 W made it difficult to reach the saturated capacitance at accumulation. There were also significant changes in the hysteresis shape and width of these C-V curves. The asymmetrical hysteresis of the 800 W C-V curve became symmetrical. The hysteresis widths of the annealed 800 W and 1000 W silicon nitrides decreased to nearly half of those values in the as-deposited condition. However, the hysteresis width of the annealed 500 W film increased significantly.



(a) 500W



(b) 800W



(c) 1000W

Figure 9. C-V curves of the annealed low-temperature silicon nitride films produced at the different microwave powers.

Table 2 shows the calculated results of the annealed silicon nitride films. By comparing these values with those from Table 1, the densities of both the interface charge trap levels and the fixed charges can be seen to decrease significantly. The densities of the interface charge trap levels and the fixed charges of the 800W and 1000W silicon nitride films reached levels acceptable for practical applications in semiconductor devices.

Table 2. Calculated interface charge trap levels and fixed charges of the annealed SiN<sub>x</sub> films.

RF Power (W)	Interface States at mid-gap (cm <sup>-2</sup> eV <sup>-1</sup> )	Fixed Charges* (cm <sup>-2</sup> )
500	1.63 × 10 <sup>11</sup>	1.74 × 10 <sup>11</sup>
800	2.60 × 10 <sup>10</sup>	8.13 × 10 <sup>9</sup>
1000	3.26 × 10 <sup>10</sup>	6.80 × 10 <sup>9</sup>

\* Fixed charges include the charged interface states.

## Discussion

The annealing treatment has a profound influence on the density and property of interface charge traps in the low-temperature silicon nitride films. The density of interface charge traps decreased significantly. The kinetics of charge capture/release became more symmetrical. The density of sluggish interface charge traps increased or decreased, depending on the microwave power conditions used for deposition. Like the silicon nitrides of all of the other thermal, chemical, and physical deposited approaches, the low-silicon nitride films by IC-PECVD incorporated hydrogen atoms in the form of N-H and Si-H bonds. It is known that N-H and Si-H bonds in silicon nitride play a role in determining the density of interface charge traps in silicon nitride films. An amphoteric behavior for N-H and Si-H centers in silicon nitride has been suggested. The charge-trapping role of these amphoteric bonds could be giving rise to the large stretch-out and hysteresis of the C-V curves observed in the low-temperature silicon nitride films.

FTIR analyses revealed that the N-H and Si-H bonds were not stable in the annealing treatment. After annealing, the concentrations of both N-H and Si-H bonds decreased and, at the same time, a small concentration of Si-O bonds were formed. Although the chemical mechanism by which interface charge traps are deactivated and annihilated during annealing is unknown, it is believed that the change in the density and property of interface charge traps is related to the change in the concentrations of both N-H and Si-H bonds and the formation of Si-O bonds. The density of fixed charges in the low-temperature silicon nitride films also decreased significantly after annealing. Fixed charges were generally related to unsaturated dangling Si bonds. The unsaturated dangling bonds usually occurred at the interface,

due to the sudden structure termination of silicon nitride and silicon crystals, which also appeared inside the silicon nitride films as a result of structure imperfections occurring during deposition. Similar to the interface charge traps, the exact mechanism that causes a decrease in the density of fixed charges during annealing was not identified. It is generally believed that hydrogen plays an important role in passivating the unsaturated dangling Si bonds. The migration of hydrogen atoms during annealing is supported by the FTIR results. Also, based on the FTIR analyses, the decrease in the density of fixed charges after annealing may be related to the oxidation reaction during annealing. The oxidation reaction was presumed to have saturated and neutralized the dangling bonds.

Among the low-temperature silicon nitride films made under the three microwave power conditions, the 800W film possessed the best combination of chemical, physical, and electrical properties. The optimal electrical properties of a dielectric layer for most high-performance, modern integrated circuits are a leakage current of ~10<sup>-6</sup> A/cm<sup>2</sup> at 2MV/cm, a breakdown strength from 6 to 10 MV/cm, an oxide fixed charge density in the low 10<sup>10</sup> cm<sup>-2</sup> range, and an interface charge trap level density near mid-gap in the low 10<sup>10</sup> cm<sup>-2</sup> eV<sup>-1</sup> range. Hence, the annealed 800W SiN<sub>x</sub> film in this study was adequate for practical integrated circuits in terms of resistance, leakage current, breakdown strength, and the densities of fixed charges and interface charge traps.

## Conclusions

The annealing treatment has limited influences on breakdown strength, leakage current, and resistivity but significantly decreased the densities of fixed charges and interface states in all of the SiN<sub>x</sub> films made under the three power conditions. After the annealing treatment, the concentrations of both N-H and Si-H bonds decreased and, at the same time, a small concentration of Si-O bonds was formed. It is believed that the significant decreases in the densities of interface charge traps and fixed charges were related to the change in the concentrations of both N-H and Si-H bonds and the formation of Si-O bonds. Overall, the 800W silicon nitride film in the annealed condition possessed the best combination of the chemical, physical, and electrical properties and is satisfactory for practical device applications.

## Acknowledgments

The author would like to thank Morehead State University for its support in funding this research project with a creative production grant and the NSF MRI fund.

## References

- Andringa, A.-M., Perrotta A., de Peuter, K., Knoops, H. C. M., Kessels, W. M. M., & Creatore, M. (2015). Low-

- Temperature Plasma-Assisted Atomic Layer Deposition of Silicon Nitride Moisture Penetration Barrier Layers. *ACS Applied Materials & Interfaces*, 7(40), 22525-22532.
- Bae, S., Farber, D. G., & Fonash, S. J. (2000). Characteristics of Low-Temperature Silicon Nitride (SiN<sub>x</sub>:H) Using Electron Cyclotron Resonance Plasma. *Solid-State Electronics*, 44, 1355-1360.
- Cen, Z. H., Chen, T. P., Ding, L., Liu, Y., Wong, J. I., Yang, M. ...Fung, S. (2009). Strong violet and green-yellow electroluminescence from silicon nitride thin films multiply implanted with Si ions. *Applied Physics Letters*, 94(4), 041102-041102.3.
- Delmotte, F., Hugon, M. C., Agius, B., & Courant, J. L. (1997). Low Temperature Deposition of SiN<sub>x</sub>:H Using SiH<sub>4</sub>-N<sub>2</sub> or SiH<sub>4</sub>-NH<sub>3</sub> Distributed Electron Cyclotron Resonance Microwave Plasma. *Journal of Vacuum Science & Technology*, 15(6), 1919-1926.
- Flewitt, A. J., Dyson, A. P., Robertson, J., & Milne, W. I. (2001). Low Temperature Growth Of Silicon Nitride By Electron Cyclotron Resonance Plasma Enhanced Chemical Vapour Deposition. *Thin Solid Films*, 383, 172-177.
- García, S., Martín, J. M., Martil, I., Fernandez, M., & Gonzalez-Diaz, G. (1998). Deposition of Low Temperature Si-Based Insulators by the Electron Cyclotron Resonance Plasma Method. *Thin Solid Films*, 317, 116-119.
- Hekmatshoara, B., Cherenack, K. H., Kattamis, A. Z., K. Wagner, L., S., & Stum, J. C. (2008). Highly stable amorphous-silicon thin-film transistors on clear plastic. *Applied Physics Letters*, 93, 032103-032105.3.
- Heya, A., Niki, T., Takano, M., Yonezawa, Y., Minamikawa, T., Muroi, S. ...Matsumura, H. (2004). Effect of Atomic Hydrogen on Preparation of Highly Moisture-Resistive SiN<sub>x</sub> Films at Low Substrate Temperatures. *Japanese Journal of Applied Physics*, 43(12A), L1546-L1548.
- Huang, W., Wang, X., Sheng, M., Xu, L., Stubhan, F., Luo, L. ...Zou, S. (2003). Low Temperature PECVD SiN<sub>x</sub> Films Applied in OLED Packaging. *Materials Science and Engineering*, B98, 248-254.
- Hugon, M. C., Delmotte, F., Agius, B., & Courant, J. L. (1997). Electrical Properties of Metal-Insulator-Semiconductor Structures with Silicon Nitride Dielectrics Deposited by Low Temperature Plasma Enhanced Chemical Vapor Deposition Distributed Electron Cyclotron Resonance. *Journal of Vacuum Science & Technology*, 15(6), 3143-3153.
- Isai, G. I., Holleman, J., Wallinga, H., & Woerlee, P. H. (2004). Low Hydrogen Content Silicon Nitride Films Deposited at Room Temperature with an ECR Plasma Source. *Journal of the Electrochemical Society*, 151(10), C649-C654.
- Jin, Z., Neumann, S., Prost, W., & Tegude, F.-J. (2005). Passivation of InP/GaAsSb/InP Double Heterostructure Bipolar Transistors with Ultra-Thin Base Layer by Low-Temperature Deposited SiN<sub>x</sub>. *Solid-State Electronics*, 49, 409-412.
- Jin, Z., Prost, W., Neumann, S., & Tegude, F.-J. (2004). Comparison of the Passivation Effects on Self- And Non-Self-Aligned InP/InGaAs/InP Double Heterostructure Bipolar Transistors by Low-Temperature Deposited SiN<sub>x</sub>. *Journal of Applied Physics*, 96(1), 777-783.
- Lee, J. W., Mackenzie, K., Johnson, D., Shul, R. J., Pearton, S. J., & Ren, F. (1998). Low Temperature ECR-CVD of SiN<sub>x</sub> for III-V Device Passivation. *Solid-State Electronics*, 42(6), 1031-1034.
- Lee, J. W., Mackenzie, K., Johnson, D. D., Shul, R. J., Pearton, S. J., Abernathy, C. R., & Ren, F. (1998). Device Degradation during Low Temperature ECR-CVD. Part II: GaAs/AlGaAs HBTs. *Solid-State Electronics*, 42(6), 1021-1025.
- Lee, J. W., Mackenzie, K., Johnson, D. D., Shul, R. J., Pearton, S. J., Abernathy, C. R., & Ren, F. (1998). Device Degradation during Low Temperature ECR-CVD. Part III: GaAs/InGaP HEMTs. *Solid-State Electronics*, 42(6), 1027-1030.
- Li, F. M., Nathan, A., Wu, Y., & Ong, B. S. (2007). Organic thin-film transistor integration using silicon nitride gate dielectric. *Applied Physics Letters*, 90(13), 133514-133516-3.
- Muller, R. S., & Kamins, T. I. (1986). *Device Electronics for Integrated Circuits* (2nd ed.). Wiley, New York.
- Nicollian, E. H., & Brews, J. R. (1982). *MOS (Metal Oxide Semiconductor) Physics and Technology*. Wiley, New York.
- Nyaupane, P., Bodas, D., Dutta Gupta, S. P., & Gangal, S. A. (2011). Deposition and characterization of low temperature silicon nitride films deposited by ICP-CVD. *Applied Surface Science*, 257, 5052-5058.
- Parka, K. J., & Parsons, G. N. (2004). Bulk and interface charge in low temperature silicon nitride for thin film transistors on plastic substrates. *Journal of Vacuum Science & Technology A: Vacuum Surfaces and Films*, 22(6), 2256-2260.
- Pool, F. S. (1997). Nitrogen Plasma Instabilities and the Growth of Silicon Nitride by Electron Cyclotron Resonance Microwave Plasma CVD. *Journal of Applied Physics*, 81(6), 839-2846.
- Sazonov, A., Striakhilev, D., Lee, C-H., & Nathan, A. (2005). Low-Temperature Materials and Thin Film Transistors for Flexible Electronics. *Proceedings of the IEEE*, 93(8), 1420-1428.
- Shao, Z., Chen, Y., Chen, H., Zhang, Y., Zhang, F., Jian, J. ...Yu, S. (2016). Ultra-low temperature silicon nitride photonic integration platform. *Optics Express*, 24(3), 1865-1872.
- Stryahilev, D., Sazonov, A., & Nathan, A. (2002). Amorphous nitride deposited at 120°C for organic light emitting display-thin film transistor arrays on plastic substrates. *Journal of Vacuum Science & Technology A Vacuum Surfaces and Films*, 20(3), 1087-1090.
- Suzuki, N., Cervera, R. B., Ohnishi, T., & Takada, K. (2013). Silicon nitride thin film electrode for lithium-ion batteries. *Journal of Power Sources*, 231(1), 186-189.

- 
- Sze, S. M. (1981). *Physics of Semiconductor Devices* (2nd ed.). Wiley, New York.
- Takano, M., Niki, T., Heya, A., Osono, T., Yonezawa, Y., Minamikawa, T. ...Matsumura, H. (2005). Preparation of Low-Stress SiN<sub>x</sub> Films by Catalytic Chemical Vapor Deposition at Low Temperatures. *Japanese Journal of Applied Physics*, 44(6A), 4098-4102.
- Xu, Q., Ra, Y., Bachman, M., & Li, G. P. (2009). Characterization of low-temperature silicon nitride films produced by ICP-CVD. *Journal of Vacuum Science Technology*, 27(1), 145-156.
- Zambona, L., & Mansano, R. D. (2003). Silicon Nitride Deposited By Inductively Coupled Plasma Using Dichlorosilane and Ammonia. *Vacuum*, 71, 439-444.

## Biographies

**Qingzhou Xu** received his bachelor's degree in materials science and engineering from Harbin Institute of Technology in China in 1989. He earned a master's degree in materials science and engineering from Beijing University of Science and Technology in 1992, and his PhD in materials science and engineering from the University of California Irvine in 2000. He has worked as an engineer in the Chinese Academy of Science Mechanics Institute and the Chinese National Engineering Center of Composites, both in Beijing, China, and the RF Integrated Corporation in California. His early study and work experience includes structural materials (light alloys and refractory metals), engineering functional materials (hard/soft magnetic materials, hydrogen-storage materials for rechargeable battery and non-lead soldering materials), and thin films. His recent study and work experience are mainly on semiconductor materials and processing, III-V compound device passivation, high-speed transistor (HBTs and HEMTs) processing and characterization, micro-electro-mechanical systems (MEMS), magnetostatic actuators and electrostatic switches, nanolithography, and nano-devices. His current interests focus on using materials science knowledge to solve reliability issues in the areas of RF MEMS switches (thin-film stress control, reliable switch contacts, and novel switch architecture with enhanced reliability), and III-V compound transistors (high-performance ohmic contacts and device passivation) as well as developing novel nano-layered and nanostructured materials. He has authored more than 30 journal and conference papers. Dr. Xu may be reached at [q.xu@moreheadstate.edu](mailto:q.xu@moreheadstate.edu)

# PERFORMANCE-BASED DESIGN OF DIAGRID TALL BUILDINGS FOR EARTHQUAKE LOADS

Mohammad T. Bhuiyan, West Virginia State University; Md. Arifuzzaman, King Faisal University; Ayed Alluqmani, Islamic University of Madinah

## Abstract

A triangulated exoskeleton, or diagrid, structural system has emerged as a structurally efficient and architecturally valid solution for tall buildings. The diagrid creates an efficient and redundant tube structure by providing a structural network allowing multiple load paths. The diagrid system has higher inherent torsional rigidity than most other structural systems. Although engineers recently started using this structural system for tall buildings, almost all related applications have been in areas of low seismicity. The main goal of this current study was to examine the potential utilization of this efficient and economic structural system in tall buildings in high-seismic regions. Three buildings with different heights (82-story, 64-story, and 38-story) and footprints were selected. Detailed performance-based assessments were carried out for earthquake action at various hazard levels for serviceability, survivability, and collapse prevention. The results from the analyses showed a superior performance for the diagrid structures under seismic loading.

## Introduction

The diagrid, in a diagrid structure, creates an efficient and redundant tube structure by providing a structural network allowing multiple load paths. The diagrid forms an exterior tube that can maximize the moment arm to resist overturning. Furthermore, the diagrid system has higher inherent torsional rigidity than most other structural systems. Most importantly, it is estimated that a diagrid structural solution may provide about a 25% reduction in structural costs compared to a frame tube structure (Rahimian & Eilon, 2008; Baker, 2006). The working principle of the diagrid system is to convert global building moments, shears, and torsional forces into “axial action” in order to diagonally brace elements.

The structural design of a tall building involves several stages, including the conceptual design, approximate analysis, preliminary design and optimization, followed by detailed and final designs. The main design criteria are strength, serviceability, and human comfort. The aim of the structural engineer is to arrive at suitable structural schemes to satisfy these criteria and assess their relative economy. The main goal for this current study was to examine the potential utilization of this efficient and economic structural system to tall buildings in high-seismic regions using a performance-based design (PBD) methodology.

## Performance Objective for Earthquakes

Tall buildings located in moderate and high-seismic regions should be designed based on a sound performance-based seismic design methodology. The main reason is that tall buildings possess unique behavioral and/or design characteristics and, thus, structures such as high-rise diagrids cannot be designed based on prescriptive, code-based procedures. Table 1 summarizes the performance objectives and evaluation criteria in each design step.

Table 1. Summary of basic performance objectives.

Design/evaluation step	1	2	3
Description	Minor (frequently occurred)	Check for minimum base shear strength, $V_{min}=0.03W$	Severe (rarely occurred)
Ground motion intensity	50% probability of exceedance in 30 years (43-year return period)		MCE, 2% probability of exceedance in 50 years
Qualitative performance levels	No damage		No collapse
Type of analysis	Linear dynamic procedure		Non-linear dynamic Procedure
Type of mathematical model	3D		3D
Load Combination	$1.0D + L_{exp} + 1.0E$		$1.0D + L_{exp} + 1.0E$
Material reduction factors ( $\phi$ )	1.0		1.0
Material strength	Expected properties		Expected properties
Allowable story drift ratio			0.025h
Global building drift limit	0.005H		
Diagonal brace performance	$DCR < 1.0$		Should not significantly lose strength

The PBD approach used in this study can be summarized into the following steps:

#### Step 1: Service-level design

This was carried out for an event having a 50% probability of exceedance in 30 years (a 43-year return period). The purpose of this design level was to prove that the building's structural systems and non-structural components would be functional after such an event. Repairs, if necessary, were expected to be minor and could be performed without substantially affecting the normal use and functionality of the building. For this level, expected material properties were used in response spectrum (RS) analyses with a load combination of  $1.0D + L_{exp} + 1.0E$ . The DCR of the diagonal braces should be less than 1.0 for the RS analysis. Under these conditions, the global building drift should be limited to 0.005H.

#### Step 2: Minimum base shear strength

For this study,  $V_{min} = 0.03W$  was used. This may be satisfied by performing elastic response spectrum analyses where the design spectrum values were scaled to produce a complete quadratic combination (CQC) base shear equal to or larger than  $0.03W$ .

#### Step 3: Collapse prevention

This was carried out for an event having a 2% probability of exceedance in 50 years (a 2475-year return period). This earthquake is the maximum considered earthquake (MCE). Expected material properties were used in non-linear time-history (NLTH) analyses with a load combination of  $1.0D + L_{exp} + 1.0E$ . The peak story drift limit was taken as 0.025 (2.5%) for any story. Also, locations of nonlinear behavior were allowed but limited to the diagonal braces. Diagonal deformation demands were carefully checked to ensure that they did not exceed limits provided by local buckling in compression and a fraction of the maximum elongation in tension. All building core and floor elements were limited to elastic behavior.

## Case Study Buildings

Three diagrid structures (64-story, 82-story, and 38-story) with different footprints and heights were selected for this study. All of the buildings were located in a suburb of Los Angeles, California. This is a zone of high seismic ground motions and moderate wind velocities (135 kph or 85 mph). Figure 1(a) shows a 3D view of the 64-story diagrid structure. The overall plan dimensions of the building were 52m x 35.5m (172 ft. x 115 ft.), with a building height of 224m (735 ft.). It should be noted that gravity columns were located only around the core of the building and there were no vertical columns (either gravity columns or lateral force-resisting columns) outside the building core. The wind and earthquake resisting system was composed of a network of diagonal elements around the building perimeter, forming a triangulated pattern to create an efficient tube structure. As the lateral system was composed of diagonal elements in a

grid pattern, the system was called a "diagrid structural system," or, henceforth, diagrid. The floor framing was a composite system, where 75mm (3") concrete topping was used over 75mm-deep (3") steel deck supported by open-web steel joists.

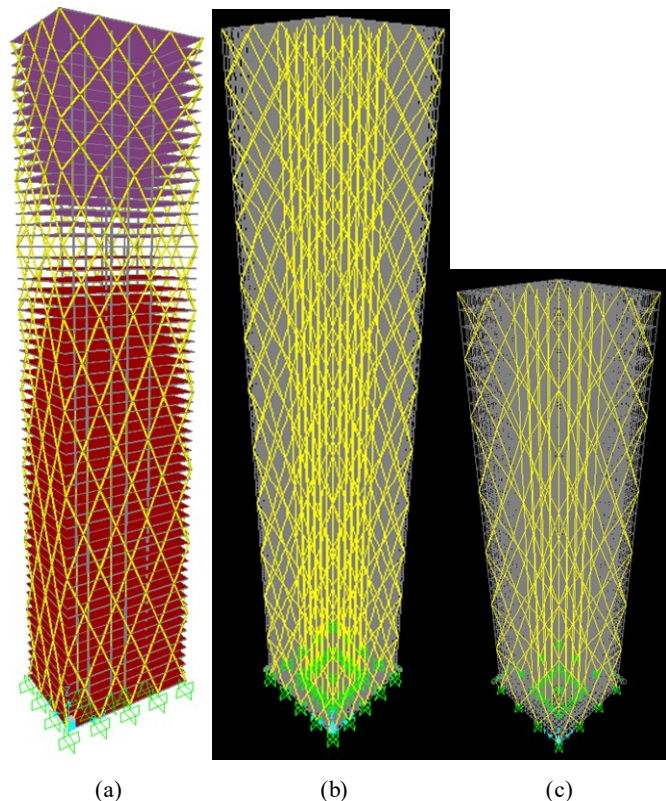


Figure 1. 3-D view of : (a) 64-story (b) 84-story and (c) 38-story diagrid structures.

The second building was 82 stories. The overall plan dimensions of the building were 48m x 48m (157 ft. x 157 ft.), with a building height of 287m (942 ft.). Figure 1(b) shows a 3D view of the diagrid structure. The floor framing was a composite system similar to the 64-story building. Similar to the first two buildings, the third building was a 38-story building for which the overall plan dimensions were 33m x 33m (108 ft. x 108 ft.), with a height of 133m (436 ft.). Figure 1(c) shows a 3D view of the structure. A more detailed description and preliminary design of these diagrid structures can be found in a study by Bhuiyan and Leon (Bhuiyan & Leon, 2018).

## Seismic Loading

As PBD was used for this study, three response spectra were used. These corresponded to three hazard levels: (i) 50% probability of exceedance in 30 years; (ii) 10% probability of exceedance in 50 years; and, (iii) 2% probability of exceedance in 50 years.

Performance-based design requires a 3D non-linear time history analysis using ground motion time histories. Seven spectrum-compatible, three-component ground motions used in this study were provided by Dr. Tony Yang, Prof. Stephen Mahin, & Dr. Yousef Bozorgnia via email on August 3, 2009. The same spectrum and spectrum-compatible ground motions were used by the PEER tall building initiative for analyzing a number of tall concrete buildings. Spectrum compatibility was achieved through frequency domain modification on recorded acceleration time histories. The recorded ground motions were obtained from a PEER NGA ground motion database. Table 2 provides the information of the original ground motions.

Table 2. Information of seven ground motions used to perform non-linear time history analyses.

Record number	NGA record sequence number	Earthquake name	Year	Station name
Set 1	723	Superstition Hills-02	1987	Parachute test site
Set 2	2113	Denali, Alaska	2002	TAPS pump station #09
Set 3	1084	Northridge-01	1994	Sylmar - converter station
Set 4	802	Loma Prieta	1989	Saratoga - Aloha Ave
Set 5	1086	Northridge-01	1994	Sylmar - Olive view med FF
Set 6	900	Landers	1992	Yermo fire station
Set 7	1165	Kocaeli, Turkey	1999	Izmit

Figure 2 shows acceleration time histories of the seven ground motions. Figure 3 depicts the response spectrum used in this study, whereas Figure 4 depicts the spectral compatibility of the ground motions to the MCE target spectrum. Figure 4 also shows that the individual spectrum matches were well with the target spectrum. Other characteristics of these ground motions can be found in a previous study by Bhuiyan (Bhuiyan, 2011).

## Modeling Procedures

Several software platforms were utilized, and many models were built for this study. The three main platforms were: (i) SAP2000 – a general purpose structural engineering software mostly used for elastic analysis (Computers, 1997); (ii) Perform 3D – performance-based design in general and performance assessment of high-rise building design in seismic regions were frequently conducted using Perform 3D

(Computers, 2006); and, (iii) OpenSEES – a sophisticated open source program for nonlinear time-history analysis. Due to its lack of pre- and post-processing tools, it is mostly used by researchers (Pacific, 2008). Elastic 3D building models were used for modal analysis, service-level evaluation, and minimum base shear strength. These analyses were conducted using SAP2000. The Perform 3D software platform was used for response spectrum analyses for seismic service-level evaluations. Detailed 3D nonlinear models of the building, constructed in OpenSEES, were used for all seismic time-history analyses.

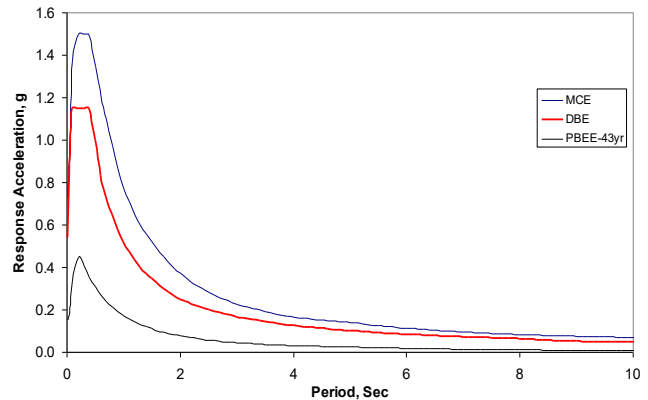


Figure 3. Response spectrum used in this study.

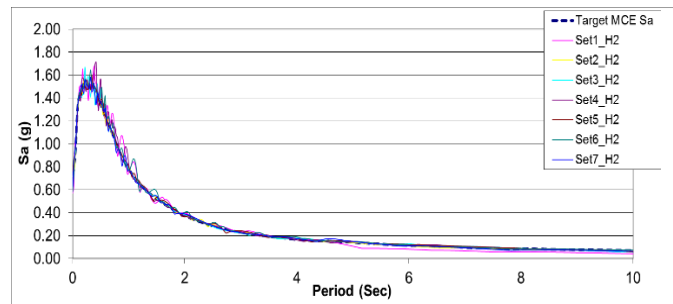
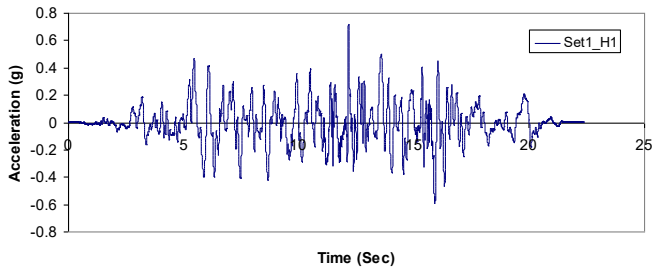


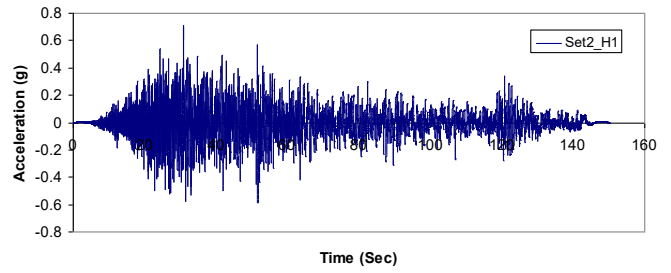
Figure 4. Spectrum compatibility of the ground motions at MCE level.

Total Dead Load = 81 psf  
 concrete = 55 psf  
 reinforcing steel = 2 psf  
 steel deck = 2.14 psf  
 joist = 4.5 psf  
 mechanical = 8 psf  
 electrical = 4 psf  
 fireproofing = 2 psf  
 floor covering & ceiling = 3 psf

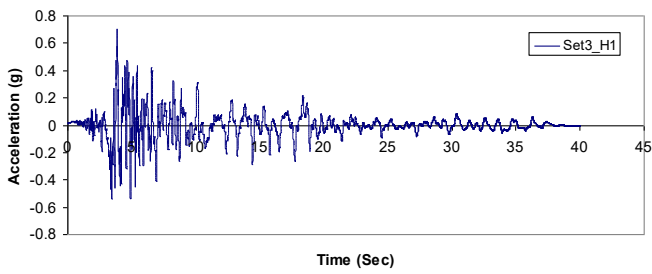
Total Live Load (outside the core) = 95 psf  
 Total Live Load (inside the core) = 65 psf  
 design LL inside the core = 80 psf  
 outside the core = 50 psf  
 partition load = 15 psf



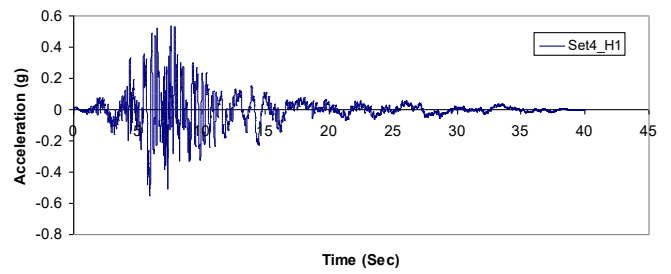
(a) Superstition Hills-02 earthquake



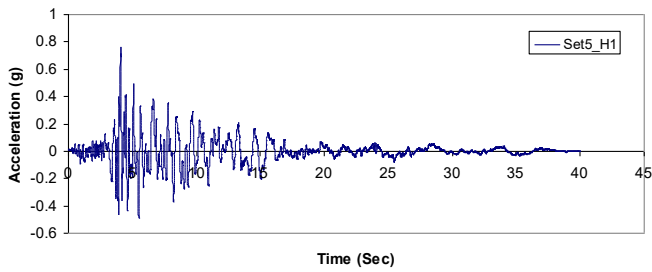
(b) Denali, Alaska, earthquake



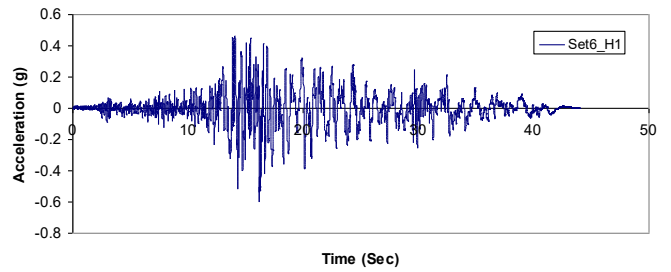
(c) Northridge-01 (1084) earthquake



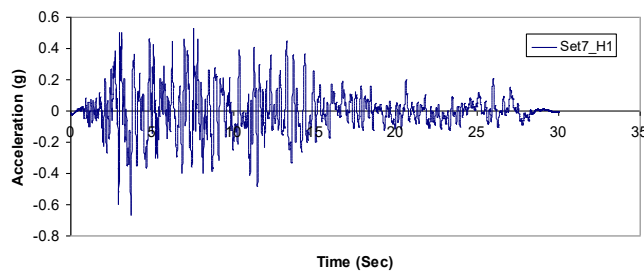
(d) Loma Prieta earthquake



(e) Northridge-01(1086) earthquake



(f) Landers earthquake



(g) Kocaeli, Turkey, earthquake

Figure 2. (a) to (g) - Seven acceleration time histories used for non-linear time history analyses.

Common modeling features and assumptions used in the SAP2000, Perform 3D, and OpenSEES models were: (i) a center-line model was established based on the idea that diagonal braces would mostly have axial forces and, therefore, panel-shear deformation would not play an important role—even if there were some panel shear deformation, the use of a centerline length offset this contribution; (ii) the connections between diagonal braces were considered as rigid; (iii) the foundation was modeled as rigid; (iv) the floor was modeled as a rigid diaphragm for all floors; (v) the mass for dynamic analysis was taken as total dead load + 25% of live load; (vi) lumped masses were assumed at nodal points of all gravity column nodes and all diagonal brace nodes of each floor; (vii) masses for both translational directions were considered at all nodes—local rotational-inertia masses at nodal points were considered to be small and, thus, neglected; (viii) global rotational inertia was automatically taken into account by the distribution of the masses at each node on each floor level; and, (ix) the Rayleigh damping model was used. Following are the distinct modeling features used for each software platform.

#### SAP2000

The “frame elements” of SAP2000 were usually used to model beam-column behavior in planar and three-dimensional structures. Figure 5 shows how a frame element was used to model all of the story’s high braces and gravity columns.

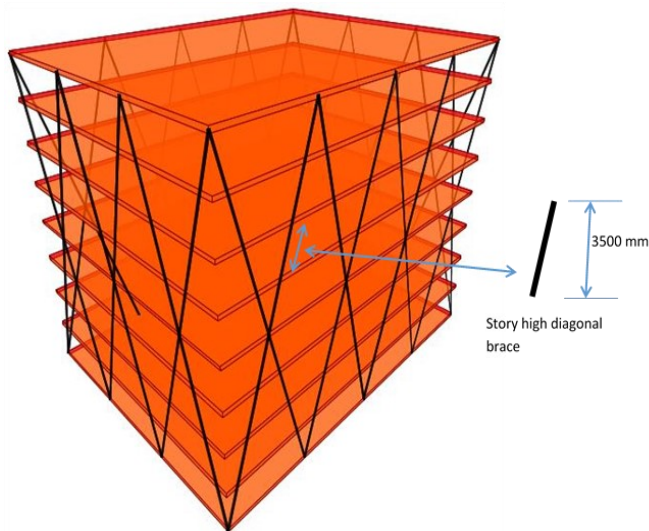


Figure 5. Story-high diagonal brace.

#### Perform 3D

The “column element” was used to construct “frame compound components” in order to model the beam-column behavior of the 3D structure. As only response spectrum analyses were performed, an elastic model of the 3D structure was sufficient, and it was quite simple to define these frame compound components for all of the story’s high braces (see again Figure 5).

#### OpenSEES

Figure 6(a) shows how each story-high diagonal brace element from Figure 5 was modeled using two force-based fiber elements (Spacone, Ciangi, & Filippou, 1992) with an initial imperfection of  $L/750$ , where  $L$  is the length of the story-high brace. Figure 6(b) shows that each force-based fiber element had five integration points, while Figure 6(c) shows that at each integration point the pipe section was discretized into 160 fibers.

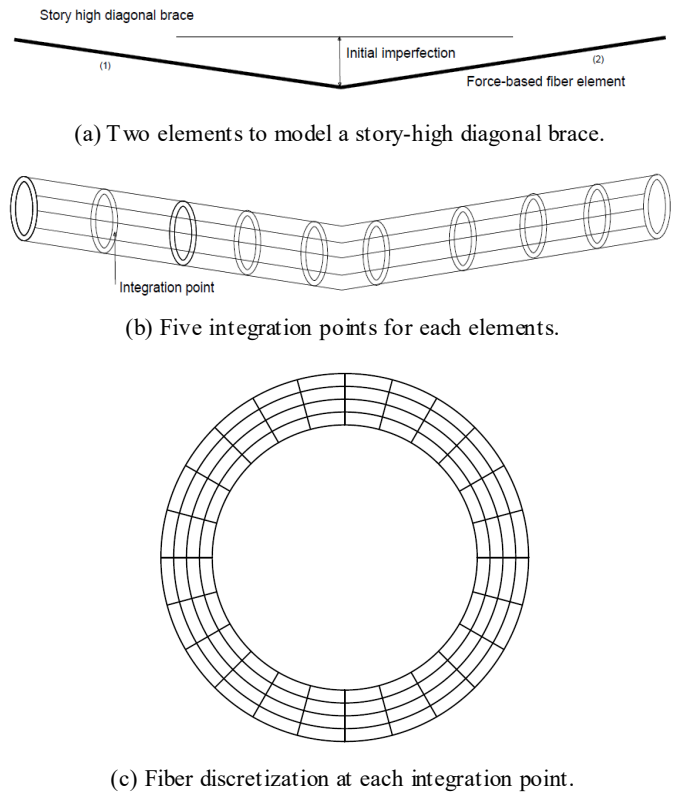


Figure 6. Modeling technique of a story-high diagonal brace element with two force-based fiber elements (a) with initial imperfection, each element has five integration points (b), and at each integration point pipe section is discretized to 160 fibers (c).

## Results of the 64-Story Building

The aim of this evaluation was to prove that the building’s structural systems and its nonstructural components were functional after such an event with a 43-year return period. Figure 3 shows the response spectrum analyses that were carried out using PERFORM-3D and the PBEE-43-year response spectrum. A Rayleigh damping ratio of 1% was used for the elastic 3D model of the building. Results of the analysis were taken from the first twenty modes. The displacements of the building at the roof level were found to be 278 mm and 210 mm in the Z- and X-directions, respectively. These values were well below the limit of 0.005H (1120mm). Figure 7 shows a plot of inter-story drift angle.

The maximum inter-story drift was found to be around 0.2%, which was low enough to ensure that damage to non-structural elements would not occur, or at least be in the insignificant range.

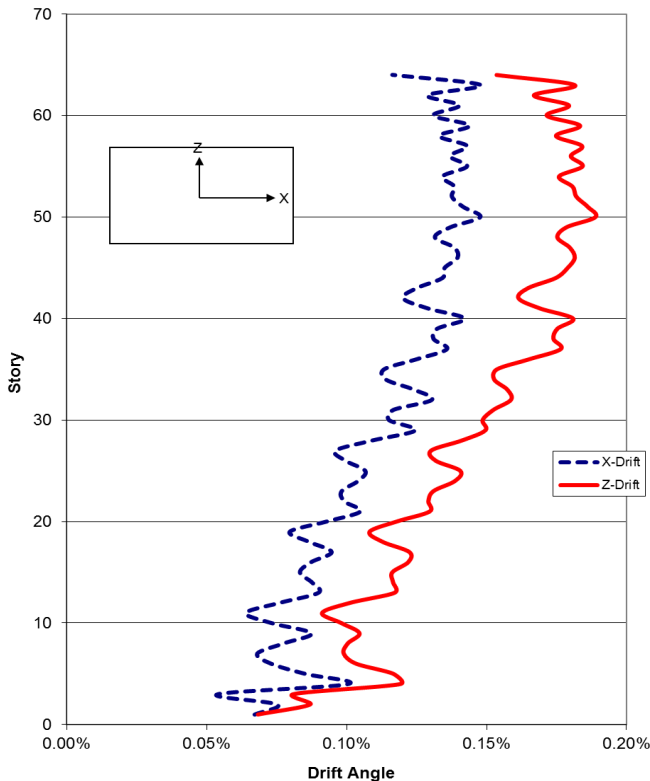


Figure 7. Inter-story drift angle for serviceability level earthquake (max value around 0.2%).

Regarding the response of individual structural members, the demand-capacity ratios (DCRs) for all of the diagonal braces and all of the gravity columns were found to be well below 1.0. Thus, it would appear that the 64-story building, as required by PBD, would behave in the elastic range for the service load earthquake. As the building was governed by stiffness, the DCRs for this level of design were relatively low. Following are the findings for minimum base shear strength and life-safety checks.

#### Outside the core of the building:

$$DL+25\%LL = (81 + 0.25*65) \text{ psf} = 97.25 \text{ psf} = 4.656 \text{ kN/m}^2$$

$$\text{Area} = 0.75 * (52.5 \text{ m} * 35 \text{ m}) = 1378.125 \text{ m}^2$$

#### Inside the core of the building:

$$DL+25\%LL = (81 + 0.25*95) \text{ psf} = 104.75 \text{ psf} = 5.015 \text{ kN/m}^2$$

$$\text{Area} = 0.25 * (52.5 \text{ m} * 35 \text{ m}) = 459.375 \text{ m}^2$$

$$DL + 25\% \text{ of } LL = 4.656*1378.125 + 5.015*459.375 = 8720 \text{ kN/}$$

floor

For the entire building, as there were 64 floors:

$$DL + 25\% \text{ of } LL = 8720 * 64 = 558,080 \text{ kN}$$

Adding the self-weight of the columns and braces (69,376 kN), the seismic weight of the building considering full dead load plus 25% live load was  $558,080 + 69,376 = 627,456 \text{ kN}$ . Thus, the minimum base shear of  $0.03W$  was  $0.03 * 627,456 = 18,823 \text{ kN}$  ( $1.88 \times 10^7 \text{ N}$ ) for both directions of loading. In the Z-direction, the base shear strength requirement for wind was  $4 \times 10^7 \text{ N}$ , while the base shear imposed by the service-level earthquake was  $2.6 \times 10^7 \text{ N}$ . As minimum base shear ( $1.88 \times 10^7 \text{ N}$ ) was less than service-level earthquake strength ( $2.6 \times 10^7 \text{ N}$ ); therefore, it satisfied the objective in Table 1. Figure 3 further shows that the design basis earthquake (DBE) demand with a response modification factor of  $R=5.0$  was less than the demand imposed by the service-level earthquake (PBEE-43-year return period). Figure 10 shows that demand imposed by wind was larger than the demand imposed by a life-safety-level earthquake (475-year return period). It should be noted that the size of the diagonal braces was not controlled by strength requirements from wind or earthquake loads, but rather wind-drift requirements (stiffness) to control the size of the diagonal brace.

This is typical of very tall buildings, where wind demands determine the basic stiffness requirements, and the seismic design is primarily focused on providing ductility and robustness. For a typical 50-60 story building located in a high seismic region, the need to limit allowable drift results in a building that is 2.5 to 4 times stiffer than required by seismic demand (Naem & Graves, 2005). Figure 3 also shows that the demand from the service-level earthquake was higher than that of a life-safety earthquake; some would question whether the life-safety evaluation was necessary at all. Figure 8 shows a plot of maximum inter-story drift in the X-direction. In this figure, thin lines represent the drift ratio from each of the seven THAs, whereas the bold line represents the average of the seven curves. As can be seen from the figure, the responses from individual ground motion are close to each other (i.e., the scatter in the response was low by seismic design standards).

Figure 4 graphically explains the reason for this; that is, that for all seven motions, the frequency content was modified to match the target MCE spectrum individually. Figure 8 shows that maximum inter-story drift ranges from about 1% to 1.3%, due to the MCE event. The allowable drift limit (from Table 1) was 2.5%. Thus, the response (in terms of drift) of the 64-story diagrid structure was well within the allowable limit. Deformation, capacity, and strength degradation were monitored for all of the braces. It was found that braces in the bottom stories underwent nonlinearity, while maintaining the full strength of the member without any degradation while most of the upper story braces did not exceed yield limit. Figure 9 shows the maximum story moments, MX. In the figure, thin lines represent the response from each of the seven THAs, whereas the bold line represents the average of the seven curves. Again, the scatter in the response was relatively low, as expected, as the ground motions were spectrally matched.

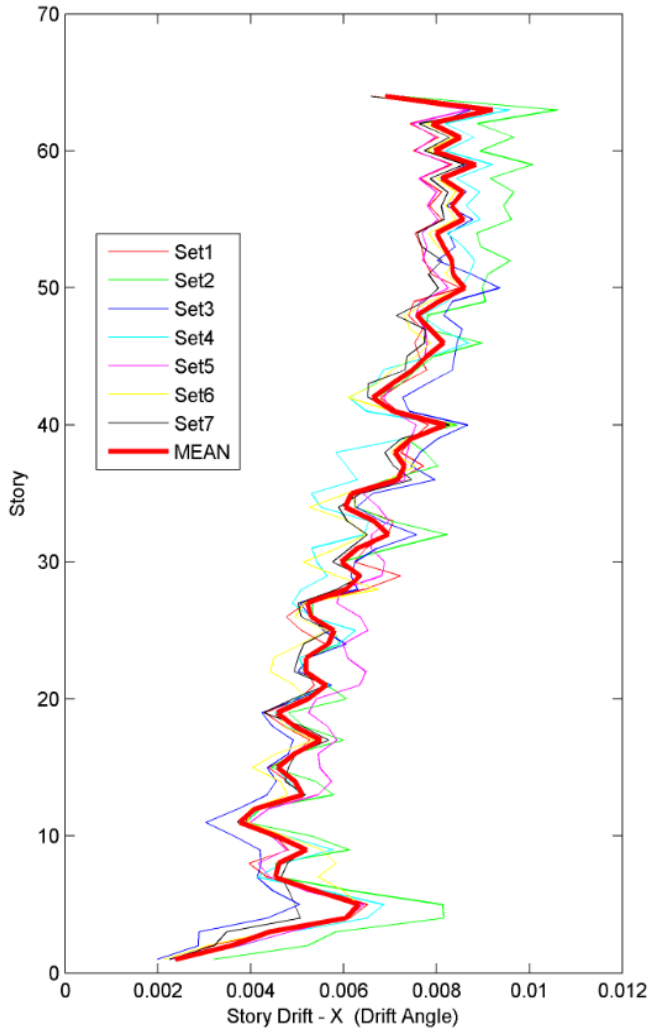


Figure 8. Story drift angle in the X-direction – from THA of the 7 sets of ground motion at the MCE level.

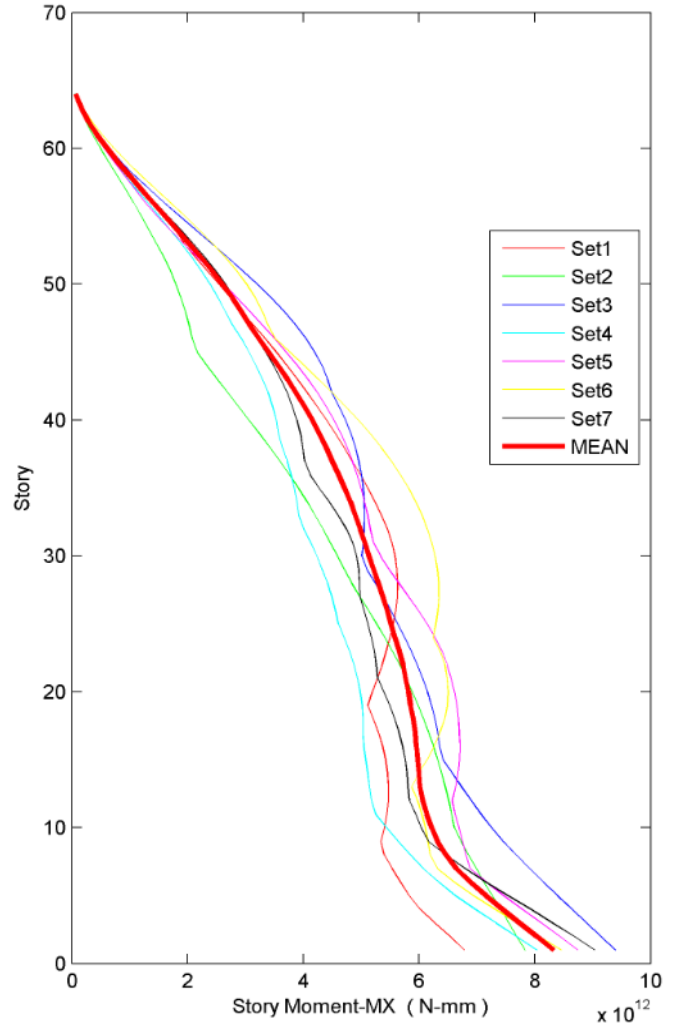


Figure 9. Story moment MX – from THA of the 7 sets of ground motion at the MCE level.

Figure 10 presents a comparison of the demands imposed by the MCE earthquake with those of the wind and DBE-level earthquake. It shows the comparison of responses in terms of story-shear FX. The bold, dark green line represents the average of 7 THAs with the MCE-level ground motion, while the red line represents the response of the building due to wind. The response spectrum analysis for the DBE-level earthquake is shown by a continuous pink line. It is evident from Figure 10 that story shear for wind was much lower than MCE-level earthquake demand. Two points can be made from the figure. First, the lines do not mean that wind did not have any role in the design, as drift limitations and not strength drive wind design. Second, the forces in the key elements shown here will need to be amplified for the design of connection elements and diaphragms that were required to remain elastic. An assessment of the dynamic amplification of these forces cannot be made without NLTHA at the MCE level.

Building codes typically do not mandate that designers perform a THA. The designer can meet the code requirement by performing response-spectrum analyses with the DBE-level spectrum. To compare this approach with NLTHA analyses, a response spectrum analysis was performed with a force reduction factor (R) equal to 5. Figure 10 shows that the response spectrum values were significantly smaller. This clearly shows that designing a tall building based on only a response-spectrum analysis might lead to unsafe designs. It may be argued that wind criteria will make the structure strong enough, if the response spectrum technique were used for seismic design. While it is true that wind criteria will make the structure strong, the design forces for diaphragm ties and chords, connections between floor plate and diagonal braces, and foundation design forces will be significantly lower than those required from a THA. Thus, it is strongly recommended that an NLTHA be performed at the MCE level for design of tall structures.

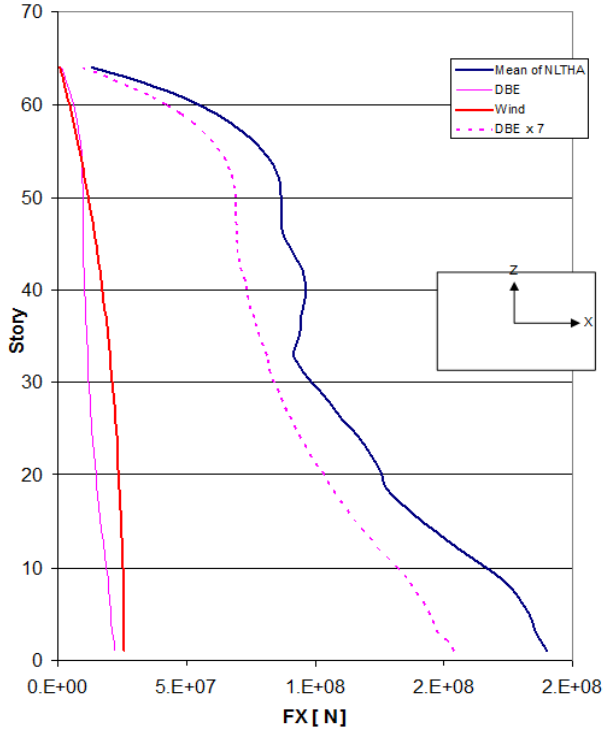


Figure 10. Story shear FX.

## Results of the 82-Story Building

The displacements of the building at the roof level were found to be 290 mm in both the Z- and X-directions. These values were well below the limit of  $0.005H$  (1435mm). Inter-story drift angle was computed for every story. The maximum inter-story drift was found to be around 0.14%, which was low enough to ensure that damage to non-structural elements would not occur or be in the insignificant range. Figure 11 shows the plot of maximum inter-story drift in the X-direction. In this figure, thin lines represent the drift ratio from each of the seven THAs. Figure 11 also shows that maximum inter-story drifts range from about 0.8% to 1.45%, due to the MCE event. The allowable drift limit (from Table 1) is 2.5%. Thus, the response (in terms of drift) of the 82-story diagrid structure were well within the allowable limit. Figure 12 shows the plot of maximum story shears, FX. In this figure, thin lines represent the response from each of the seven THAs. Again, the scatter in the response was relatively low, as expected, as the ground motions were spectrally matched.

## Results of the 38-Story Building

Response spectrum analyses were carried out using SAP2000 and the PBEE-43-year response spectrum (see again Figure 3). A Rayleigh damping ratio of 1% was used for the elastic 3D model of the building. Results of the analyses were taken from the first twenty modes.

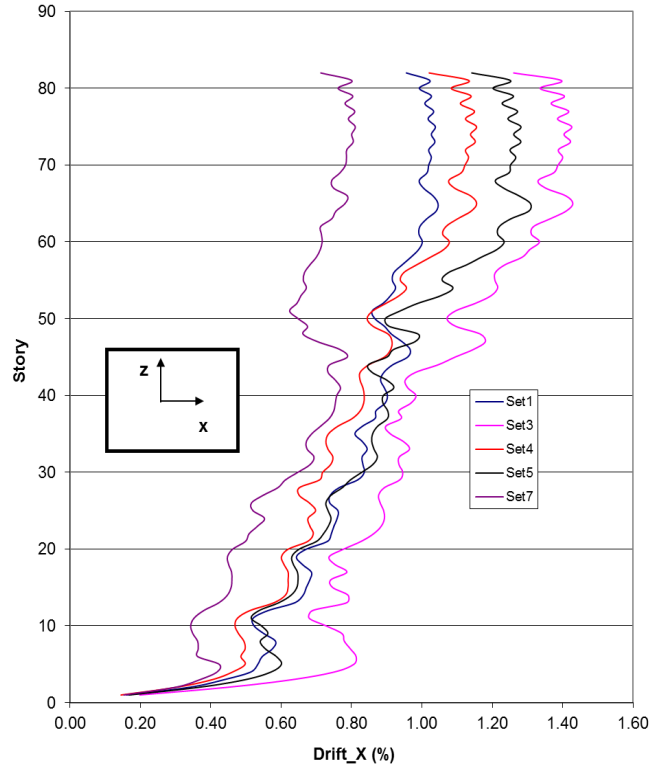


Figure 11. Maximum inter-story drift, X, at MCE for the 82-story building.

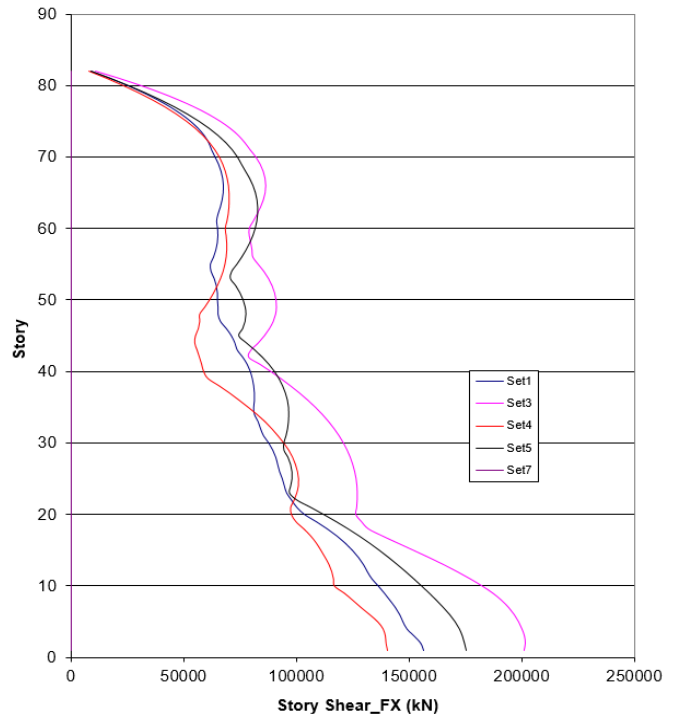


Figure 12. Maximum story shear, FX, at MCE for the 82-story building.

The displacements of the building at the roof level were found to be 184 mm in both the Z- and X-directions. These values were well below the limit of 0.005H (665mm). Inter-story drift angle was computed for every story. The maximum inter-story drift was found to be around 0.19%, which was low enough to ensure that damage to non-structural elements would not occur or at least be in the insignificant range. Nonlinear response history analyses of the building were performed for the maximum considered earthquake shaking using the same spectral compatible motion shown in Figure 2. Figure 13 shows a plot of maximum inter-story drift in the X-direction. In this figure, thin lines represent the drift ratio from each of the seven THAs. Figure 13 also shows that maximum inter-story drifts range from about 0.8% to 1.4%, due to the MCE event. The allowable drift limit (from Table 1) was 2.5%. Thus, the response (in terms of drift) of the 38-story diagrid structure was well within the allowable limit. Figure 14 shows the maximum story moments, MZ. In the figure, thin lines represent the response from each of the seven THAs. Again, the scatter in the response was relatively low, as expected, as the ground motions were spectrally matched.

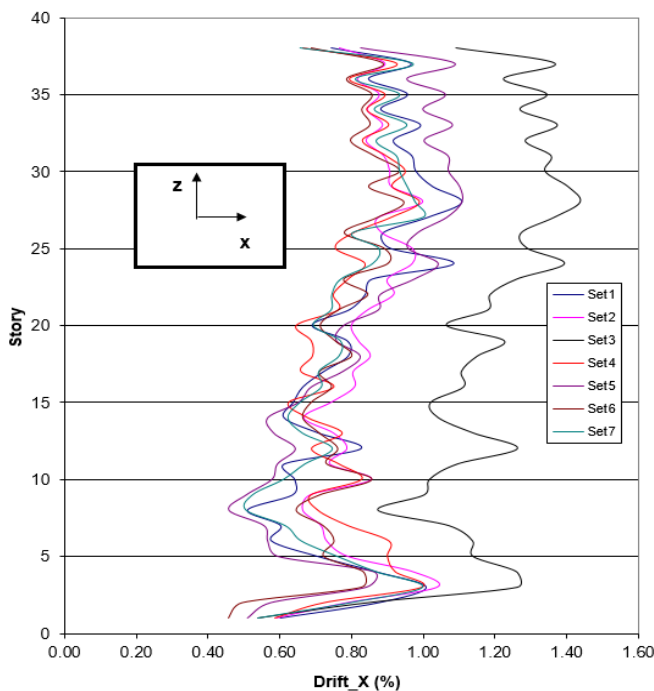


Figure 13. Maximum inter-story drift, X, at MCE for the 38-story building.

## Conclusions

Three diagrid structures (64-story, 82-story, and 38-story) were evaluated based on a performance-based design (PBD) methodology in a high-seismic region. The performance-based design included explicit consideration of serviceability, survivability, and collapse prevention.

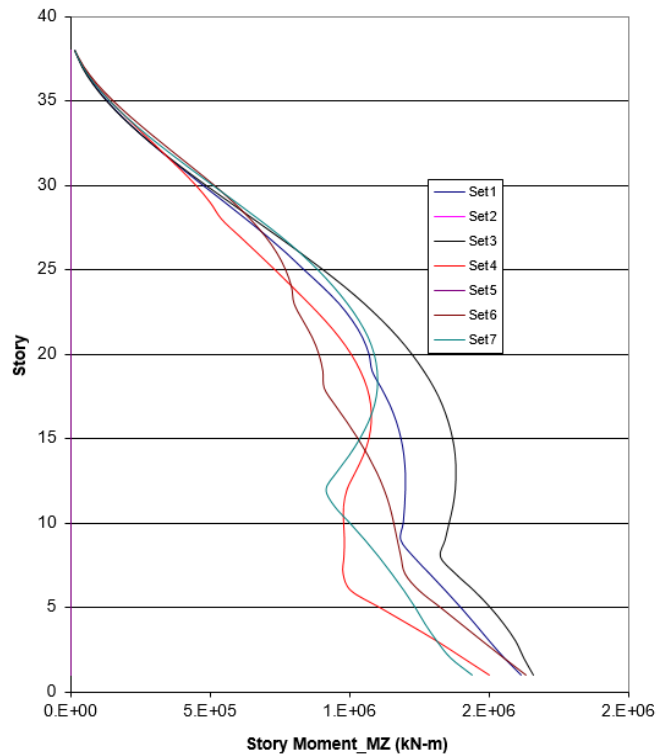


Figure 14. Maximum story moment, MZ, at MCE for the 38-story building.

Checks against the desired performance criteria showed a superior performance for the diagrid structure under seismic loading. Thus, the tall building design community in the high-seismic area can consider the diagrid system as a potential candidate for their client's high-rise buildings. The non-linear time-history analyses indicated very large dynamic amplification of shear and moment demands that need to be taken into account for the design of the diaphragms, chords, connections between floor plate and diagonal braces, foundations, and other structural elements. These amplifications of forces cannot be predicted without careful non-linear analyses at the maximum credible earthquake level. Thus, it is strongly recommended to perform NLTHA for design of tall structures.

## References

- Rahimian, A., & Eilon, Y. (2008). Hearst Headquarters: Innovation and Heritage in Harmony, Paper presented at the Council of Tall Buildings and Urban Habitat, Dubai, UAE, March 3-5.
- Baker, W. (2006). Tapered and Twisted Towers. Paper presented at the Council of Tall Buildings and Urban Habitat, Chicago, Illinois, October 25-26.
- Bhuiyan, M., & Leon, R. (2018). Preliminary Design of a Diagrid Tall Buildings. *International Journal of Modern Engineering*, 18(1), 5-14.

- 
- Bhuiyan, M. (2011). *Response of Diagrid Tall Building to Wind and Earthquake Actions* (Unpublished doctoral dissertation). ROSE School, University of Pavia, Pavia, Italy.
- Computers and Structures, Inc. (1997). SAP2000 – Integrated Structural Analysis & Design Software [Computer software]. Computers and Structures, Inc., Berkeley, California.
- Computers and Structures, Inc. (2006). PERFORM-3D – Nonlinear Analysis and Performance Assessment for 3D Structures [Computer software]. Computers and Structures, Inc., Berkeley, California.
- Pacific Earthquake Engineering Research Center. (2008). Open System for Earthquake Engineering Simulation [Computer software], Pacific Earthquake Engineering Research Center, Berkeley, California.
- Spacone, E., Ciampi, V., & Filippou, F. (1992). *A Beam Element for Seismic Damage Analysis*. Earthquake Engineering Research Center, University of California, Berkeley. Report No. UCB/EERC-92/07.
- Naeim, F., & Graves, R. (2005). The case for seismic superiority of well-engineered tall buildings. *The Structural Design of Tall & Special buildings*, 14, 401-416.
- city, UK. His research interest include concrete and steel structures, earthquake engineering, soil-structure interaction, and solid wastes. Dr. Alluqmani may be reached at [drayed@iu.edu.sa](mailto:drayed@iu.edu.sa)

## Biographies

**MOHAMMAD T. BHUIYAN** is an associate professor of civil engineering at West Virginia State University (WVSU). He earned his BSc in Civil Engineering from Bangladesh University of Engineering and Technology, Dhaka; his MSc in Earthquake Engineering jointly from Universite Joseph Fourier, France, and ROSE School, Italy; and PhD in Earthquake Engineering from ROSE School with a joint program at Georgia Tech. His research interests include tall building, earthquake engineering, and soil-structure interaction. Dr. Bhuiyan may be reached at [towhid@wvstateu.edu](mailto:towhid@wvstateu.edu)

**MD ARIFUZZAMAN** is an assistant professor of civil engineering at King Faisal University (KFU). He earned his BSc in Civil Engineering from Bangladesh University of Engineering and Technology, Dhaka; his MS in Geotechnical and Geo-Environmental Engineering from the Asian Institute of Technology; and PhD in Civil Engineering from the University of New Mexico. His research interest include materials engineering, and artificial neural network modeling. He is a licensed professional engineer in the state of New Mexico. Dr. Arifuzzaman may be reached at [marifuzzaman@kfu.edu.sa](mailto:marifuzzaman@kfu.edu.sa)

**AYED ALLUQMANI** is an associate professor of civil and structural engineering at the Islamic University of Madinah. He earned his BSc in Civil Engineering from Umm Al-Qura University, Makkah; his MSc in Structural and Foundation Engineering from Herriot-Watt University, UK; and PhD in Civil Engineering from Strathclyde Univer-

# AN EXPERIMENTAL STUDY OF COLLOID LIQUID BRIDGE AND FORCE DYNAMICS IN REAL-TIME PROCESSES

Nhat Le, Minnesota State University; Shaobiao Cai, Minnesota State University; Yongli Zhao, St. Cloud State University

## Abstract

Friction and adhesion are of great interest in applications related to liquid-solid interfaces, especially when high relative motion and liquid-caused infinitesimal interaction forces are involved. In this study, the authors designed and fabricated a novel experimental apparatus to perform measurement and analysis tasks at the liquid-solid contact interface. Presented here are the liquid bridge forces under dynamic cyclic processes in real time continuous processes. The relationship between the liquid shape and process dynamic forces were visualized. The characteristics of solid-liquid interface in dynamic state were analyzed. Factors such as mass/volume and distance to the effects of interfacial forces were calculated, compared, and explained. From this study, the authors provide insights on force dynamics in applications involving liquids on surface coatings.

## Introduction

Solid/particle-liquid interfaces can be found in many applications with moving liquids, such as lubricant in gear boxes, fuel in engines, liquid in piping systems, and especially in valve operations and biomedical applications. The interactions in the solid-liquid interface are more significant in applications with low load and fast separation, especially in nano/micro devices. Many studies have been done on liquid-mediated separation. Cai and Bhushan (2008) presented analyses for a fundamental understanding of the numerical physics of separation processes and showed insight into the relationship between meniscus and viscous forces. Experimental studies in the literature have primarily focused on the effect of adhesive force, due to factors such as surface size, liquid properties (surface tension, contact angle, and viscosity), and operating conditions (including temperature, humidity, and velocity). The effect of humidity on adhesion was studied by McHaffie and Lenher (1925) and showed that the thickness of the film and adhesion both increase with an increase in humidity. McFarlane and Tabor (1950) conducted quantitative studies on adhesion through several experiments and observed that, with a clean, hard surface in dry air, adhesion is negligible; however, adhesion is appreciable in moist air. Similar observations of the effect of humidity on adhesion were made by Miyoshi, Buckley, Kusaka, and Bhushan (1988).

Shi, Zhang, Liu, Hanaor, and Gan (2018) presented a study of dynamic contact angle hysteresis using liquid bridges under cyclic compression and stretching between two identical plates. Portuguez, Alzina, Michaud, Hourlier,

and Smith (2017) studied the evaporation of sessile water droplets with a specific device to create liquid bridges within a humid environment and between hydrophobic surfaces. Some factors were evaluated at different temperatures at a fixed relative humidity. Tadrist, Motte, Rahli, and Tadrist (2019) investigated a capillary bridge between two large plates (such as a Hele-Shaw cell). The temporal evolution of surface forces and mass transfers due to evaporation of the liquid were also measured. Xiao, Jing, Kuang, Yang, and Yu (2020) studied the liquid profile change and the involved capillary force via particle-particle and particle-plane pairs.

It is known that surface tension-driven self-alignment is a passive and highly accurate positioning mechanism that can significantly simplify and enhance the construction of advanced microsystems. Mastangeli, Zhou, Sariojac, and Lambert (2017) explained statics and dynamics of the self-aligning action of deformed liquid bridges through simple models and experiments. They further illustrated the fundamental aspects of surface patterning and conditioning, the deposition and confinement of liquids, the component feeding and interconnection to substrates through relevant applications in micro- and nanotechnology. Popov (2010) studied the stick-slip behavior of liquid-mediated contacts and observed that the mechanical properties of the liquid menisci could change the amplitude and period of the stick-slip phenomena. Dhital and Cai (2016) performed numerical modeling and studied the roles of meniscus and viscous forces during flat-on-flat liquid-mediated contact separation with different liquid properties. They further conducted experimental analysis to analyze the effect of surface roughness on static contact angle for different liquid properties. Figure 1 shows how the shape change of the liquid bridge during the separation process was captured without force measurement.

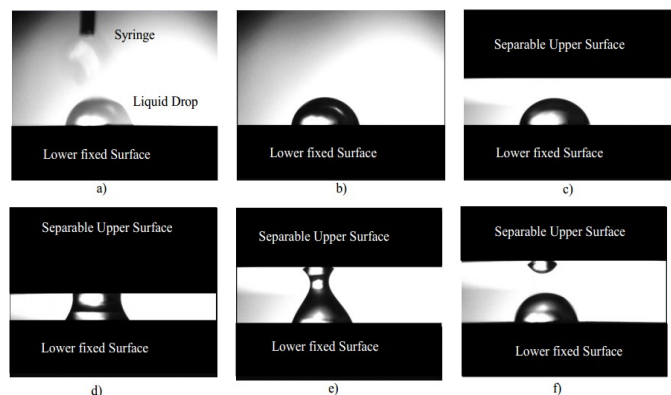


Figure 1. Series of liquid bridges in separation process (Dhital and Cai, 2016).

Among the many studies, experimental or numerical, there was lack of direct, real-time relationships between separation force and the change of liquid characteristics in realistic dynamic processes. The study of the force-liquid bridge in a real-time frame was needed. In this current study, the authors investigated the design and development of an apparatus for separating forces in real time. A motor-controlled system, an image analyzing system with a relatively high accuracy utilizing a microscope, and a DAQ system were created and used to study the dynamics of liquid bridge forces under continuous compression-tension cyclic processes in real time.

## Modeling of the Forces

The modeling of adhesive forces between liquids and solids may be divided into liquid-flat and liquid-particle situations. Idealizations are commonly used. In the modeling, the two contact surfaces were assumed to be rigid and smooth. The formed meniscus bridge was considered in mechanical equilibrium, and the liquid was incompressible with no thermal effect. The pressure was constant on a vertical, cross-sectional plane, though it was allowed to vary in a radial direction through the meniscus bridge during separation. The liquid bridge was arc-shaped with a constant volume during the process. In addition, the effect of gravity was neglected.

For a liquid-particle case with the particle sitting in fluid, the adhesive capillary force due to the background interface slope may be modeled using Equation 1 (Zhao, Cai, & Ratner, 2009):

$$\mathbf{F}_{lat}^{[bac]} = 2\pi\sigma Q_p \nabla h = -2\pi\sigma r_p \sin \beta_0 \tan(\theta_e - \beta_0) \nabla h \quad (1)$$

A combination of dynamic forces can cause particles to separate or aggregate. Figure 2 shows particle aggregation in fluid, due to the existence of adhesion. To gain better insight into force dynamics in a real-time frame, a simpler situation, a flat-on-flat case, was used in this study; Figure 3 depicts this scenario. With this situation, the liquid bridge dynamic process shape and the dynamic forces can be visualized.

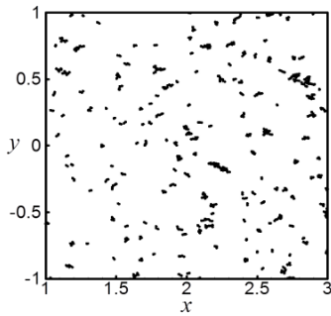


Figure 2. Simulated particle aggregation in the x-y plane when adhesion exists (Zhao et. al, 2009).

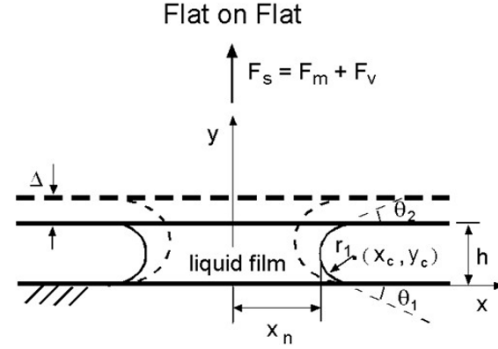


Figure 3. Diagram of a flat-on-flat situation (Cai and Bhushan, 2008).

The meniscus force, due to the formation of a meniscus bridge, can be obtained by integrating the Laplace pressure over the meniscus area and adding the surface tension effect acting on the circumference of the interface. For the separation of the liquid bridge between two flat surfaces, the meniscus force can be calculated using Equation 2 (Cai and Bhushan, 2008):

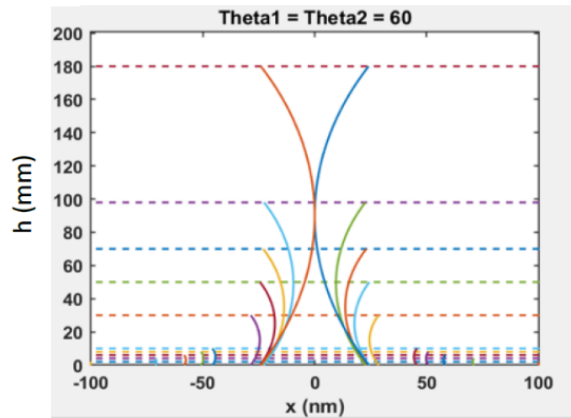
$$F_m = \frac{\pi x_{ni}^2 \gamma}{r_1} + 2\pi \gamma x_{ni} \sin \theta_{1,2} \quad (2)$$

Equation 3 gives the expression for the viscous force at a given separation distance,  $h_i$ :

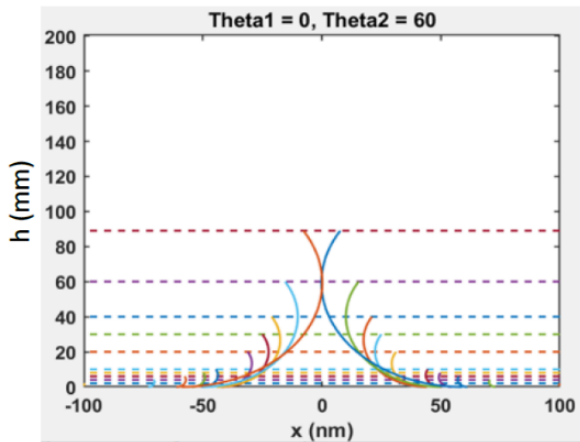
$$F_v = \frac{3\pi\eta x_{n0}^4}{4t_s} \left( \frac{1}{h_i^2} - \frac{1}{h_0^2} \right) \quad (3)$$

where,  $x_{n0}$  is the initial meniscus neck radius,  $\gamma$  is surface tension,  $\eta$  is viscosity,  $\theta$  is contact angle,  $x_{ni}$  is the neck radius of the liquid at the cross section on the horizontal plane,  $t_s$  is the separation time, and  $h$  is the separation height with subscript 0 indicating initial and  $i$  indicating the  $i_{th}$  step.

Figures 4(a) and 4(b) show the results of meniscus bridges in the separation process for a constant volume during separation of two flat surfaces, with  $h_0 = 2$  nm,  $\gamma = 72$  mN/m, and  $x_{n0} = 100$  nm. Figure 4(a) shows the results at contact angles  $\theta_1 = \theta_2 = 60^\circ$ , and Figure 4(b) shows the results at contact angles  $\theta_1 = 0^\circ$  and  $\theta_2 = 60^\circ$ . In order to investigate the properties of each force, the forces should be observed separately. From the force equations, the change in separation time will not affect the meniscus force. However, the viscous force decreases with an increase in separation time. Figure 5 shows the meniscus force and viscous force for a liquid with  $\eta = 0.89$  at separation times of  $t_s = 0.1$  s, 0.001 s, and 0.0001 s, respectively. It can be seen that the viscous force may be neglected at separation times of  $t_s = 0.1$  s or longer for the configuration, since the magnitude is about zero. These observations are the basis for the design of experiments.



(a)  $h_0 = 2 \text{ nm}$ ,  $\gamma = 72 \text{ mN/m}$ ,  $x_{n0} = 100 \text{ nm}$ , and contact angles  $\theta_1 = \theta_2 = 60^\circ$



(b)  $h_0 = 2 \text{ nm}$ ,  $\gamma = 72 \text{ mN/m}$ ,  $x_{n0} = 100 \text{ nm}$ , and contact angles  $\theta_1 = 0^\circ$ ,  $\theta_2 = 60^\circ$

Figure 4. The diagram of meniscus in the separation process.

## Experiment Design

Figure 5 shows that the viscous force is around zero at a separation time of  $t_s = 0.1 \text{ s}$  for the configurations. This allows for the design of a process to study the meniscus and viscous forces separately. Also, in experimental technique design, the idealization typically used in the modeling of liquid bridges in separation is not needed. Instead, a realistic laboratory environment was used. It should be noted that the liquid breaks before the neck radius is reduced to zero. Therefore, the actual breaking time and breaking distance must be smaller or much smaller than what is observed in theoretical simulations. For comparison purposes, the chosen separation time for this study was  $t_s = 20 \text{ s}$  for a 13 mm separation distance. The viscous force can be ignored at this separation time. Based on these parameters, the average velocity for the linear stage was  $13/20 \text{ mm/s}$  ( $0.65 \text{ mm/s}$ ) in

magnitude with a maximum separation force of 3.2 mN. To control the movement of the upper surface, a motor-lead screw mechanism was chosen among the many options to generate linear motion, due to the fact that it is easy to control, affordable, and simple to assemble and maintain.

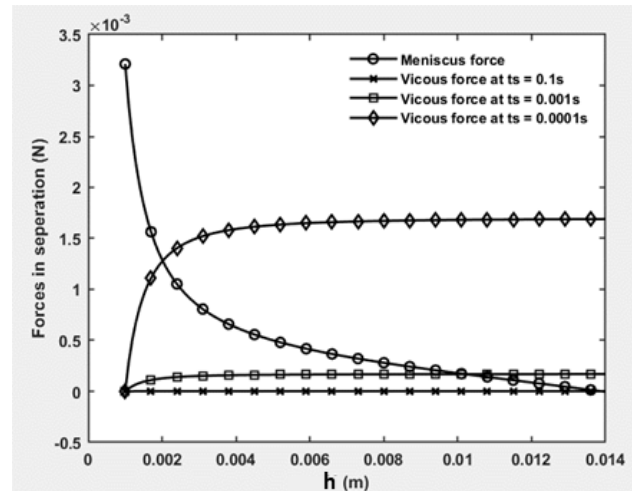


Figure 5. The plot of meniscus and viscous forces in separation process ( $h_0 = 1 \text{ mm}$ ,  $\gamma = 72 \text{ mN/m}$ ,  $x_{n0} = 3 \text{ mm}$ , and contact angles,  $\theta_1 = \theta_2 = 60^\circ$ ,  $\eta = 0.89 \text{ cP}$ , and  $t_s = 0.1, 0.001$  and  $0.0001 \text{ s}$ , respectively).

The two main components of the motorized linear actuator were a screw-nut slide and a driving motor. There were several options for the driving motor, such as DC motor, servo motor, and stepper motor. A DC motor requires an encoder for speed control; thus, a servo motor was a better choice for position control. A stepper motor is good for both speed and position controls, so it was chosen for this application to control both speed and position. The chosen lead screw had a lead of 1.27 mm. The load and friction of the positioning slide were estimated to calculate the acceleration needed for sizing the power of motor, following the SureStep™ Stepping Systems user manual (2019) for the Bipolar Stepper Motor Hybrid Frame Size 23 200 Step 2A 3.2VDC, which has a holding torque capability of 120 N·cm.

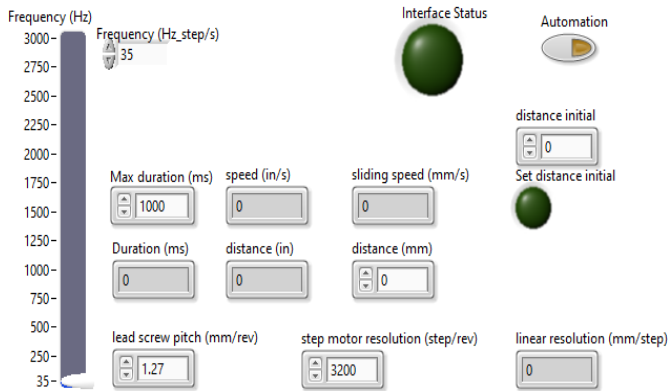
To control the motor, the Arduino was connected to an appropriate power circuit and controlled by a computer with a LabVIEW interface. The guidance in the Big Easy Driver Hookup Guide of TONI-K was used to determine the limit voltage and current of the power supply for the driver circuit and configurations. The stepper motor receives a pulse signal to operate, and its speed is controlled exactly by the frequency of the signal. The stepper motor stops if the signal pulse is missing or there is an overloaded. LabVIEW has an Arduino command that can request Arduino to generate a signal with an exact frequency. In this way, the tolerance of the frequency or the speed of the stepper motor was able to be controlled under 1%.

LabVIEW with a RS232 interface was used to program the interface. Figure 6 shows an example of the motor-control interface and its corresponding VIs. Figure 6(a) shows examples of the input to control the stepper motor and some unit conversion data, while Figure 6(b) presents the corresponding VIs. The “Frequency” input in steps/second was used to control the speed of the motor. The frequency, the stepper motor resolution, and the lead screw were used to calculate the sliding speed. The controlling signal to the stepper motor block received data from the input section and sent them to physical devices. In order to obtain measurement data, a precision balance with an appropriate range was used to measure the force in mN. The balance used was an Ohaus Explorer 124/AD with a load cell. Table 1 lists the range, readability, and repeatability of the balance. There were internal, external, and automatic calibrations included in the balance. The automatic calibration allowed the balance to be calibrated by its internal mass in a certain period or when the temperature changed. The internal mass could be adjusted with the standard mass with the available AutoCal adjustment option.

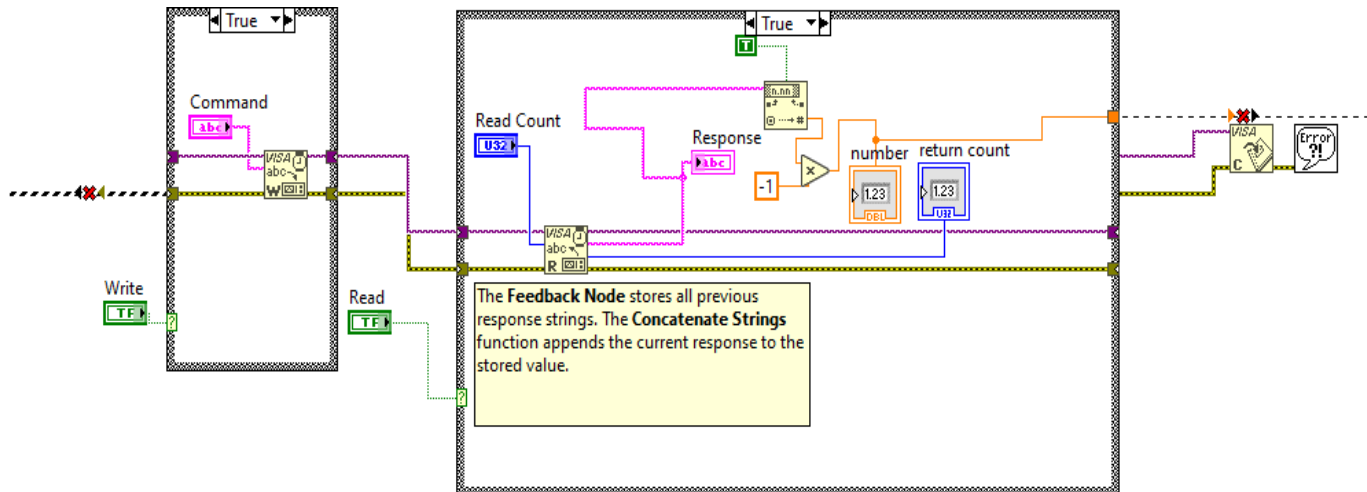
Table 1. Balance-parameter datasheets.

Capacity (g)	120	220	320	220	420	620	1100
Readability (g)	0.0001			0.001			
Verification Interval (g)	0.0001				0.01		0.01
Class	I		-	II	-	I	
Repeatability std (g)	± 0.0001			± 0.001			
Linearity (g)	± 0.0001			± 0.002			

Figure 7(a) shows the setup interface of the weight balance, while Figure 7(b) shows the corresponding VIs. To set up the interface, the time set to read values needed to be longer than the minimum transferring time of the balance to ensure the reading process without interruption. The reading rate could reach 10 Hz or 10 readings per second. A positioning slider with 15 lbs. of static loading capacity and 1.500 inches in travel length with a suitable lead and tolerance were chosen for the system. A flexible shaft coupler was used to connect the motor and the slide lead screw. The axis of the positioning slider needed to be aligned with the axis of the motor, and the two separated surfaces needed to be parallel to each other. To align the axes, the positioning slider was fixed on the frame and the position of the motor on the frame was adjustable. Figure 8 shows the components of the system. The entire frame of the slide was placed inside the weight balance, which was covered with glass to prevent external impacts. The samples and the sample holder were designed to allow quick and precise changes. The weight balance had adjustable legs and level indicator in order to level the balance pan. The design was able to test solid surfaces with different properties and surface characteristics.

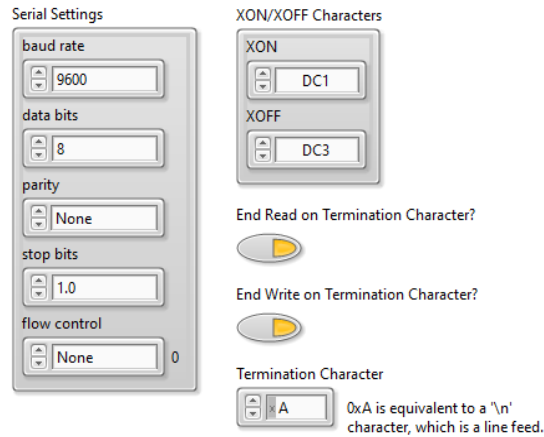


(a) Control interface of data input.

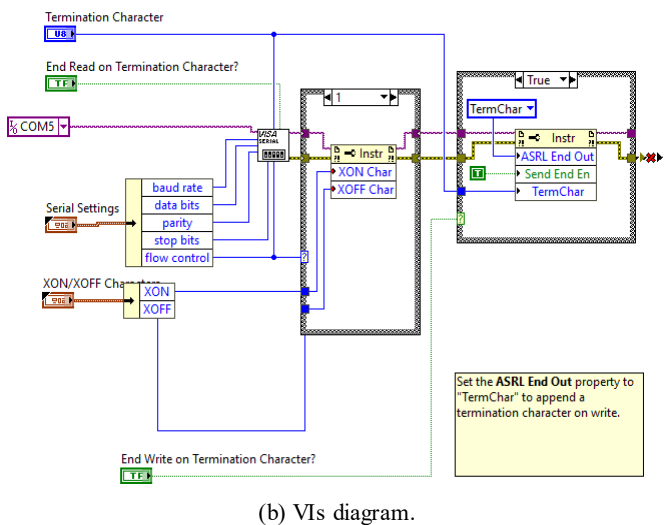


(b) The VIs of data input.

Figure 6. Example of the input section to control motor.



(a) Controlling interface panel.



(b) VIs diagram.

Figure 7. Example of program interface for weight balance with communication parameters.

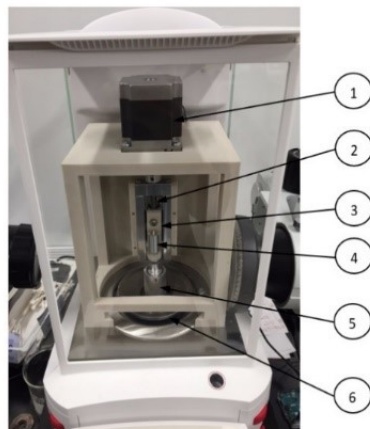


Figure 8. The positioning slider in the system: 1-stepper motor, 2-lead screw, 3-sample holder, 4-5 the sample, and 6-the weight balance.

Figure 9 shows that, in the system, in order to ensure that the two flat surfaces were parallel, the surfaces were adjusted to parallel to the ground reference datum using a caliper. Since the stepper motor slider was a non-feedback system, the position of the slider was calculated from the speed of the motor and the slider's resolution. A tolerance of 0.025 mm was used to measure the displacement of the slider, and it was compared with the position value calculated by the program. The tolerance of the position was  $\pm 0.05$  mm.

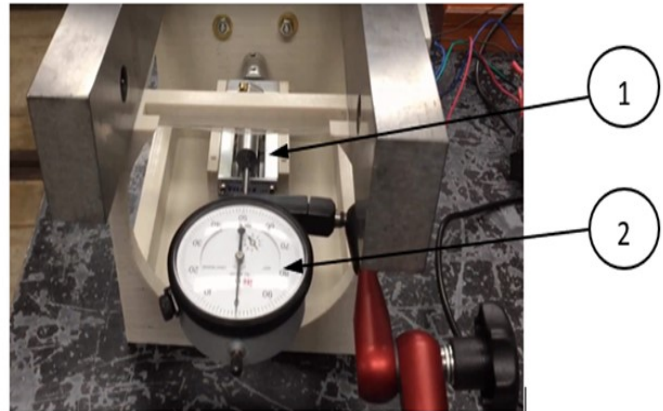


Figure 9. Slider position calibration setup: 1-the positioning slider and 2-the caliper.

## Sample Design

The samples were machined using aluminum 6061 and smoothed with 240-grit sandpaper. To ensure the parallelism between the alignment surfaces for assembly, the samples and the inner sleeve were machined with the same lathe. Figure 10 shows some of the samples created. To ensure even distribution and roughness on the entire surface, the contacting surfaces were maintained parallel, and the samples were rotated during the grinding process. For the top sample, a groove was created near the sleeve to ensure good alignment when inserting the sample into to the sleeve.

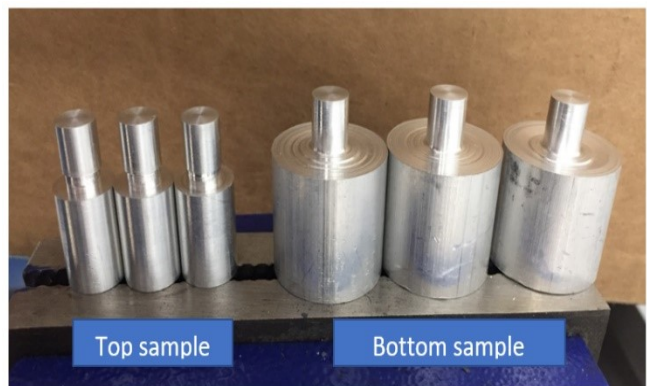


Figure 10. Examples of the samples used in the experiment.

## Experimental Testing and Results

To obtain good results for the involved forces resulting from a liquid bridge—parameters such as the distribution of roughness on the surface, the volume of liquid, environment moisture, the tolerance of linear translation system, the maximum contact circle between liquid and solid, the static electric force of two metal surfaces, and evaporation process—needed to be controlled. Figure 11 shows the complete measurement system. The system had six major components: 1-background lighting, 2-positioning slide system, 3-weight balance, 4-microscope for image recording, 5-scope stand, and 6-control and DAQ system. During measurement, the force and the real-time liquid bridge images could be recorded simultaneously. With the setup, the changes of the force could be observed with the corresponding changes in shape of the liquid bridge. This setup could be used to conduct experiments on different surface properties, different liquids, or different velocities.

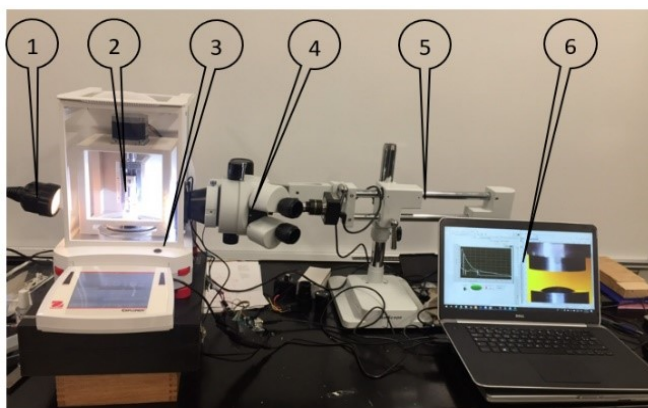


Figure 11. The experimental system's components: 1-background lighting, 2-positioning slide system, 3-weight balance, 4-microscope for image recording, 5-scope stand, and 6-control and DAQ system.

To make the surface roughness relatively even at any arbitrary position on the surface, the ground surface was adjusted parallel to the grinding surface, and the ground surface was rotated during the grinding process. To limit the effect of moisture, an alcohol with a purity of 91% was used to prepare/clean the surface before allowing it to dry completely. The tolerance of the slide was set at 0.05 mm and the two surfaces were put in contact in order to eliminate static electric charges. The distance was reset to zero after every experiment. The volume of liquid was controlled through mass using the weight balance. The volume of each drop was controlled by using a mass of 0.015g. The tolerance of the liquid mass was controlled within  $\pm 5\%$  through the weight balance with a readability of 0.0001g. Each time, the liquid was compressed to the minimum distance followed by immediately pulling of the bridge to prevent the evaporation. Experiments were conducted using water with various surface roughness. Tests were performed under the same

room conditions and initial setup. Table 2 lists the experimental control parameters and the properties of water. The water evaporation rate was indicated by the vapor pressure of liquid. The vapor pressure of water at ambient temperature is 25.8 mmHg. Experiments with water droplets were conducted with aluminum surfaces smoothed with 240-grit sandpaper.

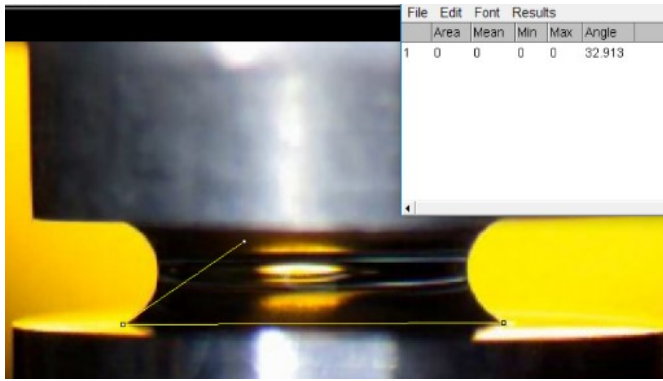
Table 2. The experiment conditions and parameters.

Density	1000 kg/m <sup>3</sup>
Surface tension	7.2 x 10 <sup>-2</sup> N/m
Controlled mass	1.5 x 10 <sup>-5</sup> kg
Controlled volume	1.5 x 10 <sup>-8</sup> m <sup>3</sup>
Temperature	25°C
Humidity	50%
Vapor pressure	25.8 mmHg
Surface material	Aluminum 6061
Minimum distance	0.5 ± 0.05 mm
Operation velocity	0.079 mm/s

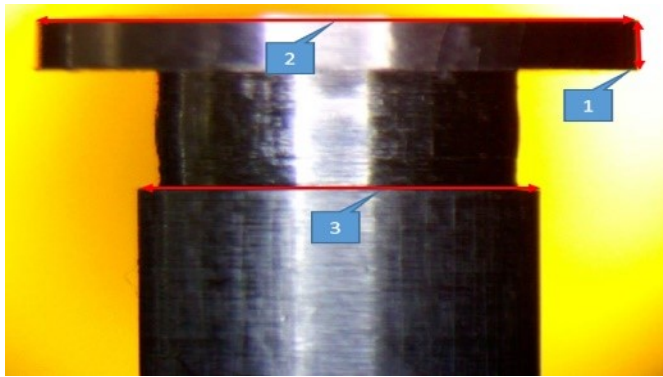
### Imaging and process

Figure 12(a) shows the image that was obtained from the recorded video. To measure the angle, Software ImageJ was used, and three points were applied to create two intersecting lines, as shown. The tolerance of the angle measurement depends on camera setup, the height of the liquid bridge surface, the resolution of the image, and the calibration. It also depends on the way that the construction lines of angle were defined. The position of the construction lines may vary with the subjective observation of people who take the measurement and with the resolution of the image. The tolerance for the angle measurement was about  $\pm 4^\circ$  from the measurement method. In this study, a generous tolerance of  $\pm 10^\circ$  was considered in order to compensate for the lack of calibration of the angle gauge. It should be noted that the distance in an image is represented by the number of pixels.

To get a spatial length of a line (needing to be measured) from a captured image, a line with a known length (gaging line) and its image-pixel aspect ratio, and the to-be-measured line must be defined. The measured line and the gaging line must be parallel on the same surface to the surface on which the image is taken. For instance, lines #1 and #3 in Figure 12(b) are on the same vertical surface and parallel to the image taken surface and the surface passing through the centerline of the concentric cylinders. The length of line #1 can be calculated by multiplying the total number of pixels of line #1 and the image pixel aspect ratio of line #3 (with known physical length). The tolerance of this method is about 5-7%.



(a) Example of a contact angle measurement.



(b) Distance dimension representation in pixel.

Figure 12. Contact angle and distance measurements.

## Liquid-Bridge Process Shape

Figure 13 shows the phenomenon of liquid drop expansion. The diameter of the contacting circle between the liquid drop and the surface depends on the surface characteristics and the way the liquid drop is dispensed on the surface. Factors such as the amount of liquid, the velocity of dispensing, and the sitting height of the liquid dispenser can all affect the shape of the drop on a surface. The contacting circle of liquid drop on the surface expands when adding liquid.

Figure 14—steps 1-9—shows examples of the dynamic shape change and the movement of the base contact circle of a liquid bridge in compression and tension processes. The rectangle used in the figure is a reference dimension. Steps 1-3 show that a concaved liquid bridge is formed upon the hydrophilic upper surface touching the liquid. A contact angle is formed upon the upper surface touching the liquid drop, and the base contact circle maintains the same without change. Further approaching causes an increase in contact angle without outward expanding to cause a squeezing effect (compression) until the contact angle reaches an angle of about  $90^\circ$  at step 3. After that, the contact base circle expands until the two surfaces reach the minimum preset-

ting distance at step 4. This observation shows that if the minimum distance between the two approaching surfaces is not small enough to expand the contact circle, the contact circle size relies on the way the drop initially sits on the surface. To achieve stable, comparable results and eliminate the effect of how the drop is released, the distance between the two surfaces must be small enough so that the contact circle can expand completely at the time when the distance between the two surfaces reaches a minimum. From this method, the initial contact circle where the liquid bridge begins to be stretched can be defined by the minimum distance and the volume of liquid only. This way, random errors caused by the initial conditions and the way of dropping the liquid on the surface can be minimized.

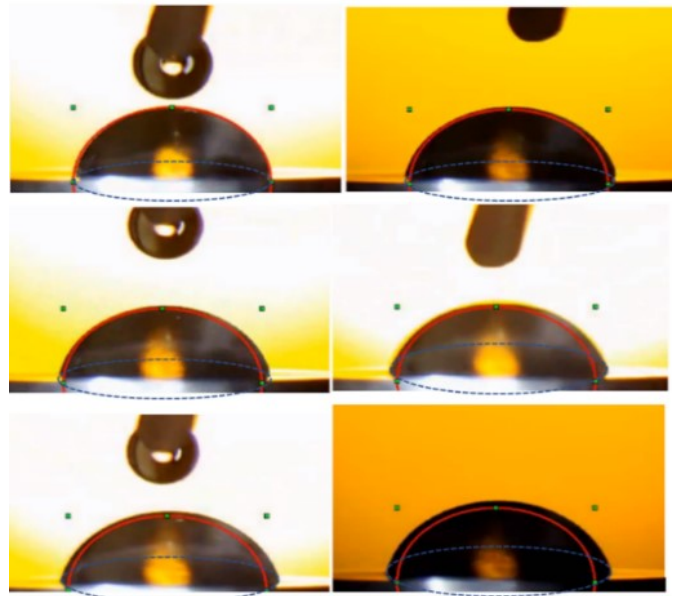


Figure 13. Contact circle expansion when more liquid is added (dashed line is for visualization purpose only).

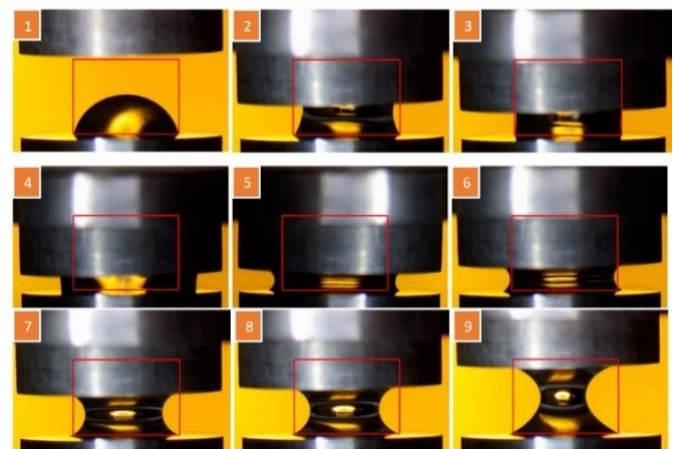


Figure 14. Process shapes change and contact base circle's movement of liquid bridge in compression and tension.

The separation process starts at step 5, where the receding of the liquid bridge can be observed. The contact angle changes from the advancing angle to the receding contact angle at step 5. At this step, the contact base circle is the largest and a stable contact is formed. Starting from step 6, the liquid base circle starts to reduce continuously to its original size shown in step 1, and the contact angle remains constant until the breakup of the liquid (steps 7-9).

## Dynamic Process Force in One Cycle

The dynamic change in shape leads to a change in process forces. Figure 15 shows the corresponding chart of dynamic forces describing the entire process. Four stages can be divided based on the observation. Stage I is approaching the process and Stage II is a process of liquid compression to a controlled minimum distance. Stage III is a transition period from advancing compression to receding separation process, and Stage IV is the continuously separating process. Stage I (in Figure 15) corresponding to step 1 from Figure 14, which shows the process of how the upper surface approaches the liquid drop. In Stage II, corresponding to steps 2-4, the force increases immediately as the upper surface touches the liquid drop, due to the formation of the meniscus. In this section, the force increases, due to the change in contact angle, meniscus radius (in the vertical plane), neck radius in the horizontal plane, and the viscous resistance.

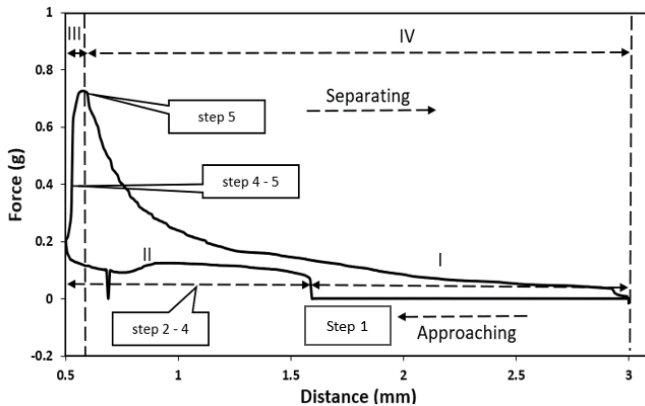


Figure 15. The total force chart for the continuous compression and stretching/separating process of liquid bridge between two aluminum flat surfaces smoothed with 240-grit sandpaper.

The downward peak in this stage was a missing data point in the data acquisition process. In Stage III, corresponding to steps 4 and 5, the total force increased rapidly when the meniscus size was at its largest. The meniscus force reached its maximum value when the contact angle changed from the advancing angle to the receding contact angle at step 5. The authors observed that the decrease in contact angle with the same dimension of liquid bridge led to a decrease in force caused by surface tension, based on the second term in Equation 2. However, the decrease in meniscus radius ( $r_l$ ) and the increase in size ( $x_{ni}$ ) due to compression leads to a

significant increase in the meniscus force (Equation 2). The increase in the resultant force showed that the Laplace pressure and the size of the meniscus were the dominant causes of the resultant maximum separating force. During the continuous separation process (Stage IV), corresponding to steps 6-9, the force decreased rapidly to a low level and slowed down later until liquid break.

## Dynamic Force in Cyclic Processes

Using the control parameters listed in Table 2, the dynamic total force-distance data for each prepared sample pair was recorded. The experiments included five complete cycles of compression from a height of 2mm to prevent the breaking of the liquid bridge after the first cycle. Figure 16 shows the force versus the distance under repeated processes. The speed of the slider, the distance, and the force measurement were accurately controlled. The repeated cycles presented the stability of the system. The exception at the first compression curve can be explained by the initial wetting state of the surface. The wetting state of the surface changed the advancing contact angle, as noted previously.

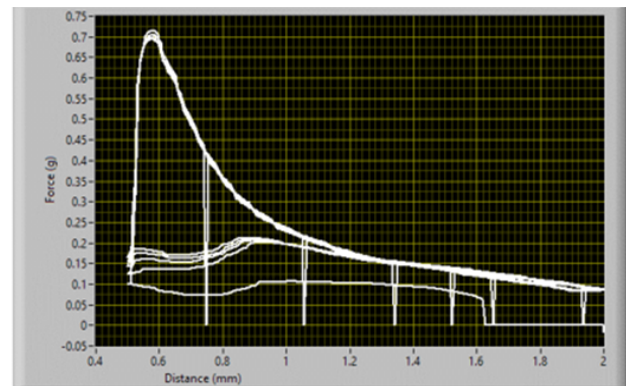


Figure 16. The force displacement curve of the water bridge under repeated compression and tension cycles.

## Comparison of Experimental and Analytical Prediction

The experimentally measured force curve for a fixed amount of water (0.015g) was further compared with the theoretical separating force curve using the same experimental parameters. Figure 17 shows the comparison. The angle used for theoretical calculations was the receding angle, measured when the liquid bridge was being stretched. The maximum force in the experimental data is outlined by a box on the graph. Overall agreement of the experimental force curve and that predicted by the theoretical equation for separation was good, although a small shift in location where the maximum separation force occurred was observed. This was due to the delayed formation of a stable contact angle after the recession in the experiment, as discussed earlier, but the theoretical equation was “static.”

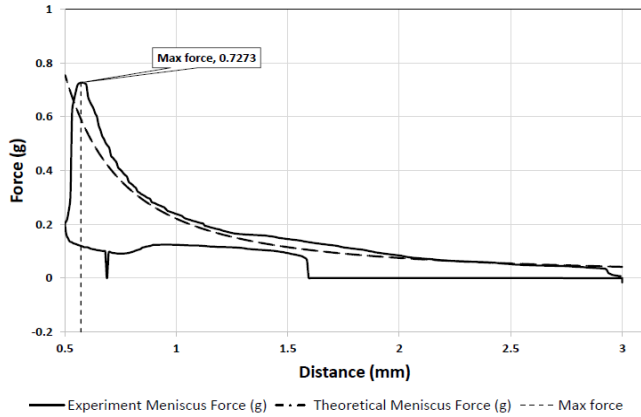


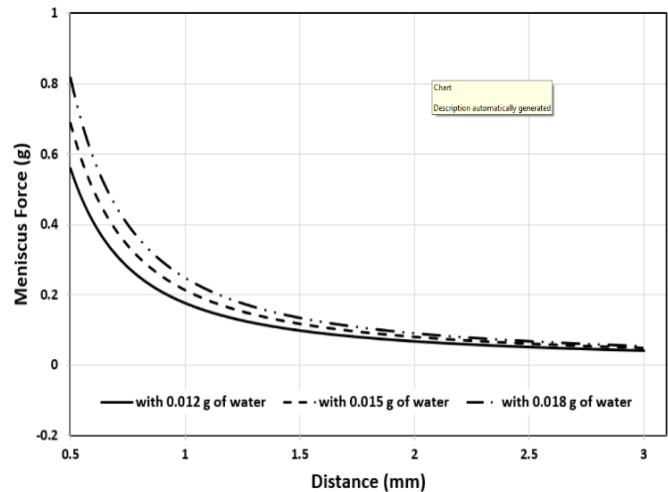
Figure 17. Comparison between the experimental force-distance curve and that defined by the theoretical equation.

For various masses, 0.015 g of water (reference) and changes of  $\pm 20\%$  (0.012 g, 0.015 g, and 0.018 g) were used to study the variation. Figure 18(a) shows—from calculations using Equation 2—that the corresponding change in the maximum meniscus force prediction would be considerable at about  $\pm 19\%$  (0.56 g, 0.69 g, and 0.82 g). From experimentation, the mass was well controlled, and the major factor causing mass variation was evaporation for volatile liquids. Since the tolerance of mass variation was strictly controlled, under  $\pm 5\%$ , the mass-related force variation could be ignored. On the other hand, mass change was believed to be one of the major factors leading to the change of force, if it existed. Figure 18(b) shows that, for the effect of minimum distance, based on a 0.5 mm minimum distance reference with changes of  $\pm 10\%$  (0.45 mm, 0.5 mm, and 0.55 mm), the corresponding change in the maximum meniscus force using the equation prediction would be from  $-15\%$  to  $21\%$  (0.58 g, 0.69 g, and 0.83 g). The force variation caused by minimum distance was significant, if it existed.

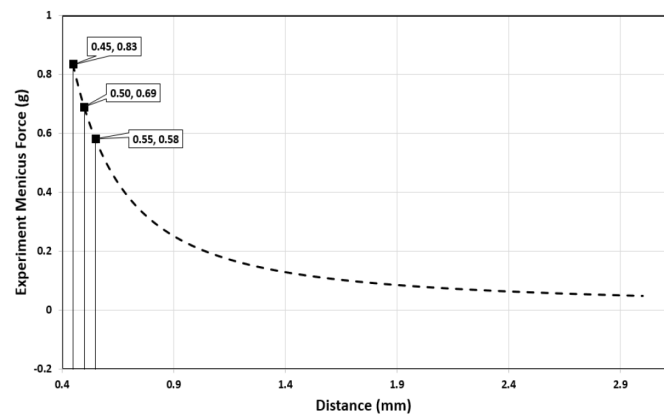
## Conclusions

This study provided a real-time dynamic analysis of liquid-solid interactions at the contact interface. A novel experimental apparatus was successfully designed and fabricated to perform the tasks. The characteristics of solid-liquid interface in static and dynamic states were demonstrated in the study with visual demonstration. It was observed that the approach of two solid surfaces caused an increase in contact angle without outward expansion of the base contact circle until the contact angle reached about  $90^\circ$ . The contact base circle expanded upon reaching this  $90^\circ$  angle during the time that the two surfaces approached each other until they reached the minimum preset distance. The size of the contact base circle relied on the way the drop initially sat on the surface, unless the distance between the two approaching surfaces was small enough. The contact base circle eventually resumed its original size during the separation process that followed.

Dynamic forces, distance and liquid bridge shape change of a contact system in real time compression, tension, and cyclic processes were presented for the first time. Insights between the liquid shape and dynamic force were analyzed. Factors such as mass and distance affecting the dynamic force were studied. The experiments showed that the involved dynamic forces could be divided into four distinctive stages. For the compression-tension cycle, force increased to its maximum at the transition period from compression to tension. If separation occurred without a waiting period, the maximum force occurred after pulling to a small distance, due to the contact angle (major) change and viscous resistance. The dynamic force quickly decayed to zero after passing the maximum point. Mass (or volume) of the liquid and the minimum surface initial distance can significantly affect the separation force. Cyclic processes were compared with single-cycle compression-tension. Good agreement demonstrated repeatability of the process.



(a) Mass



(b) Distance

Figure 18. Effect of mass and distance on the separation process with the same initial conditions for water.

---

## References

- Cai, S., & Bhushan, B. (2008). Meniscus and viscous forces during separation of hydrophilic and hydrophobic surfaces with liquid-mediated contacts. *Materials Science and Engineering R*, 61, 78-106. doi.org/10.1016/j.mser.2007.03.003
- Dhital, P., & Cai, S. (2016). Study of Role of Adhesive Forces during Liquid-Mediated Contacts Separation. *International Journal of Modern Engineering*, 17(1), 78-84.
- Mastrangeli, M., Zhou, Q., Sariolac, V., & Lambert, P. (2017). Surface tension-driven self-alignment. *Soft Matter*, 13, 304.
- McFarlane, J. S., & Tabor, D. (1950). Adhesion of solids and the effect of surface films, *Proceedings of the Royal Society A*, 202, 224-243. doi.org/10.1098/rspa.1950.0096
- McHaffie, I. R., & Lenher, S. (1925). The adsorption of water from the gas phase on plane surfaces of glass and platinum. *Journal of Chemical Society*, 127, 1559-1572.
- Miyoshi, K. D., Buckley, T., Kusaka, C., & Bhushan, B. (1988). *Effect of water vapor on adhesion of ceramic oxide in contact with polymeric magnetic medium and itself*. In B. Bhushan & N.S. Eiss (Eds.), *Tribology and Mechanics of Magnetic Storage Systems* (pp. 12-16). Society of Tribologists and Lubrication Engineers.
- Popov, V. (2010). *Contact mechanics and friction physical principles and applications*. Heidelberg: Springer.
- Portuguez, E., Alzina, A., Michaud, P., Hourlier, D., & Smith, A. (2017). Study of the Contact and the Evaporation Kinetics of a Thin Water Liquid Bridge between Two Hydrophobic Plates. *Advances in Materials Physics and Chemistry*, 7, 304.
- Shi, Z., Zhang, Y., Liu, M., Hanaor, D. A. H., & Gan, Y. (2018). Dynamic contact angle hysteresis in liquid bridges. *Colloids and Surfaces A: Physicochemical and Engineering Aspects*, 555, 365-71. doi.org/10.1016/j.colsurfa.2018.07.004
- SureStep™ Stepping Systems user manual (2019). *STP-SYS-M-WO* (5<sup>th</sup> ed.). Revision B.
- Tadrist, L., Motte, L., Rahli O., & Tadrist, L. (2019). Characterization of interface properties of fluids by evaporation of a capillary bridge. *Royal Society Open Science*. doi.org/10.1098/rsos.191608
- Xiao, F., Jing, J., Kuang, S., Yang, L., & Yu, A. (2020). Capillary forces on wet particles with a liquid bridge transition from convex to concave. *Powder Technology*, 363, 59-73. doi.org/10.1016/j.powtec.2020.01.020
- Zhao, Y., Cai S., & Ratner, A. (2009). A Numerical Computation Model for Low-Density Lipoprotein (LDL) Aggregation and Deposition in the Human Artery. Paper presented at the 62<sup>nd</sup> Annual Conf. of American Physical Society's DFD, 22-24 Nov. Minneapolis, MN.

## Biographies

**NHAT LE** is a graduate student in the Department of Mechanical and Civil Engineering at Minnesota State University, Mankato. Mr. Le may be reached at [nhat.le@mnsu.edu](mailto:nhat.le@mnsu.edu)

**SHAOBIAO CAI** is an associate professor in the Department of Mechanical and Civil Engineering at Minnesota State University, Mankato. His areas of expertise and research interests include interfacial contact mechanics and tribology, mechanical failure of materials, layered medium design, and the application of DFMA principles in the development of robust design solutions. He is a registered professional engineer in the state of Minnesota. He is a member of the American Society of Mechanical Engineers, the Society of Tribologists and Lubrication Engineers and American Society of Engineering Education. Dr. Cai may be reached at [shabiao.cai@mnsu.edu](mailto:shabiao.cai@mnsu.edu)

**YONGLI ZHAO** is a professor in the Department of Mechanical and Manufacturing Engineering at St. Cloud State University. Dr. Zhao may be reached at [yzhao@stcloudstate.edu](mailto:yzhao@stcloudstate.edu)

# COMPARATIVE TANGENTIAL STRESS ANALYSES OF CURVED BEAMS

MA Muktadir, North Carolina A&T State University; Paul Akangah, North Carolina A&T State University; Sun Yi, North Carolina A&T State University

## Abstract

Many researchers have attempted to find the solution to a curved beam under load. However, the stress values arrived at failed to satisfy the boundary conditions. Curved beams find critical practical applications in chain links, crane hooks, pipe bends, and curved segments of machine tool frames. Accurate determination of stresses in curved beams is essential in preventing catastrophic failure, leading to loss and reduced life of properties. In this current study, the authors used three methods: 1) advanced computational tools to compare the strength of materials (SOM), elasticity analysis (EA), and finite element analysis (FEA) of the curved beam tangential stress of various sections. The SOM analysis was performed first, in which three cross-sections were considered: rectangular, square, and circular. All cross-sections showed similar inner and outer tangential stress ratios. Next came the EA approach in which two airy functions were used to calculate tangential stress, the results for which differed slightly between the square and rectangular cross-sections. Finally, the finite element analysis was conducted by using ANSYS to analyze rectangular, square, and circular 3D curved beams. In that case, all cross-sections showed similar results to the SOM approach. This study represented a unique comparison of a curved beam's tangential stress, by comparing different sources found in various studies and articles.

## Introduction

There is a wide range of applications of curved beams, for example, to manufacture a small device and manufacturing of an aircraft. That type of beam is more efficient in transferring loads than straight beams. This transfer in the curved beam is affected by bending, shear, and membrane action (Mathiyazhagan & Vasiraja, 2013). In this study, the authors compared tangential stress by using the strength of materials (SOM) analysis, elasticity analysis (EA), and finite element analysis (FEA) of the curved beam of various sections. The development of the beam and bending relations should have the same cross-section throughout the beam's length. However, the varying cross-section can be caused when considering the curved beam's practical use (Subramani, Subramani, & Prasath, 2014). Figures 1 and 2 show the 2D and 3D curved beams, respectively, where  $a$  is the inner radius,  $b$  is the outer radius, and  $o$  is the circular center. The moment was applied from both ends of the beam. As the moment were the same from both ends, symmetry analysis was considered by keeping the mid-plane

fixed. For all approaches of calculation and analysis, the beam's cross-section outer radius was three times the inner radius.

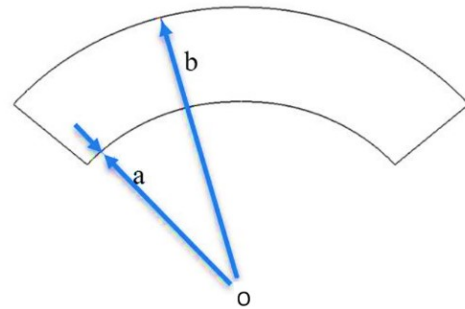


Figure 1. 2D Schematic view of a curved beam.



Figure 2. 3D Rendering of a curved beam.

## Literature Review

Beam elements have played a vital role in modeling mechanical engineering structures, but curved beams are more efficient in transferring loads than straight beams (Mathiyazhagan & Vasiraja, 2013). Wang and Liu described a solution for curved beams with the airy stress function method (2013). In that article, two airy stress functions were presented for elasticity analysis (EA). Another study determined the stress component by EA (Kılıç, & Aktaş, 2002). Chavan and Zhou (2016) presented a stress calculation for slender curved beams and simulated curved beam stresses (Chavan, & Zhou, 2016). Yet another study used FEM to analyze a curved cantilever beam's static and dynamic analysis with different cross-sections and different curvature types by varying load and direction (Mathiyazhagan & Vasiraja, 2013).

Other research described the FE analysis of non-linear and linear elastic beams, while considering the shear deformation, and derived a new formulation for the linear beam and discussed the theory of Reissner for non-linear beams (Ibrahimbegoviæ, & Frey, 1993). Bağci (1991) showed the exact elasticity solutions of curved beams for stresses and deflections and developed the expression of tangential, radial stresses for different conditions, moment, force, and combined loading for different cross-sections exponentially varying trapezoidal and T-sections. As the high-rise building increases, due to the increasing population, curved beams are becoming popular for different construction projects, including highway crossing, metrorail, the bridge on the big river, etc. Subramani et al. did the FE analysis for the composite concrete structure (2014). Lin and Lin (2011) used the Lagrangian and Eulerian to derive the finite deformation analysis, while taking into consideration the deformed curvature radius under static loading and presented analytical solutions of the circular beam compared the results of ANSYS analysis.

Curved beams also have been used for energy harvesting. Nahid Hasid researched a THUNDER, which is a curved piezoelectric energy generator by finite element methods (Hasan, 2018). Curved beams have vast application areas, due to some unique advantages. One of which is the characteristic of keeping the elastic property while deformed to specific values. Tennis rackets, the arms of a robot, and stiffeners in aircraft parts are the examples of this kind of curved beam. A study presented the analytical solution of laminated curved beams and compared the finite element analysis with the ANSYS (Lin & Lin, 2011). The curved beam has also been made of a composite material, as used in aircraft manufacturing. Ismail (2014) assessed layered composite material curved beams in theoretical and experimental methodologies by computing the maximum stress and deflection of layer by layer and detecting the effect of curvature radius and shape of the curve of twelve cases.

## Methods

For this current study, one specific material was used for calculation and analysis. Table 1 shows the material and chemical composition of structural steels (ASTM International, 2019); Calderón, Bohórquez, Rojas, & Pertuz, 2021). For the SOM analysis, three types of curved beams were considered in calculating the ratio of tangential stress, square, rectangular, and circular. The authors assumed that the outer radius was three times the inner radius. Tangential or circumferential stress ( $\sigma_\theta$ ) in a curved beam can be written as Equation 1 (Boresi, Schmidt, & Sidebottom, 1985):

$$\sigma_\theta = \frac{N}{A} + \frac{M_o(A - rA_m)}{A_r(RA_m - A)} \quad (1)$$

where,  
 $N$  = normal traction  
 $M_o$  = applied moment

$R$  = the distance from the center of curvature of the curved beam to the centroid of the beam cross-section  
 $r$  = location of the element  
 $A$  = the cross-sectional area of the curved beam  
 $A_m = \int \frac{dA}{r}$  represents dimensions of length

Table 1. Material and chemical composition of structural steels.

Property	Value	Unit			
Density	7850.00	Kg m <sup>-3</sup>			
Tensile Yield Strength	250.00	MPa			
Compressive Yield Strength	250.00	MPa			
Tensile Ultimate Strength	460.00	MPa			
Compressive Ultimate Strength	0.00	Pa			
Chemical Composition (% ≤)					
C	Si	Mn	P	S	Cu
0.26	0.40	-	0.04	0.05	0.20

Assuming,  $N = 0$ , tangential stress can be written as Equation 2:

$$\sigma_\theta = \frac{M_o(A - rA_m)}{A_r(RA_m - A)} \quad (2)$$

Assuming that  $b$  is the outer radius and  $a$  is the inner radius,  $A$ ,  $R$ , and  $A_m$  can be written as follows (Boresi et al., 1985):

$$\begin{aligned} A &= (b-a)(b+a) \\ R &= (a+b)/2 \\ A_m &= (b-a) \ln(b/a) \end{aligned}$$

Now, from Equation 2, tangential stress can be written as Equation 3:

$$\begin{aligned} \sigma_\theta &= \frac{M_o \left( (b-a)^2 - r \left( (b-a) \ln \left( \frac{b}{a} \right) \right) \right)}{(b-a)^2 r \left( \left( \frac{a+b}{2} \right) (b-a) \ln \left( \frac{b}{a} \right) - (b-a)^2 \right)} \\ \sigma_\theta &= \frac{M_o \left( b-a-r \ln \left( \frac{b}{a} \right) \right)}{(b-a)^2 r \left( \left( \frac{a+b}{2} \right) \ln \left( \frac{b}{a} \right) - b+a \right)} \quad (3) \end{aligned}$$

$$\sigma_\theta = \frac{M_o(2a - r \ln 3)}{4a^2 r (2a \ln 3 - 2a)} \quad (\text{when } b = 3a)$$

$$\sigma_\theta = \frac{M_o(2a - r \ln 3)}{8a^3 r (\ln 3 - 1)}$$

When  $r = a$ , Equation 3 can be written as Equation 4:

$$\sigma_{\theta} = \frac{M_o (2a - a \ln 3)}{8a^3 a (\ln 3 - 1)} \quad (4)$$

$$\sigma_{\theta} = \frac{M_o (2 - \ln 3)}{8a^3 (\ln 3 - 1)}$$

When  $r = b = 3a$ , Equation 3 can be written as Equation 5:

$$\sigma_{\theta} = \frac{M_o (2a - 3a \ln 3)}{8a^3 3a (\ln 3 - 1)} \quad (5)$$

$$\sigma_{\theta} = \frac{M_o (2 - 3 \ln 3)}{24a^3 (\ln 3 - 1)}$$

The ratio of the tangential stress at  $r = b$  and  $r = a$  is defined as  $\gamma$  in Equation 6:

$$\gamma = \frac{(\sigma_{\theta})_{r=b}}{(\sigma_{\theta})_{r=a}}$$

$$\gamma = \frac{\frac{M_o (2 - 3 \ln 3)}{24a^3 (\ln 3 - 1)}}{\frac{M_o (2 - \ln 3)}{8a^3 (\ln 3 - 1)}} \quad (\text{from Equations 4 \& 5}) \quad (6)$$

$$\gamma = \frac{2 - 3 \ln 3}{6 - 3 \ln 3}$$

$$\gamma = (-)0.479$$

For rectangular cross-sections, A, R, and  $A_m$  were different. Given that the width of the rectangular cross-section was double the height, the height was parallel to the calculation axis, and the height of the rectangular cross-section was half of the width (Boresi et al., 1985):

$$\begin{aligned} A &= 0.5 (b-a) (b-a) \\ R &= (a+b)2 = (3b+b)2b \\ A_m &= 0.5 (b-a) \ln (b/a) \end{aligned}$$

Now, from Equation 2, stress can be derived as Equation 7. When  $r = a$ , Equation 7 can be written as Equation 8. When  $r = b = 3a$ , Equation 7 can be written as Equation 9. The ratio of the tangential stress at  $r = b$  and  $r = a$  is defined as  $\gamma$  in Equation 10. For circular cross-sections, A, R, and  $A_m$  can be written as follows, where  $a$  is equal to  $b$  (Boresi et al., 1985).

$$R = 2a$$

$$A = \pi a^2$$

$$A_m = 2\pi \left( 2a - \sqrt{(4a^2 - a^2)} \right) = 2\pi a (2 - \sqrt{3})$$

$$\sigma_{\theta} = \frac{M_o (A - rA_m)}{Ar(RA_m - A)}$$

$$\sigma_{\theta} = \frac{M_o \left( 0.5(b-a)^2 - r \left( 0.5(b-a) \ln \left( \frac{b}{a} \right) \right) \right)}{0.5(b-a)^2 r \left( \left( \frac{a+b}{2} \right) 0.5(b-a) \ln \left( \frac{b}{a} \right) - 0.5(b-a)^2 \right)}$$

$$\sigma_{\theta} = \frac{M_o \left( b - a - r \ln \left( \frac{b}{a} \right) \right)}{0.5(b-a)^2 r \left( \left( \frac{a+b}{4} \right) \ln \left( \frac{b}{a} \right) - b + a \right)} \quad (7)$$

$$\sigma_{\theta} = \frac{M_o (2a - r \ln 3)}{2a^2 r (a \ln 3 - 2a)} \quad (\text{when } b = 3a)$$

$$\sigma_{\theta} = \frac{M_o (2a - r \ln 3)}{2a^3 r (\ln 3 - 2)}$$

$$\sigma_{\theta} = \frac{M_o (2a - a \ln 3)}{2a^3 a (\ln 3 - 2)} = \frac{M_o (2 - \ln 3)}{2a^3 (\ln 3 - 2)} \quad (8)$$

$$\sigma_{\theta} = \frac{M_o (2a - 3a \ln 3)}{2a^3 3a (\ln 3 - 1)} = \frac{M_o (2 - 3 \ln 3)}{6a^3 (\ln 3 - 2)} \quad (9)$$

$$\gamma = \frac{(\sigma_{\theta})_{r=b}}{(\sigma_{\theta})_{r=a}}$$

$$\gamma = \frac{\frac{M_o (2 - 3 \ln 3)}{6a^3 (\ln 3 - 2)}}{\frac{M_o (2 - \ln 3)}{2a^3 (\ln 3 - 2)}} \quad (\text{from Equations 8 \& 9}) \quad (10)$$

$$\gamma = \frac{2 - 3 \ln 3}{6 - 3 \ln 3}$$

$$\gamma = (-)0.479$$

Now, from Equation 2, stress can be derived as Equation 11:

$$\sigma_{\theta} = \frac{M_o(A - rA_m)}{Ar(RA_m - A)}$$

$$\sigma_{\theta} = \frac{M_o(\pi a^2 - r2\pi a(2 - \sqrt{3}))}{\pi a^2 r(2a - 2\pi a(2 - \sqrt{3}) - \pi a^2)}$$

$$\sigma_{\theta} = \frac{M_o(\pi a - r2\pi(2 - \sqrt{3}))}{\pi a^2 r(2a - 2\pi(2 - \sqrt{3}) - \pi a)}$$

$$\sigma_{\theta} = \frac{M_o(a - r2(2 - \sqrt{3}))}{\pi a^2 r(2a - 2(2 - \sqrt{3}) - a)}$$

$$\sigma_{\theta} = \frac{M_o(a - r(4 - 2\sqrt{3}))}{\pi a^2 r(a(8 - 4\sqrt{3}) - a)}$$

$$\sigma_{\theta} = \frac{M_o(a - r(4 - 2\sqrt{3}))}{\pi a^3 r(7 - 4\sqrt{3})}$$

When  $r = a$ , Equation 11 can be derived as Equation 12:

$$\sigma_{\theta} = \frac{M_o(a - a(4 - 2\sqrt{3}))}{\pi a^3 a(7 - 4\sqrt{3})} = \frac{M_o(-3 + 2\sqrt{3})}{\pi a^3(7 - 4\sqrt{3})} \quad (12)$$

When  $r = b = 3a$ , from Equation 11, tangential stress can be derived as Equation 13:

$$\sigma_{\theta} = \frac{M_o(a - 3a(4 - 2\sqrt{3}))}{\pi a^3 3a(7 - 4\sqrt{3})}$$

$$\sigma_{\theta} = \frac{M_o(1 - 3(4 - 2\sqrt{3}))}{\pi a^3 3(7 - 4\sqrt{3})} \quad (13)$$

$$\sigma_{\theta} = \frac{M_o(1 - 12 + 6\sqrt{3})}{\pi a^3(21 - 12\sqrt{3})}$$

$$\sigma_{\theta} = \frac{M_o(-11 + 6\sqrt{3})}{\pi a^3(21 - 12\sqrt{3})}$$

The ratio of the tangential stress at  $r = b$  and  $r = a$  is defined as  $\gamma$  in Equation 14:

$$\gamma = \frac{(\sigma_{\theta})_{r=b}}{(\sigma_{\theta})_{r=a}}$$

$$\gamma = \frac{M_o(-11 + 6\sqrt{3})}{\pi a^3(21 - 12\sqrt{3})} / \frac{M_o(-3 + 2\sqrt{3})}{\pi a^3(7 - 4\sqrt{3})} \quad (\text{from Equations 12 \& 13}) \quad (14)$$

$$\gamma = \frac{(-11 + 6\sqrt{3})(7 - 4\sqrt{3})}{(21 - 12\sqrt{3})(-3 + 2\sqrt{3})}$$

$$(11) \quad \gamma = (-)0.436$$

## Elasticity Analysis

For the elasticity analysis, two airy functions were taken in order to calculate the tangential ratio.

### Function 1:

Assume a solution to the bihammonic equation,

$$\nabla^4 \Phi = \left( \frac{\partial^2}{\partial r^2} + \frac{1}{r} \frac{\partial}{\partial r} + \frac{1}{r^2} \frac{\partial^2}{\partial \theta^2} \right) \left( \frac{\partial^2}{\partial r^2} + \frac{1}{r} \frac{\partial}{\partial r} + \frac{1}{r^2} \frac{\partial^2}{\partial \theta^2} \right) \Phi = 0$$

where,  $\Phi$  is an airy function, as in Equation 15 (Den Hartog, 1987):

$$\Phi = (a_1 r^3 + a_2 r + a_3 r \log_e r + a_4 r^{-1} + a_{24}) \sin \theta \quad (15)$$

Assuming  $a_{24} = 0$ , Equation 15 can be written as Equation 16:

$$\Phi = (a_1 r^3 \sin \theta + a_2 r \sin \theta + a_3 r \log_e r \sin \theta + a_4 r^{-1} \sin \theta) \quad (16)$$

Now, radial ( $\sigma_r$ ), tangential ( $\sigma_{\theta}$ ), and shear stress ( $\sigma_{r\theta}$ ), can be written as Equations 17-19:

$$\sigma_r = \frac{1}{r} \frac{\partial \Phi}{\partial r} + \frac{1}{r^2} \frac{\partial^2 \Phi}{\partial \theta^2} \quad (17)$$

$$\sigma_{\theta} = \frac{\partial^2 \Phi}{\partial r^2} \quad (18)$$

$$\sigma_{r\theta} = \frac{-1}{r} \frac{\partial^2 \Phi}{\partial r \partial \theta} + \frac{1}{r^2} \frac{\partial \Phi}{\partial \theta} \quad (19)$$

Using MATLAB and putting the value of  $\Phi$  from Equation 16 into Equations 17-19, radial, tangential, and shear stress can be written as Equations 20-22:

$$\sigma_r = \sin(\theta)(2a_1r^4 + a_3r^2 - 2a_4) / r^3$$

$$\sigma_r = \sin(\theta)(2a_1r + a_3 / r - 2a_4 / r^3) \quad (20)$$

$$\sigma_\theta = \sin(\theta)(6a_1r + a_3 / r + 2a_4 / r^3) \quad (21)$$

$$\sigma_{r\theta} = \cos(\theta)(2a_1r + a_3 / r - 2a_4 / r^3) \quad (22)$$

the boundary conditions for which are,

$$\sigma_r(a, \theta) = \sigma_{r\theta}(a, \theta) = 0$$

$$\sigma_r(b, \theta) = \sigma_{r\theta}(b, \theta) = 0$$

Applying the boundary conditions from Equations 20 and 22, and given that  $\sin(\theta)$  and  $\cos(\theta)$  cannot be zero, where  $\theta$  (degrees) is the angle, the ratio of  $a_3$  and  $a_1$  can be derived as Equations 23 and 24:

When  $r = a$ ,

$$2a_1a + a_3 / a - 2a_4 / a^3 = 0$$

$$2a + a_3 / a_1a - 2a_4 / a_1a^3 = 0$$

$$a_3 / a_1 = 2a_4 / a_1a^2 - 2a^2 \quad (23)$$

When  $r = b$ ,

$$2a_1b + a_3 / b - 2a_4 / b^3 = 0$$

$$2b + a_3 / a_1b - 2a_4 / a_1b^3 = 0$$

$$a_4 / a_1 = -a^2b^2 \quad (\text{from Equation 23})$$

$$a_3 / a_1 = -2a^2 - 2b^2 \quad (24)$$

From Equation 21, tangential stress can be written as Equations 25-27:

$$\sigma_\theta = \sin(\theta)(6a_1r + a_3 / r + 2a_4 / r^3) \quad (25)$$

$$\sigma_\theta = 2a_1 \sin \theta \left( 3r - \frac{a^2 + b^2}{r} - \frac{a^2b^2}{r^3} \right)$$

When  $r = a$  ( $b = 3a$  and using the values of  $a_4$  and  $a_3$ ),

$$(\sigma_\theta)_{r=a} = 2a_1 \sin \theta \left( 3a - \frac{a^2 + 9a^2}{a} - \frac{9a^2a^2}{a^3} \right) \quad (26)$$

When  $r = b$ , ( $b = 3a$  and using the values of  $a_4$  and  $a_3$ ),

$$(\sigma_\theta)_{r=b} = 2a_1 \sin \theta \left( 9a - \frac{a^2 + 9a^2}{3a} - \frac{9a^2a^2}{27a^3} \right) \quad (27)$$

The ratio of the tangential stress at  $r = b$  and  $r = a$  is defined as  $\gamma$  in Equation 28:

$$\gamma = \frac{(\sigma_\theta)_{r=b}}{(\sigma_\theta)_{r=a}}$$

$$\gamma = \frac{\left( 9a - \frac{a^2 + 9a^2}{3a} - \frac{9a^2a^2}{27a^3} \right)}{\left( 3a - \frac{a^2 + 9a^2}{a} - \frac{9a^2a^2}{a^3} \right)} \quad (\text{from Equations 26 \& 27}) \quad (28)$$

$$\gamma = \frac{\left( \frac{16a}{3} \right)}{-16a}$$

$$\gamma = (-)0.330$$

### Function 2:

In this case, the airy function is given as shown in Equation 29 (Budynas, 1977:

$$\Phi = (c_1 + c_2 \ln r + c_3r^2 + c_4r^2 \ln r) \quad (29)$$

Using MATLAB and inserting the value of  $\Phi$  into Equations 17-19, radial, tangential, and shear stress can be written as Equations 30-32, respectively:

$$\sigma_r = \frac{c_2}{r^2} + 2c_3 + 2c_4 \ln r + c_4 \quad (30)$$

$$\sigma_\theta = -\frac{c_2}{r^2} + 2c_3 + 2c_4 \ln r + 3c_4 \quad (31)$$

$$\sigma_{r\theta} = 0 \quad (32)$$

the boundary conditions for which are,

$$\sigma_r(a, \theta) = \sigma_{r\theta}(a, \theta) = 0$$

$$\sigma_r(b, \theta) = \sigma_{r\theta}(b, \theta) = 0$$

Applying these boundary conditions into Equations 30 and 31, coefficients  $c_2$  and  $c_3$  can be written as follows:

$$c_2 = \frac{c_4 \{2a^2 b^2 \ln(b/a)\}}{(b^2 - a^2)}$$

$$c_3 = \frac{c_4 \{a^2(1 + 2\ln a) - b^2(1 + 2\ln b)\}}{2(b^2 - a^2)}$$

Now, from Equation 31, and using these two coefficients, the ratio of the tangential stress at  $r = b$  and  $r = a$  is defined as  $\gamma$  can be derived as Equation 33:

$$\gamma = \frac{\sigma_{\theta,(r=b)}}{\sigma_{\theta,(r=a)}}$$

$$\gamma = \frac{(-2a^2 \ln b + 2a^2 \ln a - a^2 + b^2)}{(-2b^2 \ln b + 2b^2 \ln a - a^2 + b^2)} \quad [\text{as } b = 3a]$$

$$\gamma = \frac{(-2a^2 \ln(3a) + 2a^2 \ln a - a^2 + 9a^2)}{(-18a^2 \ln(3a) + 18a^2 \ln a - a^2 + 9a^2)} \quad (33)$$

$$\gamma = \frac{(-\ln(3a) + \ln a + 4)}{(-9\ln(3a) + 9\ln a + 4)}$$

$$\gamma = (-)0.490$$

## Numerical Analysis

A solid model was created with the Design Modeler of ANSYS to analyze the curved beam numerically then meshed and analyzed in ANSYS Mechanical as an application of ANSYS Workbench (Chavan, & Zhou, 2016). Figures 3-5 show the rectangular, square, and circular cross-section mesh models, respectively. FE analysis results of the rectangular, square, and circular cross-section can be visualized from Figures 6-8, respectively. As the moments were the same from both ends, symmetry analysis was considered by keeping the mid-plane fixed. Meshed and analysis were done for all cases and cross-sections in ANSYS Mechanical Workbench.

## Results and Discussion

Tangential stresses were calculated at  $r = a$  and  $r = b$ . Figure 1 shows the definitions of radii  $a$  and  $b$ . Table 2 shows the results of the ratio of tangential stress at  $r = b$  and tangential stress at  $r = a$ , defined as  $\gamma$  in Equations 6, 10, 14,

28, and 33. The elasticity approach results were slightly different for the curved beam with a square cross-section than for the SOM and FE analyses. In this current study, the authors took two airy functions from the other resources, so the results may vary slightly depending on the airy function. For the rectangular cross-section, the tangential stress ratios were -0.479, -0.490, and -0.426, respectively, for the SOM, EA, and FE analyses. However, the results for the SOM and FE showed only minor differences for all types of cross-sections.

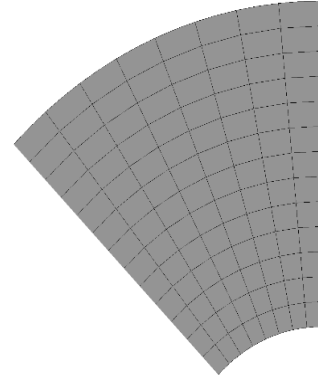


Figure 3. Mesh model of the rectangular cross-section.

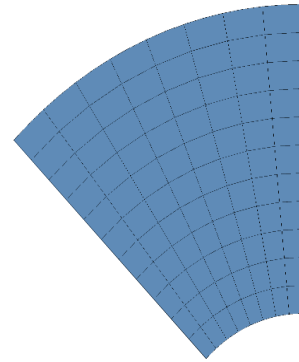


Figure 4. Mesh model of the square cross-section.

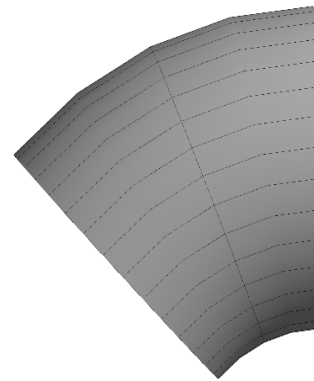


Figure 5. Mesh model of the circular cross-section.

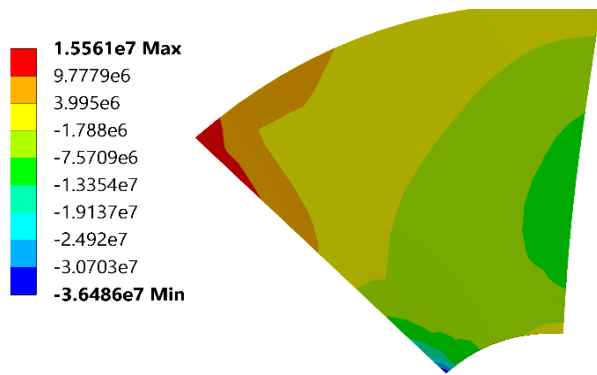


Figure 6. FE analysis results (rectangular).

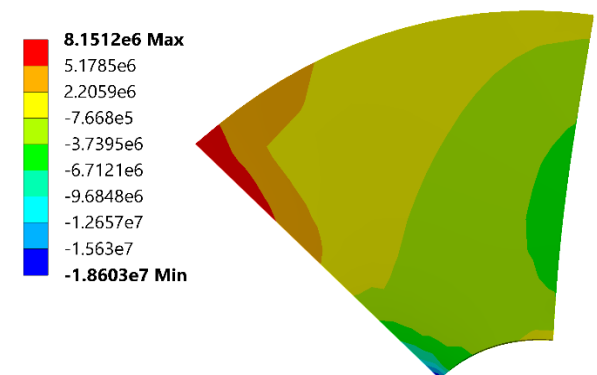


Figure 7. FE analysis results (square).

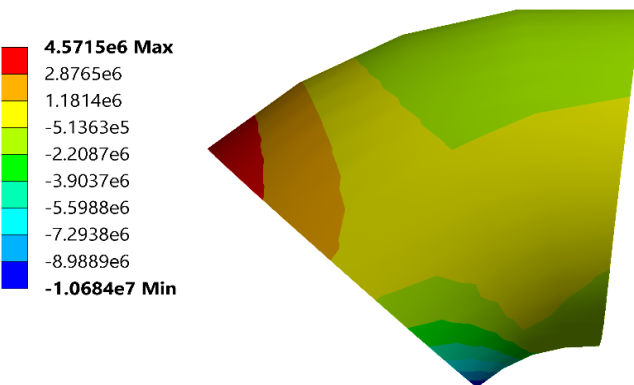


Figure 8. FE analysis results (circular).

Table 2. Comparison of the results.

Cross-section of the curved beams	$\gamma$ , SOM approach	$\gamma$ , elasticity approach	$\gamma$ , FE analysis
Square	-0.479	Function-1 (-0.330)	-0.438
Rectangular	-0.479	Function-2 (-0.490)	-0.426
Circular	-0.436		-0.428

## Conclusions

In this study, the authors compared three ways of calculating the inner and outer surface tangential stress ratios using SOM, EA, and FEA. SOM showed a similar ratio, irrespective of the cross-section, validated by the ANSYS numerical analysis, which showed roughly the same ratio for all the cross-sections—rectangular, square, and circular. However, the EA approach differed slightly for the square cross-section, as it depended on the airy function (Equations 15 and 29). In conclusion, the study showed that the ratio of the tangential stress was similar among approaches and irrespective of the cross-sections of the curved beams. Part of this research was presented at a conference as a poster. As for the material chosen, only one material was considered. In the future, the tangential stress ratio comparison will be compared with new machine learning and image processing (Garfo, Muktadir, & Yi, 2020; Muktadir & Yi, 2021). Also, studies will be done by varying the cross-sections, increasing the inner and outer radius ratios, and increasing the number of mesh for the FE analysis.

## Acknowledgments

This research was awarded funding by the US Department of Education (Award # P120A200056).

## References

- ASTM International. (2019). *ASTM A36 / A36M-19, Standard Specification for Carbon Structural Steel*. <https://www.astm.org/>
- Bagci, C. (1991, September). Exact elasticity solutions for stresses and deflections in curved beams and rings of exponential and T-sections. *International Design Engineering Technical Conferences and Computers and Information in Engineering Conference* (Vol. 7460, pp. 103-115). American Society of Mechanical Engineers.
- Boresi, A. P., Schmidt, R. J., & Sidebottom, O. M. (1985). *Advanced mechanics of materials* (Vol. 6). New York: Wiley.
- Budynas, R. G. (1977). *Advanced strength and applied stress analysis*. McGraw-Hill Science, Engineering & Mathematics.
- Calderón, L., Bohórquez, O., Rojas, M. A., & Pertuz, A. (2021, October). Experimental relationship of tensile strength and hardness of welded structural steel. *Journal of Physics: Conference Series*, 2046(1). 012065. IOP Publishing.
- Chavan, A. P., & Zhou, H. (2016). Analysis and Simulation of Slender Curved Beams. *International Journal of Engineering Research & Technology*, 5(11), 214-221.
- Den Hartog, J. P. (1987). *Advanced strength of materials*. Courier Corporation.
- Garfo, S., Muktadir, M. A., & Yi, S. (2020). Defect Detection on 3D Print Products and in Concrete

- 
- Structures Using Image Processing and Convolution Neural Network. *Journal of Mechatronics and Robotics*, 4(1), 74-84.
- Hasan, M. N. (2018). *Design Study of a Piezoelectric Curved THUNDER via Finite Element Modeling*. (Master dissertation, Southern Illinois University at Edwardsville). Available from ProQuest Central; ProQuest One Academic. (2100695456).
- Ibrahimbegović, A., & Frey, F. (1993). Finite element analysis of linear and non-linear planar deformations of elastic initially curved beams. *International Journal for Numerical Methods in Engineering*, 36(19), 3239-3258.
- Ismail, A. H. (2014). Experimental and analytical study of bending stresses and deflections in curved beam made of Laminated composite material. *Al-Khwarizmi Engineering Journal*, 10(4), 21-32.
- Kılıç, O., & Aktaş, A. (2002). Determination of stress functions of a curved beam subjected to an arbitrarily directed single force at the free end. *Mathematical and Computational Applications*, 7(2), 181-188.
- Lin, K. C., & Lin, C. W. (2011). Finite deformation of 2-D laminated curved beams with variable curvatures. *International Journal of Non-Linear Mechanics*, 46(10), 1293-1304.
- Mathiyazhagan, G., & Vasiraja, N. (2013, April). Finite element analysis on curved beams of various sections. *2013 International Conference on Energy Efficient Technologies for Sustainability* (pp. 168-173). IEEE.
- Muktadir, M. A., & Yi, S. (2021, July). Machine Vision-Based Detection of Surface Defects of 3D-Printed Objects. *2021 ASEE Virtual Annual Conference Content Access*. <https://peerasee.org/37471>
- Subramani, T., Subramani, M., & Prasath, K. (2014). Analysis of three dimensional horizontal reinforced concrete curved beam using Ansys. *International Journal of Engineering Research and Applications*, 4(6), 156-161.
- Wang, M., & Liu, Y. (2013). Elasticity solutions for orthotropic functionally graded curved beams. *European Journal of Mechanics-A/Solids*, 37, 8-16.
- sity. Dr. Akangah's interests include engineering pedagogy, metallic forms for structural and thermal applications, and advanced composites materials. Dr. Akangah may be reached at [pmakanga@ncat.edu](mailto:pmakanga@ncat.edu)
- SUN YI** is a professor of mechanical engineering at North Carolina A&T State University. He has developed new and novel methods for sensing and control algorithms for dynamic systems, which are adaptive and robust. The methods have also been applied to networked robots and UAVs/UGVs using AI, neural networks, sensor fusion, machine visions, and adaptive control. He has managed research projects supported by the Department of Defense, NASA, the Department of Energy, and Department of Transportation. Dr. Yi may be reached at [syi@ncat.edu](mailto:syi@ncat.edu)

## Biographies

**MA MUKTADIR** is a PhD student in mechanical engineering at North Carolina A&T State University. His research interests include robotics, finite element analysis, mechanical design, machine learning, image processing, material science, CFD, and additive manufacturing. Mr. Muktadir may be reached at [mmuktadir@aggies.ncat.edu](mailto:mmuktadir@aggies.ncat.edu)

**PAUL AKANGAH** is a teaching associate professor of mechanical Engineering at the North Carolina A&T State University. He earned his BS degree from Kwame Nkrumah University of Science and Technology, Kumasi, Ghana, MS (energy engineering, 2005) from The Royal Institute of Technology, Stockholm, Sweden, and PhD (mechanical engineering, 2011) from North Carolina A&T State Univer-

# STUDY OF ATMOSPHERIC PLASMA SPRAYING OF FE-BASED MATERIALS FOR OBTAINING WEAR-RESISTANCE COATINGS

Duong Vu, Duy Tan University, Vietnam

## Abstract

Among all of the plasma spray processes, atmospheric plasma spraying (APS) is one of the most progressive, due to its compatibility with a wide range of coating materials and the reasonable cost of consumable gases. Interest in this process is increasing with the substitution of expensive materials by Fe-based materials (blend) and the substitution of inert plasma generation gas by air. Some publications have underlined the importance of correct spraying parameters, such as spray distance, plasma gun power, particle size, particle velocity, substrate roughness, gas flow rate, gas mixture ratio, and so on. But the main shortcoming of these studies was that they did not show the simultaneous correlation between all important spraying parameters, especially the bilateral influence of the process on tribological properties that limited practical application. The aim of this current work was to study the influence of the most critical parameters that determine the quality of the antifriction coating in terms of Fe-based materials. The results of the study are presented in empirical formulas, including all main spraying parameters and the evaluation of the tribological properties in comparison with traditional materials.

## Introduction

The atmospheric plasma spray (APS) process has been used since the beginning of the 1960s (Fauchais, Vardelle, & Goutier, 2017). The APS is performed under atmospheric conditions in a spray booth with an exhaust system to avoid emissions (Kogelschatz, 2004; Clair, Christelle, Pascal, Jean, & Philippe, 2006; Jinheng, Na, Ya-Zhe, Chaoping, & Yongnan, 2019). Spray material must be powdery and flow easily. APS has advantages over other alternatives, due to its good mechanical properties and wear resistance. Table 1 shows the wide range of industrial applications of APS. Fe-based coatings by APS are getting attention, owing to their attractive mechanical, chemical, and thermal properties. Therefore, there have been many recent studies on this theme. In relation to Fe-based coating by APS concerning the effect of arc power on the wear resistance, it was found that as arc power increased, the percentage of porosity decreased (Jinheng et al., 2019). However, the range of power in this current study was limited to 30, 35, and 40 kW. The porosity of the coatings for the corresponding powers were 7.96%, 6.13%, and 5.75%, respectively. Fe-based coatings by high velocity oxygen fuel (HVOF) was investigated for automotive application (Priyan & Hariharan, 2014).

Table 1. Applications of APS in different industries.

N	Area of industry	Application
1	Construction	Construction materials (Thirumalaikumarasamy, Shanmugam, & Balasubramanian, 2014)
2	Energy	Gas turbine & airframe components (Emine & Robert, 2017)
3	Aerospace	Aerospace system (Koutsomichalis, Vaxevanidis, Petropoulos, Xatzaki, Mourlas, & Antoniou, 2009)
4	Automotive	Light-weight engine blocks (Vencl, 2011)
5	Biomedical	Cancer treatment (Alisa, Dayun, Qihui, Andrea, Khyati, Jonathan, & Michael, 2020)
6	Pulp, paper machinery	Center press roll, Yankee dryer roll, cutting equipment (Mitchell & Atin, 2013)
7	Textile industry	Cleaning, roller, tread guides (Andrea, Fernando, & Antonio, 2014)
8	Renewable energy	Incineration boiler, wind turbine (Samantha, 2015)
9	Oil & gas industry	Compressor, pipe, valve (Canan & Yuk-Chiu, 2013)
10	Shipbuilding (marine)	Transition duct, rotary airfoil, combustor (Canan & Yuk-Chiu, 2013)

The Fe-based coating for the tribo-corrosion application has been studied in depth (Muhammad, Cheng, Wei, Zhi-Wei, & Lin, 2016; Koga, Schulz, Savoie, Nascimento, Bolfarini, Kiminami, & Botta, 2017), but the spraying can also be done by the HVOF system. Fe-based amorphous coatings are attractive materials for wear-resistance applications in oil and gas and marine and ship industries (Ma et al., 2016). However, there is a need for more investigation on Fe-based coatings by APS in a range of powers exceeding 40kW, especially when plasma generation gas is the air. There are many macroscopic parameters that have an influence on the quality of the plasma spray coating. Spray-coating characteristics are dependent on feedstock powder properties, substrate surface state, and spray parameters. Many researchers consider that the adhesion bond strength primarily determines the quality of a coating, while the cohesion bond strength influences the life of the coating (Ekrem & Fatih, 2012; Ajit & Mishra, 2012; Jiri, Monika, Radek, Pavel, & Jakub, 2013; Abdul, Nor, SaImiah, & Juri, 2012).

Given the influence the spraying parameters have on coating quality, it is useful to discuss them in more detail. In a study by Mohamed, Soha, Madha, and Khalid (2012), the authors considered that the most common control parameters were: chemical composition, phase structure and size of the powder input, substrate temperature, plasma gas, plasma torch, powder feeder rate, spray angle, and spray distance. But there is a lack of investigation on analysis of the influence of the main parameters on the adhesion bond strength. The important information to take from this work is that the plasma current plays a very important role in increasing the particle velocity as well as the particle surface temperature. Once again, Biswajit et al. (2018) reported a similar result: main plasma spraying operating parameters have a great influence on the deposition. They concluded that the plasma gun power plays a significant role in plasma current. In a more recent study, Odhiambo, Li, Zhao, Li, and Li (2020) found that samples sprayed under higher current had better adhesive bond strength and erosion wear resistance. They also had the lowest wear loss and percentage of porosity.

Additionally, hardness of the base materials was improved almost 10 times in comparison to the lower current samples. It would be better if they had a formula to show their quantitative relation. Jeehoon, Byoungchul, and Sunghak (2005) suggested four types of spraying materials to improve wear resistance, but obviously they are expensive ones. Jinheng et al. (2019) showed some innovation with experiments in which Fe-based amorphous powder was used as the spraying feedstock, and atmospheric plasma spraying (APS) system was used to deposit the Fe-based alloy coating. The microstructure, wear behavior, and high-temperature oxidation resistances of Fe-based amorphous coatings were investigated with samples deposited under different arc powers. In their experiments, the spraying power was varied while keeping all remaining parameters constant. In this current study, the author focused on the simultaneous correlation between all important spraying parameters, in case of Fe-based powder and plasma generation gas is the air, especially the bilateral influence of the process on tribological properties that limited the practical application. The results of the study are presented here in empirical formulas, including all main spraying parameters and the evaluation of the tribological properties in comparison with the traditional materials.

## Experiments

APS was utilized in the current experiment (SG-100 TAFE-Praxair, US). The primary gas was air and the carrier gas was nitrogen. The author assumed that the velocity of the particles and the temperature would have a strong influence on the coating quality, as recent publications indicated (Once, 2015; Tejero-Martin, Rezvani Rad, McDonald, & Hussain, 2019; Lima, Trevixan, 1999). To measure the velocity of spraying particles, a special high-speed camera, Shimadzu HPV-1, was used (Buchmann, Cierpka, Kahler, & Soria, 2014). The average mass temperature of a plasma jet was evaluated indirectly by enthalpy. The wear resistance was evaluated via the pin-on-disk test, using UMT-CETR (US) equipment, according to ASTM G133 standard (with the load on pin of 5MPa), the average speed of the disk was 420 rpm, the duration of the test was five hours, and the lubrication mode dropped. All test data were calculated using the least squares method. Particle size of the powder was analyzed by a Cilas-1090 device. The substrate was 1020 steel. The phase's composition analysis of powder and spraying coating was conducted on a diffractometer by X-ray diffraction (XRD, X-RAY D 5005/SIEMENS, Germany) at a temperature of 25°C with Cu-K $\alpha$  radiation, 2 $\theta$  angle scanning from 10° to 70°. The surface morphology of the coating and the topography of the metallic particles was analyzed using an SEM coupled with energy dispersive spectroscopy (SM-6510 LV, Japan). The content of oxygen in the coating was also investigated using a high-end melt extraction analyzer (G8 Galileo, Germany). The chemical composition of some Fe-based powders was analyzed by energy dispersive spectroscopy with an SEM, SM-6510 LV, Japan. Table 2 shows the experimental data. The composite powders were mechanically mixed for 10 hours in order to obtain a uniform composite powder blend. Table 3 shows the fraction composition of the powders.

Table 2. Chemical composition of powder, % by weight. Note that the content of Fe in blends is the balance.

Code	C	Cr	B	Mo	Ni	Mn	Si	Nb	V	W
H-4	0.11	32.9	0.10	3.30	5.0	1.05	0.70	-	-	-
H-10	0.06	35.3	0.40	3.50	10.5	1.05	0.91	-	-	-
B-5	0.41	12.5	-	0.70	-	0.54	0.66	0.73	0.35	6.10
X-5	0.73	5.0	0.25	4.20	-	1.25	0.84	0.54	1.20	-

Table 3. Distribution of article upon size.

Code	Mean diameter $\mu\text{m}$	Content of articles upon size fraction, %										
		0-1	1-1.5	1.5-2	2-16	16-24	24-32	32-48	48-64	64-96	96-128	128-192
H-4	53.9	7.7	18.9	14.1	-	-	-	-	24.9	24.7	3.2	6.1
H-10	69.2	-	10.4	16.5	-	-	-	-	16.3	40.8	3.1	12.6
B-5	66.4	-	14.0	21.5	-	-	-	-	11.6	35.5	4.0	13.1
X-5	72.5	0.9	0.2	0.6	0.5	-	-	14.5	4.5	43.4	5.0	13.8

## Results and Discussion

### Case study I:

Plasma generation gas was air. The range of powder size was 40-100  $\mu\text{m}$ . There were two versions:

1. Current I = 120 A, voltage U = 200 V, flow rate of air G = 1.19 g/s
2. Current I = 180 A, voltage U = 190 V, flow rate of air G = 1.25 g/s.

In both modes of spraying, the spraying distance was kept at L = 120 mm. Table 4 presents the hardness of the spraying coating before and after heat treatment of the coatings, measured in accordance with ISO 6507-2 using FM-100 hardness measuring device (Japan). It can be seen that the hardness after heat treatment was higher than before heat treatment. The reason was that the amorphous phase was partially transformed into a nanocrystalline structure that could disperse in the coating in order to strengthen it. Another reason could be that, when the annealing temperature was 650°C, the rich-Cr, Mo phase formed in the coating, which played the role of solid solution strengthening. Due to fact that the spraying was done in air, it was useful to analyze the content of the oxygen of the powder (before spraying) and coating (after spraying). Table 5 shows these results.

As can be seen from Table 5, the content of oxygen in the coating increased but, for the wear resistance, this had a bilateral effect. In comparison with HVOF spraying, the content of the oxygen in the coatings by APS was 3-4 times higher (Koga et al., 2017), due to the fact that the plasma generation gas was air and the particle velocity in APS was less than in HVOF deposition. But on the other side, the presence of oxide of iron in the coating decreased the hardness and helped to improve the wear resistance of this coating. From four types of powders, two (H-10 and X-5) were selected to evaluate the mechanical property. Table 6 shows the relative wear resistance. From Table 6, in a similar deposition's conditions, hardness of blend H-10 was less than that of blend X-5. Thus, the wear resistance of the X-5 blend was better.

Table 4. Coating hardness before and after heat treatment.

Code	Version	Hardness before the heat treatment, H R C	Heat treatment	Hardness after the heat treatment, H R C
H-4	1	42-43	-	-
	2	33-35	4 hours 800°C	53-56
B-5	1	28-30	4 hours 540°C	37-45
	2	29-31	4 hours 540°C	37-48
H-10	1	39-41	4 hours 800°C	40-45
	2	40-43	4 hours 800°C	46-49
X-5	1	40-42	4 hours 800°C	43-45
	2	41-45	4 hours 800°C	54-56

Table 5. Content of oxygen in powder and in coating.

Code	Version	Content of the oxygen (%)	
		in powder before spraying	in coating after spraying
H-4	1	0.19	1.70
	2	0.19	1.14
B-5	1	0.30	1.33
	2	0.30	0.07
H-10	1	0.18	1.24
	2	0.18	0.90
X-5	1	0.14	2.15
	2	0.14	1.60

Table 6. Modes of spraying and results of wear resistance.

Code	Current (A)	Voltage (V)	Distance (mm)	Hardness (H R C)	Wear resistance in relative units	
					Volume of wear	Volume of cavity indentation
H-10	120	220	120	40-45	Out of scale	Out of scale
H-10	220	240	120	38-45	Out of scale	Out of scale
H-10	200	200	120	40-42	Out of scale	Out of scale
X-5	120	200	120	48-54	738	116.4
X-5	220	248	120	50-54	752	123.4
X-5	200	200	120	45-49	731	112.9

Table 7. Results from wear resistance tests on some compositions of materials.

Material of friction couple coating-substrate (Disk)	Average coefficient of friction	Character of working surface in sample and disk
(NiAl) + (NiCrBSi) / Al alloy	0.026	Uniform wear on whole surface
X-5 / Al alloy	0.075	Uniform wear on whole surface
X-5 +15% wear resistance alloy/ Al alloy	0.086	Linear wear 0.1 mm
X-5 + 30% wear resistance alloy/ Al alloy	0.064	Linear wear 0.1 mm
X-5 + 15% soft alloy / Al alloy	0.032	10% surface wear
X-5 + 30% soft alloy / Al alloy	0.048	55% surface wear
Cast iron / Al alloy	0.073	Linear wear 0.4 mm
Cast iron + 15% wear resistance alloy/ Al alloy	0.032	N/A
X-5 + 10% graphite / Al alloy	0.032	Linear wear 0.3 mm
X-5 +20% carbon / Al alloy	0.031	N/A

Thus, as observed from Table 6, the higher the plasma power, the higher the wear resistance of the coating. The reason for this is that an increase in power affects the acceleration of particles (powder) and the temperature of the jet. Finally, the density of the coating and the adhesion was increased. But up to threshold number 5, the wear resistance began to go down, which caused the content of the oxide in the coating to increase. From one hand, this content had a positive effect on the hardness; on the other hand, it decreased the wear resistance. For comparison, a set of depositions was done with powder X-5 and other powders. Table 7 shows the data of the coefficient of friction and the character of surface. Adding about 10-15% soft alloy or graphite to blend with the X-5 powder helped to reduce the coefficient of friction on the same order as traditional antifriction material (Ni Al / self-flux alloy).

#### Case study II:

Influence of the main parameters on the velocity of the particles. Code of powder: X-5; size of particle: 40-100  $\mu\text{m}$ ; variation of plasma power:

- 1) x - current I = 120 A
- 2) o - current I = 150 A
- 3)  $\Delta$  - current I = 180 A
- 4)  $\square$  - current I = 200 A
- 5)  $\blacklozenge$  - current I = 220 A

where, I is the current and G is the flow rate of the air.

Figure 1 shows the influence of air flow and current on particle velocity. The velocity of the particles increased as the current and flow increased. The velocity of the particles can be determined using the empirical formula of Equation 1. This formula is derived from the processing data using the least squares method and computer software. Almost the same range of spraying parameters was used for the other blend, 85% Ni + 25% Al, but it is recommended that Equation 2 be used to determine the velocity of the particles:

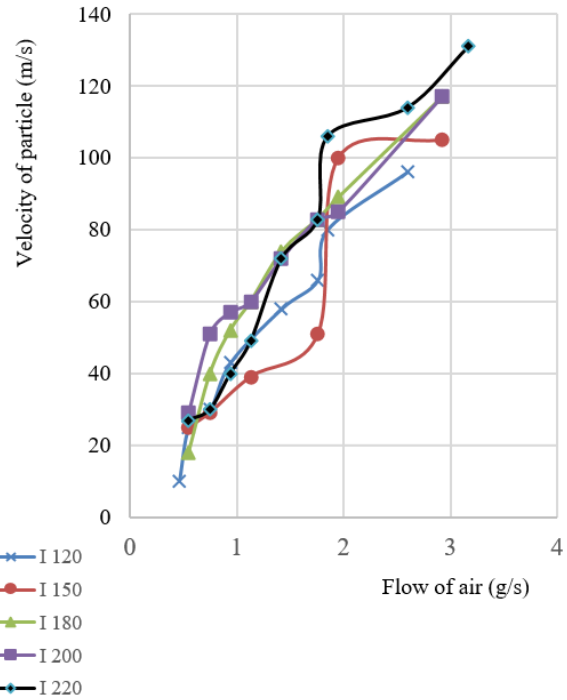


Figure 1. Influence of air flow in variation of plasma power on velocity.

$$V = 11.I^{0.3}.G^{0.9} \quad (1)$$

$$V = 27.I^{0.1}.G^{0.7} \quad (2)$$

The difference between the coefficients and exponents is likely due to the different physical properties of the feed-stock powders. Particle velocity is one of the main parameters for obtaining adhesion strength, thus it is useful to note that for the preliminary design of the Fe-based coatings, these formulas can be applied, in correlation of the current and the flow rate of the air. It will appear in the formula of calculating the adhesion strength in case study IV.

#### Case study III:

Code of powder: X-5; size of particle: 40 -100  $\mu\text{m}$ ; power of plasma was doubled to about 80 kW.

Table 8 shows the results of the measurement of velocity and spraying parameters, while Figure 2 demonstrates that the intensive mode strongly affects particle velocity, due to an increase in plasma power (see case study II). The maxi-

imum velocity could be reached at approximately 180 m/s. The higher the power, the higher the particle velocity. The particle velocity contributed to kinetic energy in impact (collision) on the substrate and increased the adhesion bond. Its contribution will be specified in case study IV. The reason of choosing only powder X-5 was due to the fact that the content of the Fe reached a maximum value of 85%, which exceeded that from any other commercial brand (Ma et al., 2016).

Table 8. Intensive mode of spaying of powder X-5 and velocity of the particles.

Current (A)	Voltage (V)	Flow of air (g/s)	Velocity of particle (m/s)
240	260	1.94	117
240	294	2.52	144
240	310	2.75	142
240	315	2.85	153
240	325	3.25	166
240	330	3.28	177

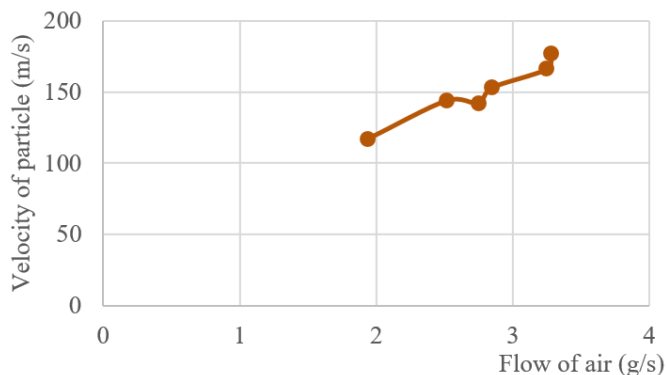


Figure 2. The intensive mode illustration of Table 8.

Case study IV:

Influence of plasma power and the flow rate of the air on the enthalpy ( $\Delta H$ ) in Figure 3. The interval of the variation of the flow rate was 0.5 g/s in the range of 0.5 ÷ 3 g/s. Powder X-5:

- 1) x – current I = 120 A
- 2) ♦ - current I = 180 A
- 3) o – current I = 220 A

The increase of the flow rate of air increased the enthalpy just until the defined value, since, after this limit, the particle was less heated and the results indicated a decrease of the enthalpy.

Case study V:

The adhesion bond of the coatings on the steel substrate was determined by using the universal compression testing machine (Model HT- 2101 A-300, Taiwan), according to the ASTM C 633 standard. The feedstock powder brand was X-5. Figure 4 shows the results of measuring the adhesion bond and particle velocity.

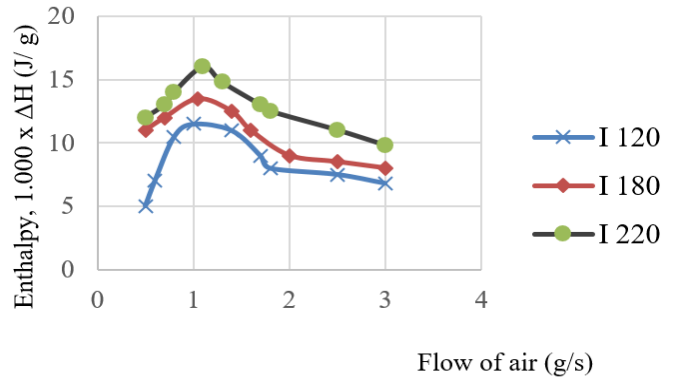


Figure 3. Influence of power and flow rate on the enthalpy

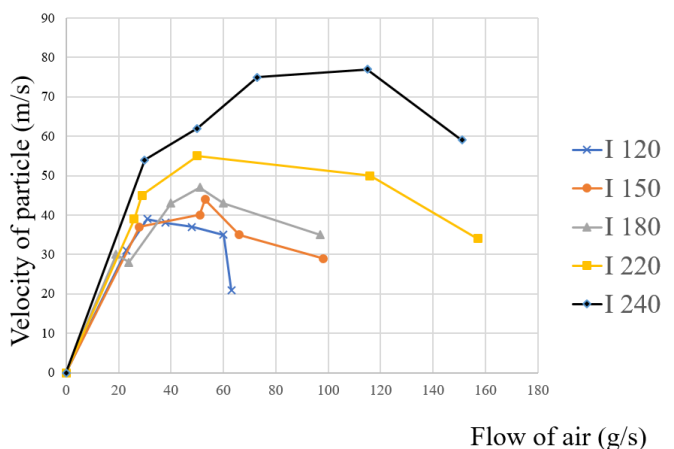


Figure 4. Relationship between adhesion bond and particle velocity in variation of feedstock power (powder X-5).

Figure 4 shows that there was a small difference in adhesion bonds for the range of low velocities (less than 40 m/s); above this range, however, stronger adhesion bonds slowed down (in the case of I = 120 A). This value of adhesion bond was a softer slope (in the case of I = 240 A). However, in this intensive case, the adhesion bond approached a value of 80 MPa, which exceeded the maximum limit noted in recent publications (Ville, Heli, Andrea, & Petri, 2015). The second tendency in changes in adhesion bonding was that, along with the plasma power increasing, their maximums (pick) were shifting toward higher velocities. As a result of analyzing the data, the author is able to present the empirical formula—Equation 3—for representing the simultaneous influence of the three main factors (velocity, temperature, and power via a current) on adhesion strength:

$$\sigma = \frac{1}{V^{x_1} \cdot \Delta H^{x_2} \cdot I^{x_3} \cdot x_4 + V^{x_5} \cdot \Delta H^{x_6} \cdot I^{x_7} \cdot X_8} \quad (3)$$

where,  $x_1 = -1.454$ ,  $x_2 = 0.926$ ,  $x_3 = -0.398$ ,  $x_4 = 0.003$ ,  $x_5 = 0.836$ ,  $x_6 = -1.182$ ,  $x_7 = -0.9$ ,  $x_8 = 3598$ , and where velocity is in V [m/s], enthalpy is in  $\Delta H$  [J/g], and adhesion bond is in MPa.

A more simplified formula for calculation of the adhesion bond is shown as Equation 4:

$$\sigma = V^{x_1} \cdot \Delta H^{x_2} \cdot I^{x_3} \cdot x_4 \quad (4)$$

where,  $x_1 = 0.023$ ,  $x_2 = 0.97$ ,  $x_3 = 0.089$ , and  $x_4 = 0.003$ .

Obviously, in practice, it would better to use Equation 5, as it shows the relationship between the adhesion bond and the current and the flow of air:

$$\sigma = I^{x_1} \cdot G^{x_2} \cdot \exp(x_3 / G) \cdot x_4 \quad (5)$$

where,  $\sigma$  is the adhesion bond [MPa],  $I$  is current [A],  $G$  is flow rate of air [g/s]; also, the values of  $x$  are  $x_1 = 0.6362$ ,  $x_2 = -1.9692$ ,  $x_3 = -1.8503$ , and  $x_4 = 11.5676$ .

Equation 5 is well-suited for applications in the range of currents between 120 and 220 A. By varying the current and the flow rate of the air, it can be expected to reach a good adhesion bond, which is one of the main qualities for the criteria of the coating.

## Conclusions

1. One can apply the APS using air as the plasma generation gas to deposit Fe-based powder with optimal parameters in order to restrain the minimum content of oxide, which saves costs during deposition.
2. For the spraying material, Fe-based is the favorable substitution for the more expensive traditional materials. It also provides reasonable wear resistance.
3. When velocities reach 200 m/s, which is the case for almost all arc plasma jets, the authors developed empirical formulas for evaluating the adhesion bond (see again Equations 3-5). These formulas help in the design of the plasma torch and prediction of the adhesion bond, given the technological parameters of the spraying process.
4. In the future, the development of coatings will be successfully applied in a high-wear resistance environment, making them good candidates for the integration of self-lubrication.
5. In practice, by choosing an optimal set of spraying parameters, one can obtain both wear resistance and adhesion bond strength in the APS coatings from Fe-based materials, especially in an environment of air.
6. In the future, it will be useful to continue the study of the evaluation of partial contribution of the temperature

and the velocity of the particle in adhesion bonding and cohesion strength in the coating. Particle velocity can be increased by the innovative construction of plasma torch in terms of a supersonic jet. At the same time, these main parameters can be increased by changing the diameter and the length of the torch channel to increase the power of the plasma jet. The author expects to be able to present results in this direction in future publications.

## References

- Abdul, R. M. S., Nor, H. S., Salmiah, K., & Juri, S. (2012). Impact of Plasma Spray Variables Parameters on Mechanical and Wear Behaviour of Plasma Sprayed Al<sub>2</sub>O<sub>3</sub> 3% wt TiO<sub>2</sub> Coating in Abrasion and Erosion Application. *Procedia Engineering*, 41, 1689-1695. doi: 10.1016/j.proeng.2012.07.369
- Ajit, B., & Mishra, S. C. (2012). Dependence of Adhesion Strength of Plasma Spray on Coating Surface Properties. *Journal of Materials & Metallurgical Engineering*, 2(1), 23-30. ISSN: 2231-3818.
- Alisa, M., Dayun, Y., Qihui, W., Andrea, L. K., Khyati, C. P., Jonathan, H. S., & Michael, K. (2020). Cold Atmospheric Plasma Cancer Treatment, direct versus indirect approaches. *Material Advances*, 1(6), 1494-1505. The Royal Society of Chemistry. ISSN: 2633-5409.
- Andrea, Z., Fernando, R. O., & Antonio, P. S. (2014). Plasma Treatment in Textile Industry. *Plasma Processes & Polymers* 12(2), 98-131. Doi :10.1002/ p p a p .201400052.
- Biswajit, K. S., Soumya, S. M., Ashutosh, P., Sumant, K. S., Subrat, K. B., Kasinatha, B. ... Ajit, B. (2018). Sensitivity of Process Parameters in Atmospheric Plasma Spray Coating. *Journal of Thermal Spray and Engineering*, 1 (1), 1-6. Science IN.
- Buchmann, N. A., Cierpka, C., Kahler, C. J., & Soria, J. (2014). Ultra-High-Speed 3D Astigmatic Particle Tracking Velocimetry: application to particle laden supersonic impinging jets. *Experiment in fluids*, 55(11), 1-13. Doi 10.1007/s 00348-014-1842-1
- Canan, U. H., & Yuk-Chiu, L. (2013). Advances in Thermal Spray Coatings for Gas Turbines and Energy Generation: A Review. *Journal of Thermal Spray Technology*, 22(5), 564-576. DOI: 10.1007/ s 11666-013-9904-0
- Clair, T., Christelle, T., Pascal, T., Jean, D., & Philippe, L. (2006). Atmospheric pressure plasmas: A review. *Spectrochimica Acta Part B: Atomic Spectroscopy*, 61(1), 2-30. Doi:10.1016/j.sab.2005.10.003
- Ekrem, A., & Fatih, U. (2012). Adhesion Properties of the Plasma Spraying Coatings. EU, Czech Republic, Bmo. *Metal2012*. tanger.cz>files>proceedings>reports
- Emine, B., & Robert, V. (2017). Ceramic Top Coats of Plasma Sprayed Thermal Barrier Coatings: Materials, Processes, and Properties. *Journal of Thermal Spray Technology*, 26, 992-1010. DOI 10.1007/ s 11666 - 017 -0597-7

- Fauchais, P., Vardelle, M., & Goutier, S. (2017). Atmospheric Plasma Spraying Evolution Since the Sixties Through Modeling, Measurements and Sensors. *Plasma Chemistry and Plasma Processing*, 37, 601-626. Doi: 10.1007/s11090-017-9802-1
- Jeehoon, A., Byoungchul, H., & Sunghak, L. (2005). Improvement of Wear Resistance of Plasma-Sprayed Molybdenum Blend Coatings. *Journal of Thermal Spray Technology*, 14(2), 251-257. Doi :10.1361/10599630523827
- Jinheng, L., Na, S., Ya-Zhe, X., Chaoping, J., & Yongnan, C. (2019). The Effect of Arc Power on the Wear and High-temperature Oxidation Resistances of Plasma-Sprayed Fe-based Amorphous Coatings. *High Temperature Materials and Processes*, 38, 639-646.
- Jiri, M., Monika, V., Radek, M., Pavel, S., & Jakub, H. (2013). An Influence of Interface Characteristics on the Adhesion/Cohesion of Plasma Sprayed Tungsten Coatings. *Coatings*, 3, 108-125. doi :10.3390/coatings3020108
- Koga, G. Y., Schulz, R., Savoie, S., Nascimento, A. R. C., Bolfarini, C., Kiminami, C. S., & Botta, W. J. (2017). Microstructure and wear behaviour of Fe-based amorphous HVOF coatings produced from commercial precursors. *Surface & Coating Technology*, 309, 938-944. Doi: 10.1016/j.surfcoat.2016.10.057
- Kogelschatz, U. (2004). Atmospheric - pressure plasma technology. *Plasma Physics and Controlled Fusion*. 46 (12B), B63. Doi :10.1088/0741-3335/46(12 B)/006
- Koutsomichalis, A., Vaxevanidis, N., Petropoulos, G., Xatzaki, E., Mourlas, A., & Antoniou, S. (2009). The Tribological Coatings for Aerospace Applications and the Case of WC-Co Plasma Spray Coatings. *Tribology in Industry*, 31(1&2), 37-42.
- Lima, C. R. C., & Trevisan, R. E. (1999). Temperature Measurement and Adhesion Properties of Plasma Sprayed Thermal Barrier Coatings. *Journal of Thermal Spray Technology*, 8(2), 323-327. ASM International.
- Ma, H. R., Chen, X. Y., Li, J. W., Chang, C. T., Wang, G., Li, H. ..Li, L. W. (2016). Fe -based amorphous coating with high corrosion and wear resistance. *Surface Engineering*, 33(1), 56-62. DOI: 10.1080/02670844.2016.1176718
- Mitchell, R. D., & Atin, S. (2013). Thermal Spray Technology, 5 A, A S M Handbook. In Robert C. Tucker, Jr. (Ed). *Thermal Spray Application in the Paper Production Industry*. doi.org/10.31399/asmhb.v05a.000574
- Mohamed, S. M., Soha, A. A. E. G., Madha, A. S., & Khalid, F. A. (2012). The Effect of Air Plasma Spray Parameters on Coating Performance in Zirconia- Based Thermal Barrier Coatings. *International Journal of Electrochemical Science*, 7, 2811-2831. [www.electrochemsci.org](http://www.electrochemsci.org)
- Muhammad, Y., Cheng, Z., Wei, W., Zhi-Wei, Z., & Lin, L. (2016). Tribo-corrosion Behavior of Fe-based Amorphous Composite Coating Reinforced by Al<sub>2</sub>O<sub>3</sub> in 3.5% NaCl Solution. *Journal of thermal spray technology*, 25(8), 1554-1560. Doi: 10.1007/s11666-016-0457-x
- Odhiambo, J. G., Li, W., Zhao, Y. T., Li, C.L., & Li, Q. (2020). Influence of plasma spraying current on the microstructural characteristics and tribological behaviour of plasma sprayed Cr<sub>2</sub>O<sub>3</sub> coating. *Boletin de la Sociedad Espanola de Ceramica y Vidrio*, 216, 1-9. <https://doi.org/10.1016/j.bsecv.2020.03.007>
- Once, A. B. (2015). Atmospheric plasma spray process and associated spraying jet. *International Conference on Thermal Spraying*, 77(012008), 35-42.
- Priyan, M. S., & Hariharan, P. (2014). The wear and Corrosion Resistance of Fe Based Coatings by HVOF Sprayed on Grey Cast-Iron for Automotive Application. *Tribology in Industry*, 36(4), 394-405.
- Samantha, W. (2015). Future Development of Thermal Spray Coatings. Types, Designs, Manufacture and Applications. In N. Espallargas (Ed), *Thermal Spray Coating in Renewable Energy Applications* (pp. 241-257). Publisher: Woodhead Publishing. doi.org/10.1016/B978-0-85709-769-9.00010-5
- Tejero-Martin, D., Rezvani Rad, M., McDonald, A., & Hussain, T. (2019). Beyond Traditional Coatings: A Review on Thermal-Sprayed Functional and Smart Coatings. *Journal of thermal spray technology*, 28, 598-644. <https://doi.org/10.1007/s11666-019-00857-1>
- Thirumalakumarasamy, D., Shanmugam, K., & Balasubramanian, V. (2014). Corrosion performance of atmospheric plasma sprayed alumina coatings on A Z31B magnesium alloy under immersion environment. *Journal of Asian Ceramic Societies*, 2(4), 403-415. <https://doi.org/10.1016/j.bsecv.2020.03.007>
- Venci, A. (2011). Optimization of the deposition parameters of thick atmospheric plasma spray coatings. *Proceedings of the 7th International Conference on Tribology (BALKANTRIB '11)*, 275-282.
- Ville, M., Heli, K., Andrea, M., & Petri, V. (2015). Advanced coatings by novel high-kinetic thermal spray processes, Tampere University, Finland, *TIEDE&TEKNIKA Materia 1/2015*, 46-50.

## Biography

**DUONG VU** received his PhD in mechanics from Saint Petersburg University, Russia, in 1993. He is currently the Dean of Mechanical Engineering, Duy Tan University. His interests include mechanical engineering, mechatronics and entrepreneurship, professional starter education, and engineering education. He has also taught courses in strength of materials, materials science and engineering, machine design. Dr. Vu may be reached at [duongvuaustralia@gmail.com](mailto:duongvuaustralia@gmail.com)

# AN IMPROVED METHOD FOR PREDICTING THE RESULTS OF ACCELERATED ENGINE AIR FILTER TESTS BASED ON LIMITED DATA SETS

Kevin M. Hubbard, Missouri State University; Neal Callahan, Missouri State University; Nebil Buyurgan, Missouri State University

## Abstract

Accelerated life tests performed on heavy duty air filters for internal combustion engines are difficult, time consuming, and expensive. In these tests, air filters experience dust loading, which leads to an increased pressure drop across the filter element. In previous work, a method was developed by which to predict the final pressure drop across filter elements, based on limited data sets using polynomial curve fitting techniques. The polynomials employed in the previous study were continuous over the entire time interval of the accelerated filter life test. From this current study, the authors present here an improved method for predicting the outcome of accelerated filter life tests, based on limited data sets. This method used a first-order (linear) curve fit to model pressure drop across the filter element during the first two stages of filter dust loading, and a second-order polynomial to model pressure drop during the final phase of the life of the filter. The methods introduced here resulted in a 4% improvement in final pressure drop prediction, and a 43% reduction in testing time and expense, when compared to previously developed techniques.

## Introduction

Air filters employed for internal combustion vehicle and equipment engines are classified as light duty or heavy duty. Light duty air filters are employed on relatively small engines, which are capable of low output power. These filters typically operate in relatively clean environments with low levels of dust or other particulate matter in the engine intake air. In addition, the volume flow rate of air passing through the filter is relatively small. Heavy duty filters are employed on larger engines, which produce higher levels of output power. These filters often operate in “dirty,” often off-road environments with larger levels of dust and particulate matter present in the air being filtered. The volume flow rate of air passing through these types of filters is large. When filters are initially placed in use, the restriction (pressure drop across the filter element) is small. As the filter is exposed to particulate matter over time, however, the pressure drop across the filter element increases. When the pressure drop across the filter element reaches some maximum value specified by the original equipment manufacturer (OEM), the filter is considered to have reached the end of its useful service life. Typical in-service filter lives are measured in terms of months.

For filter design and quality control purposes, accelerated life tests are often performed. For heavy duty air filters, these tests are performed in accordance with the ISO 5011:2020 Inlet Air Cleaning Equipment for Internal Combustion Engines and Compressors - Performance Testing Standard (International Organization for Standardization, 2020). In this test, months of service life are simulated in a short period of time. The ISO 5011 standard mandates that the filter be subjected to cyclic volume flow rates, typically with ranges between 100% and 20% of the maximum volume flow rate of the filter being tested. In a typical testing cycle, the air filter being tested might be exposed to 100% of maximum volume flow rate for some period of time, followed by 60%, 20%, 80%, 60%, and finally 40% of maximum volume flow rate, each for equal time intervals. Upon completion of the cycle, a new cycle is begun. Figure 1 depicts one filter testing volume flow rate cycle.

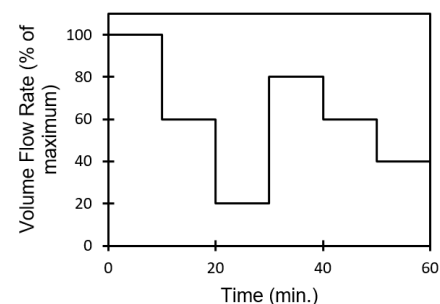


Figure 1. Heavy duty air filter volume flow rate test profile.

During each cycle, standard test dust of known composition and particle size distribution is fed into the air stream upstream of the filter being tested. This test dust is fed at a mass rate that is proportional to the volume flow rate of air passing through the filter element. During the test procedure, the pressure drop across the filter element is monitored. The test is ended when the filter element exhibits some maximum allowable pressure drop, or when some maximum amount of testing time has been reached. The maximum allowable pressure drop is specified by the OEM, and is often set at some value between 20 and 30 in. H<sub>2</sub>O (0.7225 psi to 1.084 psi, or 4.982 kpa to 7.473 kpa). The maximum testing time is also specified by the OEM, and is typically on the order of 20 hours. Even though the maximum testing time is often on the order of 20 hours, heavy duty air filter tests typically require days or even weeks to perform.

The ISO 5011:2020 standard specifies that ambient temperature must remain between 70°F and 90°F (21.2°C to 32.2°C) and ambient relative humidity must remain between 30% and 65%. When these ambient conditions are not met, testing must be halted. The test equipment places a severe load on the climate control systems in the testing facility, particularly in terms of temperature. Volume flow rates across heavy duty air filters are often on the order of 500 ft<sup>3</sup>/min (standard cubic feet per minute, scfm), adjusted to standard sea level conditions (14.7 psia (760 mm Hg) barometric pressure; 80°F (27°C) temperature; standard density of air 0.002268 slug/ft<sup>3</sup> (1.17 kg/m<sup>3</sup>) (International Organization for Standardization, 2020). As a result, the blowers employed in these tests are large and generate large amounts of heat, and the ambient temperature in the testing facility is often exceeded. In addition, noise levels in the testing facility are high, leading to test operator fatigue. Each of these factors necessitates that heavy duty air filter tests be performed in numerous small time intervals. As a result, testing costs are high, often on the order of \$15,000.

Heavy duty air filter testing is employed to perform quality assurance activities using methods, such as statistical process control, to satisfy OEM requirements, and to perform new filter design or existing filter design modification activities. When testing is performed to fulfill OEM requirements, the test is known as a first-article test. First-article tests must be carried out fully, ending only when the pressure drop across the filter element has exceeded the allowable value, or when the maximum testing time has been achieved. When tests are performed for quality assurance purposes, however, testing time reductions and, therefore, cost reductions may be achieved if the results of the heavy duty air filter test may be predicted based on a limited data set obtained by conducting only a portion of the entire test. For the collection of statistical process control data, the actual value of the final pressure drop at the end of the final test cycle is of less importance than the detection of variations in that value.

Filter design parameters having an effect on pressure drop performance include the filter medium composition, the number, size, and distribution of pores in the filter medium, the thickness of the medium, and the geometry (root-to-peak height and peak-to-peak/root-to-root spacing) of the pleats (Joubert, Laborde, Bouilloux, Chazelet, & Thomas, 2011). For new filter design or existing filter design modification efforts, the comparative results between competing designs are of importance in determining the effects of design changes. As a result, a method by which to predict the final result of a heavy duty air filter pressure drop test based on limited data sets is desirable. Previous work has been published with regard to the use of curve-fitting techniques by which the final pressure drop resulting from a heavy duty air filter test may be predicted (Hubbard, Buyurgan, & Jones, 2017). In this current study, the authors employed second- and third-order polynomials for the prediction of

final test results. Test results were predicted with an error (difference between the predicted and measured values) of 1.9692 in. H<sub>2</sub>O. These results were achieved with a 28% reduction in data collection. From this study, the authors present here an improved method for the prediction of the results of heavy duty air filter accelerated life tests based on limited data sets.

## Factors Affecting Air Filter Pressure Drop

Darcy's Law is commonly employed to model the pressure drop across filtration media (Cheng & Tsai, 1998). Darcy's Law is embodied in Equation 1:

$$\Delta P = \Delta P_f + \Delta P_c \quad (1)$$

where,  $\Delta P$  is the total pressure drop across the filter medium and dust cake,  $\Delta P_f$  is the pressure drop across the clean filter medium, and  $\Delta P_c$  is the pressure drop across the dust cake.

The  $\Delta P_f$  and  $\Delta P_c$  terms may be expanded, as in Equations 2-4:

$$\Delta P_f = K_1 V_f \quad (2)$$

$$\Delta P_c = K_2 V_f \frac{M}{A} \quad (3)$$

$$\Delta P = K_1 V_f + K_2 V_f \frac{M}{A} \quad (4)$$

where,  $K_1$  is the filter resistance coefficient,  $K_2$  is the dust cake resistance coefficient,  $V_f$  is the face velocity of air at the point of filter medium entry,  $M$  is the mass of dust deposited on the filter medium, and  $A$  is the area of filter medium exposed to air flow.

The filter resistance coefficient ( $K_1$ ) is a function of filter medium physical characteristics, including pore size and distribution, medium material, and medium thickness. The dust cake resistance coefficient ( $K_2$ ) is a function of the packing efficiency of the dust cake, and dust particle size and distribution. Endo, Chen, and Pui (1998) formulated Equation 5:

$$\Delta P_c = 18 \mu V_f T \frac{(1-\alpha)\{v(\alpha)\}}{\alpha^2} \frac{\kappa}{d_{vg}^2 e^{4 \ln^2 \sigma_g}} \quad (5)$$

where,  $T$  is the thickness of the dust cake,  $\mu$  is the dynamic viscosity of the gas being filtered,  $v(\alpha)$  is the void function,  $\kappa$  is the dynamic shape factor for the dust particles,  $\alpha$  is the average porosity of the dust cake layer,  $d_{vg}$  is the volume equivalent diameter of the dust particles, and  $\sigma_g$  is the standard deviation of the particle equivalent diameter of the dust particles. The dynamic shape factor  $\kappa$  was set to unity for

spherically shaped particles. The void function  $v(\alpha)$  accounts for dust cake agglomeration, and acts as a modifier on the dynamic viscosity  $\mu$  of the gas being filtered.

Employing the formulation of Endo et al. (1998), Darcy's Law may be restated as Equations 6-8:

$$v(\alpha) = \frac{10(1-\alpha)}{\alpha} \quad (6)$$

$$\alpha = 1 - \frac{M}{\rho TA} \quad (7)$$

$$\Delta P = K_1 V_f + 180 \mu V_f T \frac{(1-\alpha)^2}{\alpha^3} \frac{\kappa}{d_{vg}^2 e^{4 \ln^2 \sigma_g}} \quad (8)$$

where,  $\rho$  is the density of the individual dust particles.

In Equation 4, if face velocity is held constant, then the mass of the dust cake ( $M$ ) is the only variable affecting the pressure drop across the dust-loaded filter medium. In Equations 7 and 8, mass is also the only variable affecting the pressure drop across the filter media and dust cake, if face velocity across the filter medium and temperature are held constant. Note that temperature affects the dynamic viscosity ( $\mu$ ) of the fluid passing through the filter medium. The temperature range at which accelerated filter life testing was performed, however, was allowed to vary only to a small extent. If the rate at which dust is fed into the airstream impinging on the filter is known, then the pressure drop across the filter medium may be transformed into a function of time. It is difficult in practice, however, to establish values for many of the factors in Equations 4-8. From this current study, the authors present here a simplified technique for predicting pressure drop as a function of time.

## Experimental Design and Testing

Figure 2 schematically depicts the testing apparatus employed in this study. When the blower was in operation, air entered the system through the ideal flow nozzle. This nozzle provided a gradual, rather than abrupt transition through which air could enter the system, thereby promoting laminar flow. Dust was fed into the air stream by the dust feeder. The dust-carrying air stream entered the filter housing, which contained the filter undergoing testing. After exiting the test filter, the air stream passed through the absolute filter housing. This housing contained an absolute filter media, which collected any test dust that had passed through the test filter. This filter media would be weighed both before and after testing in order to assess the efficiency of the test filter. Flow-rate measuring and control devices were located downstream of the absolute filter housing. Pressure sensors connected to piezometer rings were located upstream of the filter being tested (between the filter housing

and the dust feeder) and downstream of the filter being tested (between the filter housing and the absolute filter housing). These pressure sensors were employed in order to measure the pressure drop across the filter media during testing. Pressure drop across the filter element was also monitored using a water-type U-tube manometer. Ambient conditions were monitored using digital instruments during the test procedure in order to assure compliance with the ISO 5011:2020 standard, and to obtain data with which to convert all measured values to standard sea-level temperature and barometric pressure conditions. Ambient data, as well as pressure and flow rate data were collected and stored using an analog PC-based data acquisition card.

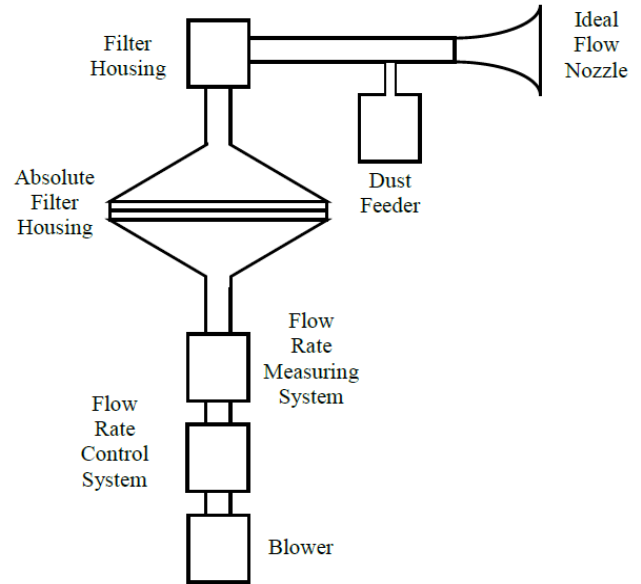


Figure 2. Testing apparatus schematic (Hubbard et al., 2017).

The test dust employed was coarse grade, and was fed at a rate of 0.025 grams per cubic foot of volumetric air flow. The volumetric flow rate of air passing through the system, as well as the dust feed rate, were varied in accordance with the schedule specified in the ISO5011:2020 standard. Each volumetric flow rate was held constant for intervals of 10 minutes, and each complete cycle exhibited a duration of one hour. The test filters described here had a maximum volumetric flow rating of 420 sfc. Table 1 details the volume flow rate and dust feed rate employed during each 10-minute interval.

## Analysis and Results

In previous studies, a single polynomial regression was employed in order to predict the pressure drop across the filter element at the maximum testing time (Hubbard et al., 2017). However, pleated filters, such as the type of filter analyzed in this study, experience three dust loading stages: depth filtration, cake filtration, and a final dust cake build-

up stage (Joubert et al., 2011). In-depth filtration, dust particles impinge on the clean filter medium and penetrate into the pores of that medium. This phase of dust loading occurs in a relatively short time interval. Cake filtration occurs once the pores of the medium have been loaded with dust. During the cake filtration stage of dust loading, a dust cake develops on the surface of the medium. Once the surface of the medium has developed a thin dust cake, the final dust cake build-up stage of dust loading begins. During this stage, newly impinging dust particles cling to previously deposited dust particles (rather than to the medium itself), and the thickness of the dust cake increases with time.

Table 1. Volume flow rate of air and dust feed rates.

Time Period (minutes)	Volumetric flow rate (cubic feet per minute)	Dust feed rate (grams per minute)
0	420	10.5
10	252	6.3
20	84	2.1
30	336	8.4
40	252	6.3
50	168	4.2

During the depth filtration and cake filtration stages of dust loading, pressure drop across the filter medium tends to exhibit a linear relationship with respect to time (Joubert et al., 2011). During the final dust cake build-up stage of dust loading, this relationship tends to become non-linear. Since the depth filtration stage of dust loading is brief, the time-versus-pressure-drop function during the depth filtration and cake filtration stages of dust loading was modeled using a single first-order (linear) polynomial. Data was collected from full first-article tests for eight heavy duty air filters using the testing profile depicted in Figure 1 and detailed numerically in Table 1. Figure 3 graphically depicts the filter restriction data collected during the testing of these eight filters. Note that data for the maximum rated flow rate were collected once per hour, and the test was terminated upon reaching 20 hours of testing time. As a result, data exists for hours 0-19.

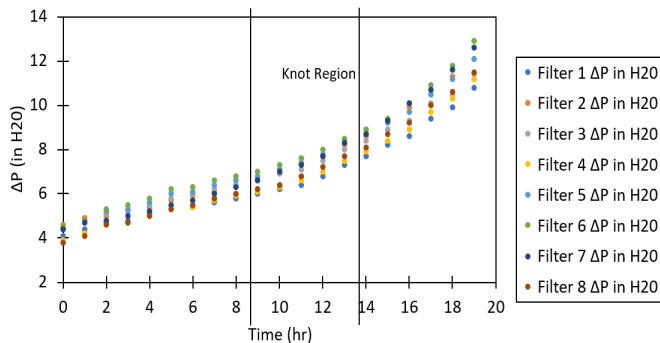


Figure 3. Time versus pressure drop for eight test filters.

A point of intersection exists in the time-versus-pressure-drop curve at the point in time that marks the end of the cake filtration stage of dust loading and the beginning of the final dust cake-build up stage. The point of intersection of two curves described by different functions is known as a “knot” (Coopersmith, 1983). For times less than the time at the point of intersection, the time-versus-pressure-drop curve was essentially linear, and for times greater than the time at the point of intersection the curve was non-linear in nature. An examination of the curves depicted in Figure 3, however, reveals that the location of the knot in each curve is subject to interpretation.

Stress-strain curves obtained from tensile tests of many metallic materials exhibited similar behavior. In the elastic deformation region, these curves were essentially linear, while in the plastic deformation region, these curves became exponential in nature. When the point of transition from elastic to plastic behavior is ambiguous, the offset yield strength is often employed in order to remove ambiguity. This type of method, though, is somewhat arbitrary. Arbitrary methods were initially employed in this study, as well. The results (in terms of the error between the predicted pressure drop value and the actual, measured pressure drop at the end of the test) varied significantly from one filter to another. A less arbitrary method for determining the time and pressure drop value associated with the knot exhibited by the time-versus-pressure-drop curves was developed and is embodied in Equations 9-11:

$$m_{avg} = \frac{\sum_{i=1}^n (\Delta P_i - \Delta P_{i-1})}{n} \quad (9)$$

$$m_i = \Delta P_i - \Delta P_{i-1} \quad (10)$$

$$d = m_{avg} - m_i \quad (11)$$

where,  $m_{avg}$  is the average slope of the time-versus-pressure-drop curve from time zero until the time at which the current data point is being evaluated,  $i$  is the time (hr) associated with the data point at which the curve is being evaluated,  $\Delta P_i$  is the pressure drop value (in. H<sub>2</sub>O) measured at the current time  $i$ ,  $\Delta P_{i-1}$  is the pressure drop value associated with the previous data point,  $m_i$  is the instantaneous slope of the time-versus-pressure-drop curve at time  $i$ , and  $d$  is a value known as the discriminant. The discriminant is the difference between the average slope of the time-versus-pressure-drop curve from time zero until the current time and the slope of the curve between the point being evaluated and the previous data point.

The data depicted in Figure 3 were collected using a analog voltage output pressure transducers, and recorded using a 12-bit analog PC-based data acquisition card. Some electrical and/or radio frequency noise may be expected to be pre-

sent in the signal. The calculation of average slope ( $m_{avg}$ ) was employed in order to reduce the level of noise present in the signal. Averaging is a commonly employed technique for noise rejection in signals (Janajreh, Sajjad, & Janajreh, 2021). This technique is analogous to the use of a low-pass noise filter in signal processing applications (Weyori & Boateng, 2013). As the time-versus-pressure-drop data transition from the linear region into the higher-order polynomial region, the slope of the curve, which was constant in the depth filtration and cake filtration regions, became variable and increased. The discriminant was employed in order to detect this transition. The use of the discriminant is analogous to the use of a high-pass filter. The discriminant was employed in order to reject minor variations between the instantaneous and average slopes of the time-versus-pressure-drop curve, and “pass” large variations between these two values. When the discriminant had achieved a negative value, and one that possessed an absolute value larger than some threshold value, the filter was considered to have entered the final dust cake build-up phase of dust loading. Collectively, the use of averaging for noise rejection in conjunction with the discriminant is analogous to the creation of a bandpass filter in digital signal processing.

Table 2. Time-versus-pressure-drop data, slope, and discriminant results (Filter 1).

Time (hr)	$\Delta P$ (in. H <sub>2</sub> O)	$m_i$	$m_{avg}$	$d$
0	4.1			
1	4.4	0.3		
2	4.7	0.3	0.300	4.4410 <sup>-16</sup>
3	4.8	0.1	0.233	0.133
4	5.1	0.3	0.250	-0.050
5	5.3	0.2	0.240	0.040
6	5.4	0.1	0.217	0.117
7	5.6	0.2	0.214	0.0143
8	5.8	0.2	0.213	0.0125
9	6	0.2	0.211	0.0111
10	6.2	0.2	0.210	0.0100
11	6.4	0.2	0.209	0.009
12	6.8	0.4	0.225	-0.175
13	7.3	0.5	0.246	-0.254
14	7.7	0.4	0.257	-0.143
15	8.2	0.5	0.273	-0.227
16	8.6	0.4	0.281	-0.119
17	9.4	0.8	0.312	-0.488
18	9.9	0.5	0.322	-0.178
19	10.8	0.9	0.353	-0.547

A threshold value of the discriminant of  $d < 0$  was initially employed to determine the transition from the depth/cake filtration phases to the final dust cake buildup phase. This threshold value, however, provided poor results, since some noise remained present in the signal even after averaging techniques for noise reduction were employed. Varying the threshold value of the discriminant had an effect on the error between the predicted and measured values of final pressure drop. For the type of heavy duty air filter evaluated in this study, a threshold discriminant value of -0.1 provided acceptable (small) error values.

As an example, Table 2 details time-versus-pressure-drop data for Filter 1, as well as  $m_{avg}$ ,  $m_i$ , and  $d$  results for each data point. The discriminant value was less than -0.1 at 12 hrs. The knot was placed one time interval prior to that time. As a result, the time at which the knot was encountered was set at a time of 11 hrs. Using this method, the time associated with the knot was evaluated for each of the filters for which test data were analyzed. Table 3 details these results. At times less than or equal to the time associated with the knot, a first-order curve fit was applied to the time-versus-pressure-drop data. Figure 4 depicts the time-versus-pressure-drop curve for a time less than the time associated with the knot for each filter.

Table 3. Filter knot times.

Filter	Time at knot (hr)
1	11
2	11
3	12
4	11
5	12
6	12
7	11
8	10

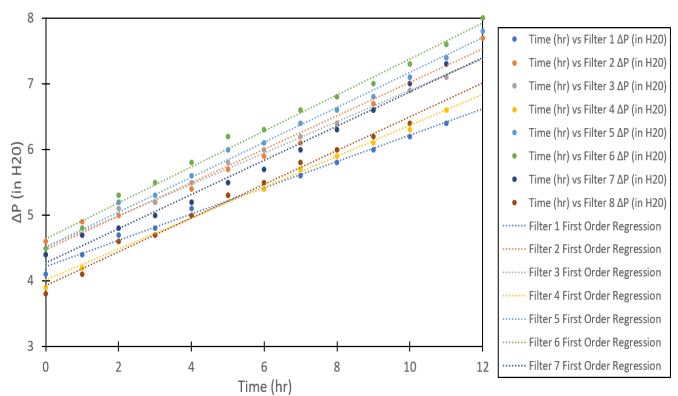


Figure 4. Depth filtration and cake filtration at time-versus-pressure drop.

The first-order curve fit equation has the form of Equation 12:

$$\Delta P_1 = C_0 + C_1 t \quad (12)$$

where,  $C_0$  and  $C_1$  are constant coefficients,  $t$  is time expressed in hours, and  $\Delta P_1$  is pressure drop expressed in in.  $H_2O$ .

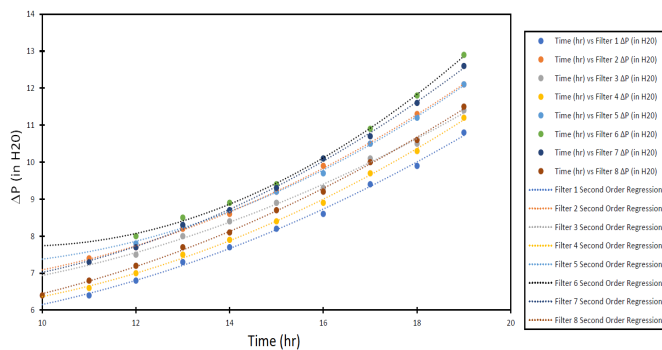
Table 4 details the coefficient of determination ( $r^2$ ) values and coefficient values obtained from first-order curve fits of data taken at times prior to the time associated with the knots for Filters 1 through 8.

Table 4. First-order curve parameters, depth/cake filtration.

Filter	$r^2$	$C_0$	$C_1$
1	0.993631	4.017	0.200
2	0.986673	4.478	0.255
3	0.994258	4.512	0.239
4	0.993622	4.014	0.235
5	0.992442	4.512	0.266
6	0.991625	4.640	0.274
7	0.985907	4.279	0.260
8	0.989731	3.932	0.257

At times greater than the time associated with the knot, second- and third-order curve fits were applied to the data set associated with each filter. Second-order curves exhibited high coefficient-of-determination values. An increase in the order of the curve fit to each data set resulted in only marginal improvement in the  $r^2$  value. As a result, second-order curves were employed to model the data. Figure 5 depicts the second-order curves applied to the data for each filter at times greater than or equal to the time associated with the knot.

Figure 5. Final dust cake build-up time-versus-pressure drop (Filter 1).



The second-order curve fit equation has the form of Equation 13:

$$\Delta P_2 = K_0 + K_1 t + K_2 t^2 \quad (13)$$

where,  $K_0$ ,  $K_1$ , and  $K_2$  are constant coefficients,  $t$  is time expressed in hours, and  $\Delta P_2$  is pressure drop expressed in in.  $H_2O$ .

Table 5 details the coefficient of determination ( $r^2$ ) values and coefficient values obtained from second-order curve fits applied to data taken at times greater than or equal to the time associated with the knots for Filters 1 through 8.

Table 5. Second-order curve parameters, final dust cake build-up.

Filter	$r^2$	$K_0$	$K_1$	$K_2$
1	0.997044	5.968	-0.239	0.0258
2	0.999398	7.377	-0.351	0.0315
3	0.995648	6.918	-0.254	0.0256
4	0.998348	6.873	-0.357	0.0306
5	0.998383	8.347	-0.459	0.0344
6	0.999080	13.021	-1.105	0.0577
7	0.998676	8.013	-0.475	0.0376
8	0.998910	6.003	-0.225	0.0269

Using the general expression for second-order curves embodied in Equation 13, it is possible to derive expressions for the coefficients  $K_0$ ,  $K_1$ , and  $K_2$  in terms of data collected at  $t < t_{knot}$  if one additional boundary condition is applied. As a result, the final value for pressure drop across the filter element may be estimated using data collected only during the depth filtration and cake filtration stages of dust loading in conjunction with one additional boundary condition. As a matching condition, the slope of the depth filtration/cake filtration first-order curve was set equal to the slope of the final dust cake build-up second-order curve at the knot, as in Equation 14:

$$\left. \frac{d\Delta P_1}{dt} \right|_{t=t_{knot}} = \left. \frac{d\Delta P_2}{dt} \right|_{t=t_{knot}} \quad (14)$$

where,  $\Delta P_1$  is the first-order  $\Delta P$  function associated with the depth filtration and cake filtration stages of dust loading,  $\Delta P_2$  is the second-order  $\Delta P$  function associated with the final dust cake build-up stage of dust loading,  $t$  is time expressed in hours, and  $t_{knot}$  is the time at which the cake filtration stage of dust loading ends and the final dust cake build-up stage of dust loading begins.

The first derivatives of the  $\Delta P_1$  and  $\Delta P_2$  functions are presented in Equations 15 and 16, respectively:

$$\left. \frac{d\Delta P_1}{dt} \right|_{t=t_{knot}} = C_1 \quad (15)$$

$$\left. \frac{d\Delta P_2}{dt} \right|_{t=t_{knot}} = K_1 + 2K_2 t_{knot} \quad (16)$$

Setting the right-hand terms in Equations 15 and 16 equal, and solving for  $K_1$ , results in Equation 17:

$$K_1 = C_1 - 2K_2 t_{knot} \quad (17)$$

A second matching condition may be obtained through the observation that the piecewise function described by  $\Delta P_1$  and  $\Delta P_2$  is continuous at  $t = t_{knot}$ . This boundary condition is embodied in Equation 18:

$$\Delta P_1|_{t=t_{knot}} = \Delta P_2|_{t=t_{knot}} \quad (18)$$

Equating Equations 12 and 13 at  $t = t_{knot}$  results in Equation 19:

$$C_0 + C_1 t_{knot} = K_0 + K_1 t_{knot} + K_2 t_{knot}^2 \quad (19)$$

A boundary condition is given by Equation 20:

$$\Delta P_{2\ final} = \Delta P_2|_{t=t_{knot}} + r \quad (20)$$

where,  $\Delta P_{2\ final}$  is the differential pressure drop across the filter element at test termination, and  $r$  is the rise in pressure drop across the filter element between  $t_{knot}$  and test termination. Substituting Equation 13 into Equation 20 results in Equation 21:

$$K_0 + K_1 t_{final} + K_2 t_{final}^2 = \Delta P_2|_{t=t_{knot}} + r \quad (21)$$

Substituting Equation 17 into Equation 19 results in Equation 22:

$$C_0 + C_1 t_{knot} = K_0 + (C_1 - 2K_2 t_{knot}) t_{knot} + K_2 t_{knot}^2$$

$$K_0 = C_0 + K_2 t_{knot}^2 \quad (22)$$

Substituting Equations 22 and 17 into Equation 21 results in Equation 23:

$$C_1 + K_2 t_{knot}^2 + (C_1 - 2K_2 t_{knot}) t_{final} + K_2 t_{final}^2 = \Delta P_2|_{t=t_{knot}} + r \quad (23)$$

Employing the matching condition embodied in Equation 18 in conjunction with Equation 12 results in Equation 24:

$$\Delta P_2|_{t=t_{knot}} = \Delta P_1|_{t=t_{knot}} = C_0 + C_1 t_{knot} \quad (24)$$

Substituting Equation 24 into Equation 23 results in Equation 25:

$$C_1 + K_2 t_{knot}^2 + (C_1 - 2K_2 t_{knot}) t_{final} + K_2 t_{final}^2 = C_0 + C_1 t_{knot} + r \quad (25)$$

Solving Equation 25 for the constant  $K_2$  results in Equation 26:

$$K_2 = \frac{C_1 (t_{knot} - t_{final}) + r}{t_{knot}^2 - 2t_{knot} t_{final} + t_{final}^2} \quad (26)$$

Equations 17 and 22 are repeated here for convenience:

$$K_1 = C_1 - 2K_2 t_{knot} \quad (17)$$

$$K_0 = C_0 + K_2 t_{knot}^2 \quad (22)$$

The slope and intercept of the first-order curve associated with the depth filtration and cake filtration stages of dust loading are provided in Equations 27 and 28:

$$C_1 = \frac{\Delta P_1|_{t=t_{knot}} - \Delta P_1|_{t=0}}{t_{knot}} \quad (27)$$

$$C_0 = \Delta P_1|_{t=0} \quad (28)$$

The constant coefficients  $K_0$  and  $K_1$  depend only on the time at which the knot occurs, the slope of the linear region of the time-versus-pressure-drop curve associated with the depth filtration and cake filtration stages of dust loading ( $C_1$ ), and the constant coefficient  $K_2$ . The constant coefficient  $K_2$  depends on the time at which the knot occurs ( $t_{knot}$ ), the time at which the test is to be terminated ( $t_{final}$ , which is a known quantity), the slope of the linear region of the time-versus-pressure-drop curve, and the rise in differential pressure across the filter element, which occurs between  $t_{knot}$  and  $t_{final}$ .

Table 6 details the values of differential pressure rise ( $r$ ) values for each of the eight filters for which data were collected in this study.

Table 6. Filter rise ( $r$ ) values.

Filter	$r$ (in. H <sub>2</sub> O)
1	4.4
2	4.4
3	3.9
4	4.6
5	4.3
6	4.9
7	5.3
8	5.1

The Shapiro-Wilk test performed on these data results in a  $P$  value of 0.862, where  $P$  is the probability of finding the observed or larger deviation from normality in the sample if the distribution is exactly normal in the population. Typically,  $P$  values resulting from this test and having values larger than 0.05 indicate that there is reason to believe that the data are normally distributed. The standard deviation of these data was 0.461 in. H<sub>2</sub>O. The data detailed in Table 6 exhibits a mean value of 4.6 in. H<sub>2</sub>O and a range of 1.4 in. H<sub>2</sub>O.

Since the rise-value data can be assumed to be normally distributed, 99.73% of all values in the population of rise values for this filter were expected to lie within  $\pm 3\sigma$  of the mean, where  $\sigma$  is the standard deviation of the normal distribution of data. The largest rise value to be expected in the population was  $(4.6 + 3(0.461))$  in. H<sub>2</sub>O = 5.98 in. H<sub>2</sub>O, and the smallest rise value to be expected in the population was  $(4.6 - 3(0.461))$  in. H<sub>2</sub>O = 3.22 in. H<sub>2</sub>O. Table 7 details the greatest and least errors in predicted final pressure drop using these extreme values, as well as those obtained using the mean rise value of 4.60 in. H<sub>2</sub>O. Table 7 also details the error bandwidth between predicted and measured final pressure drop values for each rise value, where error bandwidth was the difference between the greatest and least error obtained by evaluating the predicted and measured final pressure drop values for each of the eight filters for which data were available. Note that a positive error represented an over prediction of final pressure drop, and a negative error value represented an under prediction.

Table 7. Errors and error bandwidths between predicted and measured final pressure drops.

Rise value ( $r$ ) (in. H <sub>2</sub> O)	Greatest error between predicted and measured values (in. H <sub>2</sub> O)	Least error between predicted and measured value (in. H <sub>2</sub> O)	Error bandwidth (in. H <sub>2</sub> O)
5.98	1.58	-2.42	4.00
4.60	0.70	-3.10	3.80
3.22	-1.18	-5.18	4.00

Figure 6 depicts measured and predicted results using  $r = 5.98$  in. H<sub>2</sub>O,  $r = 4.60$  H<sub>2</sub>O, and  $r = 3.22$  H<sub>2</sub>O for Filter 1.

In the previous study, continuous second- and third-order polynomials were employed to predict final pressure drop values (Hubbard et al., 2017). These polynomials were continuous over the interval  $t = 0$  to  $t = t_{final}$ . No reduction in data collection was apparent from the results of the analyses in that study, when pressure drop was measured at the maximum-rated air flow of the filter, third-order polynomials were employed, and a test uncertainty ratio of 4:1 was imposed. When second-order curves were employed to model the time-versus-pressure-drop curve at the maximum rated air flow, error bandwidths of 4.17 in. H<sub>2</sub>O were obtained using 14 hours of data-collection time.

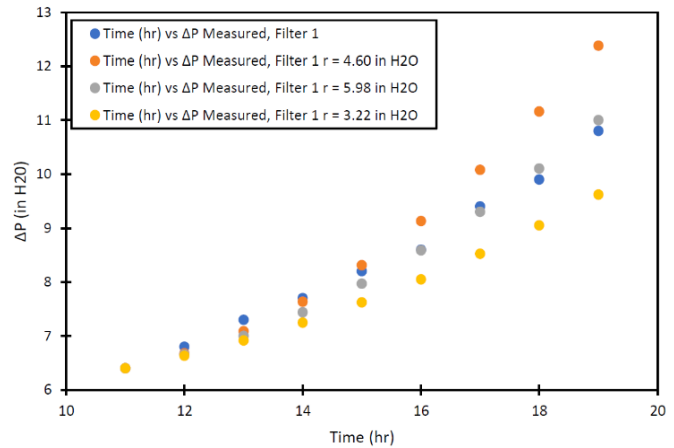


Figure 6. Measured and predicted final pressure drop results.

Employing the methods described here, an error bandwidth improvement of approximately 4% was realized using 11 375 hours of data-collection time, on average. This 4% reduction in error bandwidth was associated with a reduction in data-collection time (and, therefore, testing expense) of 43%, when compared to the previous method (Hubbard et al., 2017). The method developed in this study is acceptable for use in statistical process control analyses. Commonly employed heuristics for use with X-Bar control charts, which monitor the centering of the distribution of data collected from the process, and R-Bar control charts, monitor the dispersion of data (Suman & Prajapati, 2018; Montgomery, 2020).

If error exists between the predicted value of final pressure drop and the “true” value of final pressure drop, these (and other) heuristics employed in statistical process control are not affected. The method described here is suitable for existing filter design optimization and new filter design. After the completion of one entire first-article test, the rise value measured during that test may be employed as modifications are made to the original filter geometry. Since all analyses performed in filter design optimization are comparative, the method described in this paper is valid.

## Conclusions

In this paper, the authors presented an improved method for the prediction of the results of accelerated filter life tests using limited data sets. The methods described here resulted in significant time and cost savings in the performance of these types of tests, as well as an improvement of test prediction results of 4%, when compared to previously developed techniques. In addition, the methods described here resulted in a data-collection savings of 43%, as compared to previously developed methods. Previously developed methods employed polynomial curve fits applied in a continuous manner over the entire testing period. In this current work, a first-order polynomial was employed to model pressure

---

drop across the filter element during the depth filtration and cake filtration phases of dust loading, and a second-order polynomial was employed to model pressure drop during the final dust cake build-up stage of dust loading. Techniques with which to identify the time at which the cake filtration phase ends, and the final dust cake build-up phase begins were described in this paper. In addition, techniques by which to determine the coefficients that characterize the second-order polynomial employed to model the final dust cake build-up stage of dust loading were developed.

## References

- Cheng, Y. H., & Tsai, C. J. (1998). Factors influencing pressure drop through a dust cake during filtration. *Aerosol Science and Technology*, 29(4), 315-328.
- Coopersmith, L. (1983). Forecasting time series which are inherently discontinuous. *Journal of Forecasting*, 2, 225-235.
- Endo, Y., Chen, D. R., & Pui, D. Y. H. (1998). Effects of particle polydispersity and shape factor during dust cake loading on air filters. *Powder Technology*, 98(3), 241-249.
- Hubbard, K. M., Buyurgan N., & Jones, M. P. (2017). A method for predicting the results of accelerated engine air filter tests based on limited data sets. *International Journal of Modern Engineering*, 18(1), 33-39.
- International Organization for Standardization. Inlet air cleaning equipment for internal combustion engines and compressors -- Performance testing. (ISO 5011:2020). <https://www.iso.org/standard/72490.html>
- Janajreh, I., Sajjad, M., & Janajreh, L. (2021). Simulation of human coughing under various flow scenarios and environmental conditions. *International Journal of Modern Engineering*, 21(2), 24-33.
- Joubert, A., Laborde, J. C., Bouilloux, L., Chazelet, S., & Thomas, D. (2011). Modelling the pressure drop across HEPA filters during cake filtration in the presence of humidity. *Chemical Engineering Journal*, 166(2), 616-623.
- Montgomery, D. C. (2019). *Introduction to statistical quality control*. (8th ed.). Hoboken, NJ: Wiley and Sons.
- Weyori, B. A., & Boateng, K. O. (2013). Dynamic intelligent mean filter for impulse noise suppression in 2D images. *International Journal of Modern Engineering*, 13(2), 60-67.
- Suman, G., & Prajapati, D. (2018). Control chart applications in healthcare: a literature review. *International Journal of Metrology and Quality Engineering*, 9(5), 1-21. <https://doi.org/10.1051/ijmqe/2018003>

## Biographies

**KEVIN M. HUBBARD** is an associate professor of mechanical engineering technology in the Technology and Construction Management Department at Missouri State University. He earned his BS degree (aerospace engineer-

ing, 1991) from the University of Missouri-Rolla; MS (engineering management, 1993) from the University of Missouri-Rolla; and PhD from the University of Missouri-Rolla (engineering management, 1996). His research interests include automation and device control, manufacturing systems, device design, and process optimization. Dr. Hubbard may be reached at [KHubbard@MissouriState.edu](mailto:KHubbard@MissouriState.edu)

**RICHARD N. CALLAHAN** is the department head and a professor of technology and construction management at Missouri State University. He earned his BS degree (engineering management, 1988) from the University of Missouri-Rolla; MS (engineering management, 1992) from the University of Missouri-Rolla; and PhD (engineering management, 1999) from the University of Missouri-Rolla. His interests include process optimization, quality control, and manufacturing systems. Dr. Callahan may be reached at [NealCallahan@MissouriState.edu](mailto:NealCallahan@MissouriState.edu)

**NEBIL BUYURGAN** is a professor of mechanical engineering technology in the Technology and Construction Management Department at Missouri State University. He earned his BS degree (industrial engineering, 1998) from Istanbul Technical University, Turkey; MS (engineering management, 2000) from the University of Missouri-Rolla; and PhD from the University of Missouri-Rolla (engineering management, 2004). His research interests include the optimization of logistics in manufacturing operations, retail operations, military operations, and healthcare operations, as well as supply chain management. Dr. Buyurgan may be reached at [NebilBuyurgan@MissouriState.edu](mailto:NebilBuyurgan@MissouriState.edu)

# INSTRUCTIONS FOR AUTHORS: MANUSCRIPT FORMATTING REQUIREMENTS

The INTERNATIONAL JOURNAL OF MODERN ENGINEERING is an online/print publication designed for Engineering, Engineering Technology, and Industrial Technology professionals. All submissions to this journal, submission of manuscripts, peer-reviews of submitted documents, requested editing changes, notification of acceptance or rejection, and final publication of accepted manuscripts will be handled electronically. The only exception is the submission of separate high-quality image files that are too large to send electronically.

All manuscript submissions must be prepared in Microsoft Word (.doc or .docx) and contain all figures, images and/or pictures embedded where you want them and appropriately captioned. Also included here is a summary of the formatting instructions. You should, however, review the [sample Word document](http://ijme.us/formatting_guidelines/) on our website ([http://ijme.us/formatting\\_guidelines/](http://ijme.us/formatting_guidelines/)) for details on how to correctly format your manuscript. The editorial staff reserves the right to edit and reformat any submitted document in order to meet publication standards of the journal.

The references included in the References section of your manuscript must follow APA-formatting guidelines. In order to help you, the sample Word document also includes numerous examples of how to format a variety of scenarios. Keep in mind that an incorrectly formatted manuscript will be returned to you, a delay that may cause it (if accepted) to be moved to a subsequent issue of the journal.

1. **Word Document Page Setup:** Two columns with ¼" spacing between columns; top of page = ¾"; bottom of page = 1" (from the top of the footer to bottom of page); left margin = ¾"; right margin = ¾".
2. **Paper Title:** Centered at the top of the first page with a 22-point Times New Roman (Bold), small-caps font.
3. **Page Breaks:** Do not use page breaks.
4. **Figures, Tables, and Equations:** All figures, tables, and equations must be placed immediately after the first paragraph in which they are introduced. And, each must be introduced. For example: "Figure 1 shows the operation of supercapacitors." "The speed of light can be determined using Equation 4:"

5. **More on Tables and Figures:** Center table captions above each table; center figure captions below each figure. Use 9-point Times New Roman (TNR) font. Italicize the words for table and figure, as well as their respective numbers; the remaining information in the caption is not italicized and followed by a period—e.g., "*Table 1*. Number of research universities in the state." or "*Figure 5*. Cross-sectional aerial map of the forested area."
6. **Figures with Multiple Images:** If any given figure includes multiple images, do NOT group them; they must be placed individually and have individual minor captions using, "(a)" "(b)" etc. Again, use 9-point TNR.
7. **Equations:** Each equation must be numbered, placed in numerical order within the document, and introduced—as noted in item #4.
8. **Tables, Graphs, and Flowcharts:** All tables, graphs, and flowcharts must be created directly in Word; tables must be enclosed on all sides. The use of color and/or highlighting is acceptable and encouraged, if it provides clarity for the reader.
9. **Textboxes:** Do not use text boxes anywhere in the document. For example, table/figure captions must be regular text and not attached in any way to their tables or images.
10. **Body Fonts:** Use 10-point TNR for body text throughout (1/8" paragraph indentation); indent all new paragraphs as per the images shown below; do not use tabs anywhere in the document; 9-point TNR for author names/affiliations under the paper title; 16-point TNR for major section titles; 14-point TNR for minor section titles.



11. **Personal Pronouns:** Do not use personal pronouns (e.g., "we" "our" etc.).
12. **Section Numbering:** Do not use section numbering of any kind.
13. **Headers and Footers:** Do not use either.

14. **References in the Abstract:** Do NOT include any references in the Abstract.
  15. **In-Text Referencing:** For the first occurrence of a given reference, list all authors—last names only—up to seven (7); if more than seven, use “et al.” after the seventh author. For a second citation of the same reference—assuming that it has three or more authors—add “et al.” after the third author. Again, see the *sample Word document* and the *formatting guide for references* for specifics.
  16. **More on In-Text References:** If you include a reference on any table, figure, or equation that was not created or originally published by one or more authors on your manuscript, you may not republish it without the expressed, written consent of the publishing author(s). The same holds true for name-brand products.
  17. **End-of-Document References Section:** List all references in alphabetical order using the last name of the first author—last name first, followed by a comma and the author’s initials. Do not use retrieval dates for websites.
  18. **Author Biographies:** Include biographies and current email addresses for each author at the end of the document.
  19. **Page Limit:** Manuscripts should not be more than 15 pages (single-spaced, 2-column format, 10-point TNR font).
  20. **Page Numbering:** Do not use page numbers.
  21. **Publication Charges:** Manuscripts accepted for publication are subject to mandatory publication charges.
  22. **Copyright Agreement:** A copyright transfer agreement form must be signed by all authors on a given manuscript and submitted by the corresponding author before that manuscript will be published. Two versions of the form will be sent with your manuscript’s acceptance email.
23. **Submissions:** All manuscripts and required files and forms must be submitted electronically to Dr. Philip D. Weinsier, manuscript editor, at [philipw@bgsu.edu](mailto:philipw@bgsu.edu).
  24. **Published Deadlines:** Manuscripts may be submitted at any time during the year, irrespective of published deadlines, and the editor will automatically have your manuscript reviewed for the next-available issue of the journal. Published deadlines are intended as “target” dates for submitting new manuscripts as well as revised documents. Assuming that all other submission conditions have been met, and that there is space available in the associated issue, your manuscript will be published in that issue if the submission process—including payment of publication fees—has been completed by the posted deadline for that issue.

Missing a deadline generally only means that your manuscript may be held for a subsequent issue of the journal. However, conditions exist under which a given manuscript may be rejected. Always check with the editor to be sure. Also, if you do not complete the submission process (including all required revisions) within 12 months of the original submission of your manuscript, your manuscript may be rejected or it may have to begin the entire review process anew.

Only one form is required. Do not submit both forms!

The form named “paper” must be hand-signed by each author. The other form, “electronic,” does not require hand signatures and may be filled out by the corresponding author, as long as he/she receives written permission from all authors to have him/her sign on their behalf.



[www.ijeri.org](http://www.ijeri.org)

Print ISSN: 2152-4157  
Online ISSN: 2152-4165



[www.iajc.org](http://www.iajc.org)

## INTERNATIONAL JOURNAL OF ENGINEERING RESEARCH AND INNOVATION

### **ABOUT IJERI:**

- IJERI is the second official journal of the International Association of Journals and Conferences (IAJC).
- IJERI is a high-quality, independent journal steered by a distinguished board of directors and supported by an international review board representing many well-known universities, colleges, and corporations in the U.S. and abroad.
- IJERI has an impact factor of **1.58**, placing it among an elite group of most-cited engineering journals worldwide.

### **OTHER IAJC JOURNALS:**

- The International Journal of Modern Engineering (IJME)  
For more information visit [www.ijme.us](http://www.ijme.us)
- The Technology Interface International Journal (TIIJ)  
For more information visit [www.tiij.org](http://www.tiij.org)

### **IJERI SUBMISSIONS:**

- Manuscripts should be sent electronically to the manuscript editor, Dr. Philip Weinsier, at [philipw@bgsu.edu](mailto:philipw@bgsu.edu).

For submission guidelines visit  
[www.ijeri.org/submissions](http://www.ijeri.org/submissions)

### **TO JOIN THE REVIEW BOARD:**

- Contact the chair of the International Review Board, Dr. Philip Weinsier, at [philipw@bgsu.edu](mailto:philipw@bgsu.edu).

For more information visit  
[www.ijeri.org/editorial](http://www.ijeri.org/editorial)

### **INDEXING ORGANIZATIONS:**

- IJERI is currently indexed by 16 agencies. For a complete listing, please visit us at [www.ijeri.org](http://www.ijeri.org).

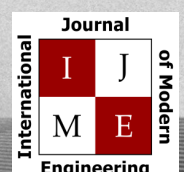
### **Contact us:**

**Mark Rajai, Ph.D.**

Editor-in-Chief  
California State University-Northridge  
College of Engineering and Computer Science  
Room: JD 4510  
Northridge, CA 91330  
Office: (818) 677-5003  
Email: [mrajai@csun.edu](mailto:mrajai@csun.edu)



[www.tiij.org](http://www.tiij.org)



[www.ijme.us](http://www.ijme.us)

# THE LEADING JOURNAL OF ENGINEERING, APPLIED SCIENCE AND TECHNOLOGY

**The latest impact factor (IF) calculation (Google Scholar method) for IJME of 3.0 moves it even higher in its march towards the top 10 engineering journals.**

**IJME IS THE OFFICAL AND FLAGSHIP JOURNAL OF THE  
INTERNATIONAL ASSOCIATION OF JOURNALS AND CONFERENCE (IAJC)**

[www.iajc.org](http://www.iajc.org)



The International Journal of Modern Engineering (IJME) is a highly-selective, peer-reviewed journal covering topics that appeal to a broad readership of various branches of engineering and related technologies. IJME is steered by the IAJC distinguished board of directors and is supported by an international review board consisting of prominent individuals representing many well-known universities, colleges, and corporations in the United States and abroad.

## **IJME Contact Information**

**General questions or inquiries about sponsorship of the journal should be directed to:**

**Mark Rajai, Ph.D.**

**Editor-in-Chief**

**Office: (818) 677-5003**

**Email: [editor@ijme.us](mailto:editor@ijme.us)**

**Department of Manufacturing Systems Engineering & Management**

**California State University-Northridge**

**1811 Nordhoff St.**

**Northridge, CA 91330**